

Measurement of the $K^+ \rightarrow \pi^+ \nu \bar{\nu}$ Branching Ratio

The E949 Collaboration

Abstract

The BNL-E949 experiment has collected a data sample equivalent to 1.77×10^{12} K^+ decays at rest during its 2002 physics run. These data are analyzed via a blind analysis with a technique called the "Bifurcation Method", in order to obtain an unbiased background estimate in the signal box for the rare kaon $K^+ \rightarrow \pi^+ \nu \bar{\nu}$. The total background level was estimated to be about 0.30 ± 0.02 events. One candidate event is observed, giving an upper limit for the branching ratio $\mathcal{B}(K^+ \rightarrow \pi^+ \nu \bar{\nu}) < 8.76 \times 10^{-10}$ (90% CL). Combining with the other two candidate events observed by the BNL-E787 experiment gives the branching ratio $(1.47_{-0.93}^{+1.60}) \times 10^{-10}$, which is consistent with the Standard Model prediction of $(0.78 \pm 0.12) \times 10^{-10}$, and thus sets a limit of $0.0024 < |V_{td}| < 0.0322$ on the Cabibbo-Kobayashi-Maskawa matrix element V_{td} .

1 Introduction

The Standard Model (SM) has so far well explained almost of all the experimental results in particle physics. Despite this success, there are still some experimental observations which the SM cannot account for. The matter and antimatter asymmetry is one of these exceptions, for example, the cosmological baryon asymmetry in our universe[1]. According to Sakharov[2], one of necessary condition to generate such an asymmetry is that the elementary interaction violates charge conjugation symmetry (C) and the combined CP symmetry (where P is parity symmetry). However, the strength of asymmetry cannot be derived by the model calculations based on the SM[3]. Whether or not there are new sources of CP violation has been searched for many years in particle physics experiments. In this paper, we will detail the analysis of BNL-E949 experiment, which are mostly in common with BNL-E787 experiment.

This paper is arranged as following. We will first review CP violation and rare kaon decays. And then we will describe the sources of background and how we can suppress the background in designing the kaon beamline, the detector and the selection criteria in data analysis. We will describe our unique methods in estimating the background level and in evaluating the acceptance. After opening the signal box, we will present our method in extracting branching ratio, making full use of our knowledge on the background in the signal box. In the end of this paper, we will also show how the result of rare kaon decay can give an impact on discovery of the new physics beyond the SM.

1.1 CP Violation and rare decay $K^+ \rightarrow \pi^+ \nu \bar{\nu}$

In the Standard Model, CP violation in flavour changing processes is related to a imaginary phase in the quark mixing matrix[4], assuming that there are three generations of quarks. This matrix is known as the Cabibbo-Kobayashi-Maskawa (CKM) matrix. In Wolfenstein parameterization [5], the CKM matrix can be written in powers of $\lambda = \sin \theta_c = 0.22$:

$$V_{CKM} = \begin{pmatrix} V_{ud} & V_{us} & V_{ub} \\ V_{cd} & V_{cs} & V_{cb} \\ V_{td} & V_{ts} & V_{tb} \end{pmatrix} \simeq \begin{pmatrix} 1 - \lambda^2/2 & \lambda & A\lambda^3(\rho - i\eta) \\ -\lambda & 1 - \lambda^2/2 & A\lambda^2 \\ A\lambda^3(1 - \rho - i\eta) & -A\lambda^2 & 1 \end{pmatrix}. \quad (1)$$

Where A , λ , ρ and η are real numbers. CP invariance of the Lagrangian for weak interactions is violated when the CKM matrix is a complex one. The parameter η describes CP violation in the SM, since a non-zero value of the parameter η breaks the CP invariance for weak interactions.

The unitarity of the CKM matrix can be expressed in terms of six unitarity conditions, which can be represented graphically in the form of triangles, all of which must have the same area. The area of these triangles is equal to one half of the Jarlskog invariant, J_{CP} [7]. Applying the unitarity property $V^\dagger V = 1$ to the CKM matrix in (1) implies

$$V_{ub}^* V_{ud} + V_{cb}^* V_{cd} + V_{tb}^* V_{td} \simeq V_{ub}^* - \lambda V_{cb}^* + V_{td} = 0, \quad (2)$$

where the approximations $V_{ud} \simeq V_{tb}^* \simeq 1$ and $V_{cd} \simeq -\lambda$ have been made. This equation can be represented graphically, as shown in Figure 1, where we have divided all of the sides

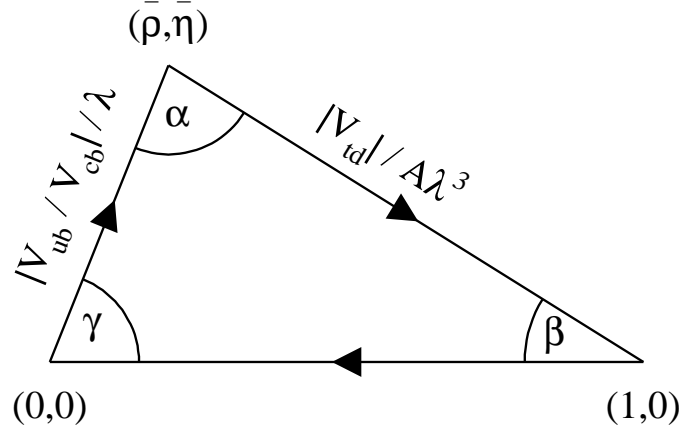


Figure 1: Unitarity triangles in the $\rho-\eta$ plane. Two sides of the triangle can be expressed by the CKM matrix elements $|V_{td}|/A\lambda^3$ and $|V_{ub}/V_{cb}|/\lambda$, respectively, where A and λ are parameters in the Wolfenstein parameterization.

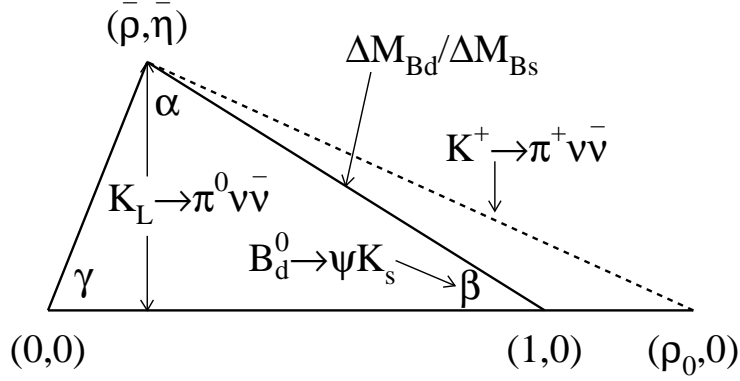


Figure 2: Unitarity triangle determined by B and K decays. The ρ and η can be determined by two ways: angle β from the CP violation asymmetry in the decay $B_d^0 \rightarrow J/\psi K_s^0$, and the length of the side from $\Delta M_{B_s}/\Delta M_{B_d}$ in $B^0 - \bar{B}^0$ mixing; the height of the triangle from $\mathcal{B}(K_L^0 \rightarrow \pi^0 \nu \bar{\nu})$ and the radius of a circle centered at $(\rho_0, 0)$ from $\mathcal{B}(K^+ \rightarrow \pi^+ \nu \bar{\nu})$.

by λV_{cb}^* . The apex of the triangle is given by two well-known Wolfenstein parameters, $\bar{\rho}$ and $\bar{\eta}$, where $\bar{\rho} = \rho(1 - \lambda^2/2)$ and $\bar{\eta} = \eta(1 - \lambda^2/2)$.

B and kaon are by now the only two mesons showing evidence of CP violation in their decay processes. Whether or not the observed CP violation can be explained by the CKM phase within the SM, the determination of ρ and η independently from B and K decays as shown in Figure 2 becomes very crucial. can be examined in two ways, as follows:

- A comparison of angle β from the ratio $\mathcal{B}(K_L^0 \rightarrow \pi^0 \nu \bar{\nu})/\mathcal{B}(K^+ \rightarrow \pi^+ \nu \bar{\nu})$ and from CP violation asymmetry (\mathcal{A}_{CP}) in the decay $B_d^0 \rightarrow J/\psi K_s^0$.
- A comparison of the magnitude $|V_{td}|$ from $K^+ \rightarrow \pi^+ \nu \bar{\nu}$ and from the mixing frequencies of B_s and B_d mesons, expressed in terms of the ratio of the mass differences, $\Delta M_{B_s}/\Delta M_{B_d}$.

Although the decay $K^+ \rightarrow \pi^+ \nu \bar{\nu}$ is a Flavour Changing Neutral Current (FCNC) process prohibited in the tree level and the first order of loop level, this decay is allowed

in the second order, and is described by a "Box" diagram and two "Z-penguin" diagrams, as shown in Figure 3. The weak amplitude for this process is represented as

$$\mathcal{M} \sim \sum_{i=u,c,t} V_{is}^* V_{id} \frac{\gamma^\mu q_\mu + m_i}{q^2 - m_i^2}, \quad (3)$$

where the V_{ij} 's are the CKM matrix elements, the γ^μ 's are the Dirac matrices, the q_μ is the momentum transfer, and the m_i 's are quark masses. \mathcal{M} vanishes if all of the quark masses, m_i , are equal, because of the unitarity of the CKM matrix. However, the breaking of flavor symmetry, which results in the different quark masses, allows this decay to proceed at a very small rate, especially the discovery of the top quark violates the quark mass equality at a maximum, giving a largest contribution to the $K^+ \rightarrow \pi^+ \nu \bar{\nu}$ branching ratio via the weak coupling of top to down quarks in term of V_{td} in the CKM matrix element.

The branching ratio for $K^+ \rightarrow \pi^+ \nu \bar{\nu}$ is calculated by following the convention in [8]. The effective Hamiltonian can be written in the SM as

$$\mathcal{H}_{eff}^{SM} = \frac{G_F}{\sqrt{2}} \frac{\alpha}{2\pi \sin^2 \Theta_W} \sum_{l=e,\mu,\tau} (V_{cs}^* V_{cd} X_{NL}^l + V_{ts}^* V_{td} X(x_t)) (\bar{s}d)_{V-A} (\bar{\nu}_l \nu_l)_{V-A}, \quad (4)$$

where

$$X(x_t) \equiv X_0(x_t) + \frac{\alpha_s(m_t)}{4\pi} X_1(x_t) = \eta_X \cdot X_0(x_t) \quad (5)$$

and

$$X_0(x_t) \equiv C_0(x_t) - 4B_0(x_t), \quad \eta_X = 0.995. \quad (6)$$

$B_0(x_j)$ and $C_0(x_j)$ in (6) are functions of $x_j \equiv m_j^2/M_W^2$, and were derived for the first time by Inami and Lim in 1981 [9]. The coefficient X_{NL}^l and the function $X(x_t)$ are the charm and top quark contributions, including QCD corrections at the next-leading-order (NLO) level [10, 11, 12].

With the top quark mass in the minimal subtraction (\overline{MS}) scheme $m_t = (168.1 \pm 4.1)$ GeV[8],

$$X(x_t) = 1.529 \pm 0.042 \quad (7)$$

is obtained.

The perturbative charm contribution gives the largest theoretical uncertainty and can be described in terms of the parameter

$$P_c(X) \equiv \frac{1}{\lambda^4} \left[\frac{2}{3} X_{NL}^e + \frac{1}{3} X_{NL}^\tau \right] = 0.39 \pm 0.07, \quad (8)$$

where $\lambda = \sin \theta_c$, and the error is obtained by varying the charm mass, m_c , the scale factor, $\mu_c = \mathcal{O}(m_c)$ and the coupling constant, $\alpha_s(M_Z^2)$, by certain amounts. Therefore, one can have

$$\mathcal{B}(K^+ \rightarrow \pi^+ \nu \bar{\nu}) = \kappa_+ \cdot \left[\left(\frac{\text{Im} \lambda_t}{\lambda^5} X(x_t) \right)^2 + \left(\frac{\text{Re} \lambda_c}{\lambda} P_c(X) + \frac{\text{Re} \lambda_t}{\lambda^5} X(x_t) \right)^2 \right], \quad (9)$$

$\lambda = V_{us} = 0.2240 \pm 0.0036$
$\bar{\rho} = 0.187 \pm 0.059$
$\bar{\eta} = 0.354 \pm 0.027$
$ V_{cb} = (41.5 \pm 0.8) \times 10^{-3}$
$ V_{ub}/V_{cb} = 0.092 \pm 0.014$
$ V_{td} = (8.24 \pm 0.54) \times 10^{-3}$
$A = V_{cb} /\lambda^2 = 0.827 \pm 0.016$
$\sin 2\beta = 0.732 \pm 0.049$
$m_t = 168.1 \pm 4.1 \text{ GeV}$
$X(x_t) = 1.529 \pm 0.042$
$P_c(X) = 0.389 \pm 0.073$
$\rho_0 = 1 + \lambda^4 P_c(X)/ V_{cb} ^2 X(x_t) = 1 + P_c(X)/A^2 X(x_t) = 1.373 \pm 0.068$
$\xi = f_{B_s} \sqrt{B_s}/f_{B_d} \sqrt{B_d} = 1.24 \pm 0.08$

Table 1: Parameters that are used in the SM prediction of the $\mathcal{B}(K^+ \rightarrow \pi^+ \nu \bar{\nu})$.

where

$$\kappa_+ \equiv r_+ \frac{3\alpha^2 \mathcal{B}(K^+ \rightarrow \pi^0 e^+ \nu)}{2\pi^2 \sin^4 \Theta_W} \lambda^8 = (4.84 \pm 0.06) \times 10^{-11} \left[\frac{\lambda}{0.224} \right]^8 \quad (10)$$

and the λ_j 's ($\equiv V_{js}^* V_{jd}$) are from the CKM matrix elements. The r_+ ($= 0.901$) represents isospin breaking corrections in relating $K^+ \rightarrow \pi^+ \nu \bar{\nu}$ to the well-measured leading decay $K^+ \rightarrow \pi^0 e^+ \nu$ [13]. In obtaining the numerical value in (10), we used [14]

$$\sin^2 \Theta_W = 0.231, \quad \alpha = \frac{1}{127.9}, \quad \mathcal{B}(K^+ \rightarrow \pi^0 e^+ \nu) = (4.87 \pm 0.06) \times 10^{-2}. \quad (11)$$

Employing the improved Wolfenstein decomposition of the CKM matrix [15], expression (9) describes in the $\bar{\rho} - \bar{\eta}$ plane an ellipse with a small eccentricity, namely

$$(\sigma \bar{\eta})^2 + (\bar{\rho} - \bar{\rho}_0)^2 = \frac{\sigma \mathcal{B}(K^+ \rightarrow \pi^+ \nu \bar{\nu})}{\bar{\kappa}_+ |V_{cb}|^4 X^2(x_t)}, \quad (12)$$

where

$$\bar{\rho}_0 \equiv 1 + \frac{\lambda^4 P_c(X)}{|V_{cb}|^2 X(x_t)}, \quad \sigma \equiv \left(1 - \frac{\lambda^2}{2} \right)^{-2}, \quad \bar{\kappa}_+ \equiv \frac{\kappa_+}{\lambda^8} = (7.64 \pm 0.09) \times 10^{-6}. \quad (13)$$

Using (9) and varying m_t , $|V_{cb}|$, $P_c(X)$ and $|V_{td}|$, which is constrained by $|V_{ub}/V_{cb}|$ and the $B^0 - \bar{B}^0$ mixing in the $\bar{\rho} - \bar{\eta}$ plane, the branching ratio of $K^+ \rightarrow \pi^+ \nu \bar{\nu}$ is predicted to be

$$\mathcal{B}(K^+ \rightarrow \pi^+ \nu \bar{\nu}) = (0.78 \pm 0.12) \times 10^{-10} \quad (14)$$

within the SM. Here, the parameters used are summarized in Table 1. It should be noted that, for an uncertainty of 15% in (14), the theoretical uncertainty is $\sim 7\%$ at present, mainly due to the charm quark contribution.

Theoretically, one of the cleanest ways to extract the $|V_{td}|$ is regarded to be from a precise measurement of $\mathcal{B}(K^+ \rightarrow \pi^+ \nu \bar{\nu})$. This is due to the following reasons:

- Long-distance contributions to the branching ratio are negligible (at most 10^{-13}) [16].
- The uncertainty from the hadronic matrix element has been removed by using $\mathcal{B}(K^+ \rightarrow \pi^0 e^+ \nu)$.
- The remaining theoretical uncertainties (7%) are relatively small and reliable as compared with the errors in other K and B decays.

The theoretical uncertainty will be reduced if we can have a better knowledge about the QCD corrections to the charm contribution at the next-to-next-leading-order (NNLO) level. A precise measurement of $\Delta M_{B_d}/\Delta M_{B_s}$ in $B^0 - \bar{B}^0$ mixing would also narrow down the SM prediction, once $B_s^0 - \bar{B}_s^0$ mixing has been observed [17]. A precise measurement of the $K^+ \rightarrow \pi^+ \nu \bar{\nu}$ branching ratio is therefore a stringent test of the SM and also a probe for new physics.

1.2 History of $K^+ \rightarrow \pi^+ \nu \bar{\nu}$ experiments at BNL

The history of $K^+ \rightarrow \pi^+ \nu \bar{\nu}$ experiments at BNL can be traced back to the middle of 1980's, when the first phase of BNL-E787 experiment was proposed. The experiment was done during the period of 1988-1991, giving an upper limit of the branching ratio to 2.4×10^{-9} at 90% confidence level (CL). The second phase of BNL-E787 experiment was done from 1995 to 1998. The target and the drift chamber were upgraded in order to provide a more precise measurement on momentum, range and energy of the charged pions. Two candidates are observed during the second phase of BNL-E787 experiment, resulting in a measurement of branching ratio $(1.57_{-0.82}^{+1.75}) \times 10^{-10}$. This branching ratio is consistent with the SM prediction $(0.78 \pm 0.12) \times 10^{-10}$. Since the center value can be twice the SM prediction because the experimental uncertainty, the BNL-E949 experiment was proposed in 1999. The goal is to increase the incident kaon flux and the power of the photon veto, so that more statistics and broader pion momentum region can be obtained. It is anticipated that a more precise measurement can not only test the SM with better precision, but also probe the new physics beyond the SM.

1.3 Background classifications

BNL-E949 is a Kaon-stop experiment with clear kinematic features for all the relevant kaon decay modes as shown for the momentum spectra of charged particles in Figure 4. The experimental signature of the $K^+ \rightarrow \pi^+ \nu \bar{\nu}$ decay is a single π^+ track with no other particle from a K^+ decay, because two neutrinos in the final state cannot be detected in the apparatus. Theoretically, the maximum π^+ momentum is 227 MeV/c.

The $K^+ \rightarrow \mu^+ \nu_\mu (\gamma)$ and $K^+ \rightarrow \pi^+ \pi^0$ decays are mainly concerned when the search is only conducted in high momentum region. The signal imitation comes from either a μ^+ being misidentified as π^+ in $K_{\mu 2}$ and the gamma being missed in $K^+ \rightarrow \mu^+ \nu_\mu \gamma$, or the photons from π^0 decay being missed together with the π^+ momentum, range and energy being shifted due to the experimental resolution effect or the occurrence of scattering along the pion trajectory in $K_{\pi 2}$.

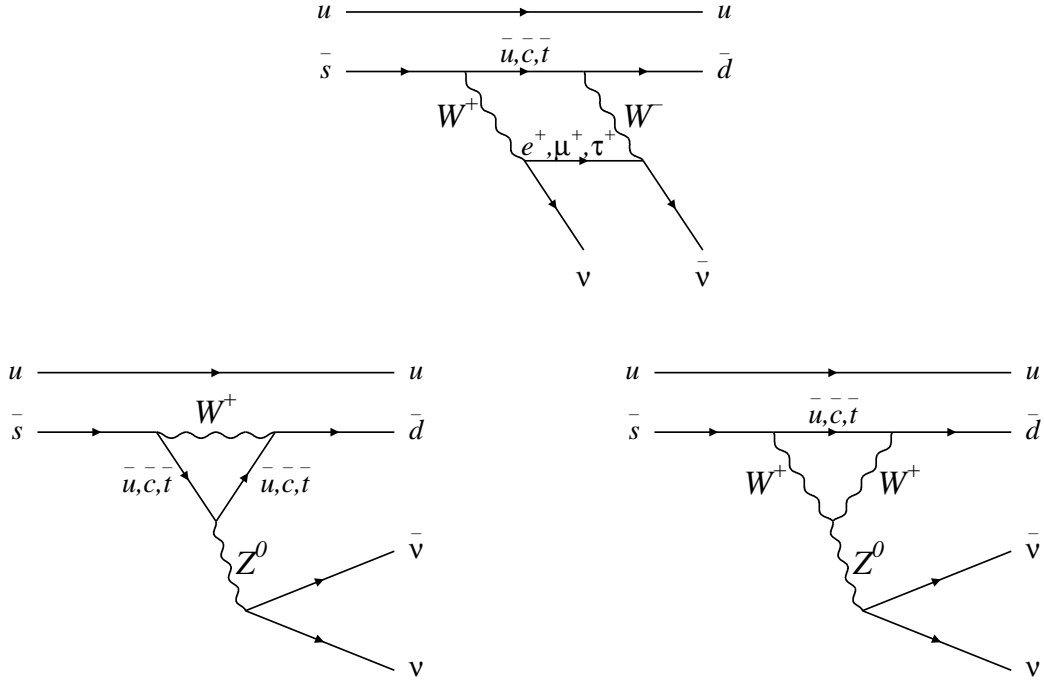


Figure 3: Second-order weak processes that contribute to the $K^+ \rightarrow \pi^+ \nu \bar{\nu}$ branching ratio: the "Box" diagram (upper) and two "Z-penguin" diagrams (bottom).

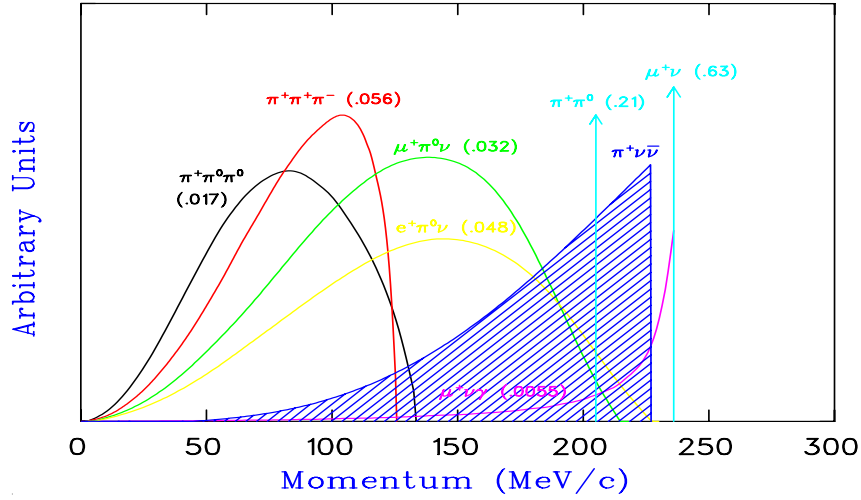


Figure 4: Momentum spectra (in MeV/c) of charged particles from K^+ decays in the rest frame. The values in the parentheses represent the branching ratios for their decay modes. The hatched spectrum shows the π^+ momentum in the $K^+ \rightarrow \pi^+ \nu \bar{\nu}$ decay assuming the $V - A$ interaction.

In addition to the background from Kaon decays, there are also background from the beam contamination, including the single π^+ beam being mis-identified as a K^+ beam, the double beam with an accompanying K^+ or a π^+ beam which cannot be separated by the beam counters, and the interaction of $K^+ + n \rightarrow p + K_L^0$, $K_L^0 \rightarrow \pi^+ l^- \bar{\nu}_l$. The detector was designed to be able to sufficiently suppress the known background sources from the $K^+ \rightarrow \mu^+ \nu_\mu (\gamma)$, the $K^+ \rightarrow \pi^+ \pi^0$ and the beam backgrounds mentioned above.

2 The detector and calibration

BNL-E949 is a successor to BNL-E787. The E949 detector was upgraded to accomodate the higher beam rate, which is almost of twice that of BNL-E787. In this section, we will describe how the experiment was designed and how the calibration was done in order to achieve a precise measurement.

2.1 Beam line of low energy kaons

The K^+ beam is produced by a high-intensity proton beam from the Alternating Gradient Synchrotron (AGS) at BNL. Protons are accelerated to a momentum of 21.5 GeV/c. 65 trillion protons (Tp) are extracted in a 2.2-second long "spill" once every 5.4 seconds from the AGS. The slow extracted beam (SEB) is transported to the kaon production target for BNL-E949. The production target is made of a platinum that extends 6 cm to the beam direction, and is located on a water-cooled copper base. The typical AGS running condition is 45 Tp on the production target per 2.2 second spill at 21.5 GeV/c.

Low Energy Separated Beam line III [32] (LESBIII, shown in Figure 5) collects and focuses kaons produced at the production target. The beam emitted toward 0 degree contains about 500 pions and 500 protons for every kaon, and is momentum-selected by a dipole magnet (D1 in Figure 5). Two electrostatic separators (Separators 1 and 2 in Figure 5) sweep pions and protons out of the beam. The resulting beam is further selected by a second dipole magnet (D2 in Figure 5). LESBIII contains a number of focusing quadrupole (Q1-10), sextupole (S1-3), and octupole (O1) magnets and collimating slits, and has a total length of 19.6 m from the production target to the E949 target. Kaons with 710 MeV/c were transported. The angular acceptance of LESBIII is 12 msr and the momentum acceptance is 4.5% FWHM. LESBIII provides the world's highest-intensity kaon beam of 710 MeV/c with a flux of about 5×10^5 K^+ 's per Tp on the production target. The $K^+ : \pi^+$ ratio in the beam is about 3:1. Proton contamination is negligible due to a large deflection of protons by the separators. Under the typical AGS running condition of 45 Tp on the production target per spill, 1.3×10^7 K^+ 's emerge from LESBIII.

2.2 Beam counters

Since the beam intensity is very high and the beam contains pions with a ratio of $K^+ : \pi^+ = 3 : 1$, a single kaon entering the target should be identified by the beam instrumentation. It has three roles: kaon identification, slowing down the kaon, and detecting the extra beam particles that accompany the studied kaon. The beam instrumentation from upstream to downstream consists of a Čerenkov counter, beam wire chambers, degraders and a beam hodoscope.

The kaon beam from LESBIII enters the Čerenkov counter located just downstream of the last quadrupole magnet (Q10) and 2 m upstream of the target. A side view of the Čerenkov counter is shown in Figure 6. In BNL-E949, the reflection index (n) of the radiator is 1.49, which gives a threshold of Čerenkov radiation $\beta_{\check{C}} = 1/n = 0.671$ and a reflection threshold $\beta_{ref} = \sqrt{\frac{1}{n^2-1}} = 0.905$. Kaons and pions with a momentum of 710

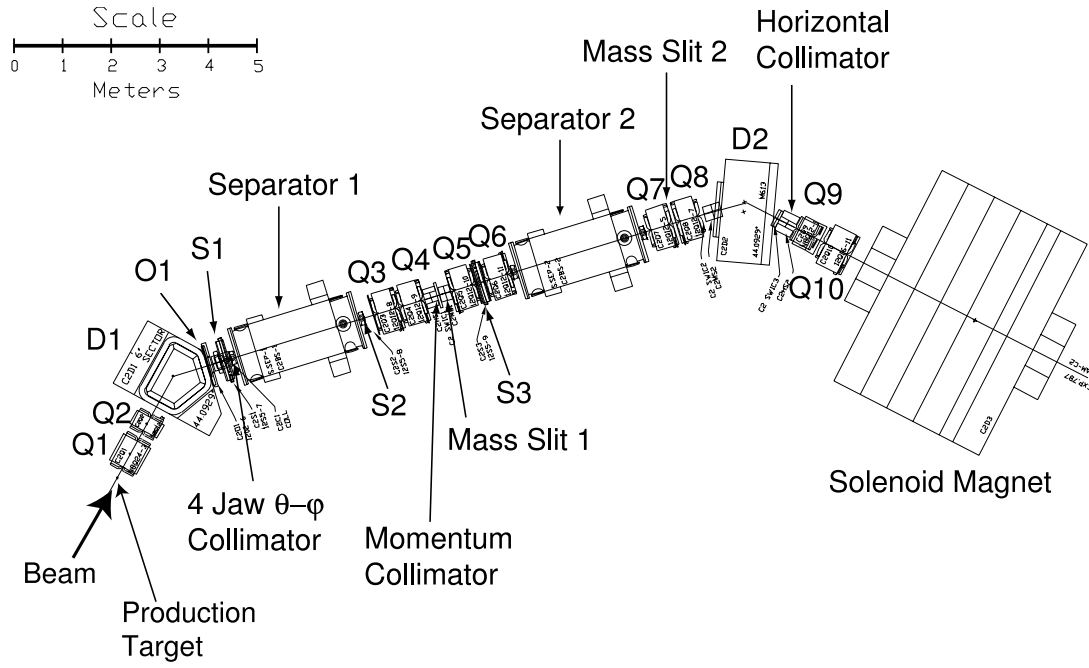


Figure 5: Low-energy separated beam line III at BNL.

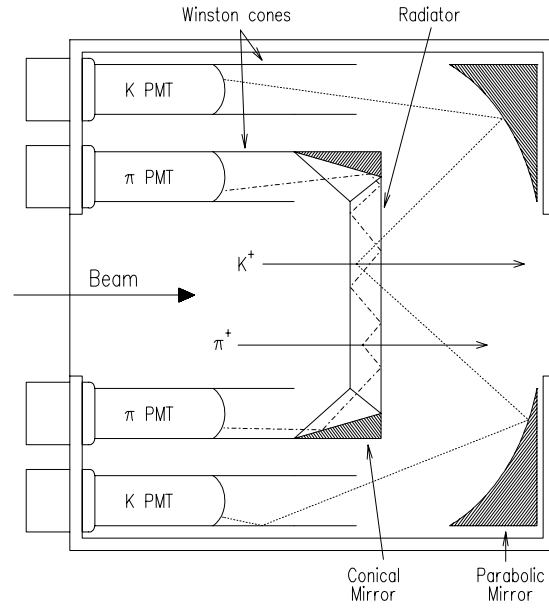


Figure 6: Side view of the Čerenkov counter.

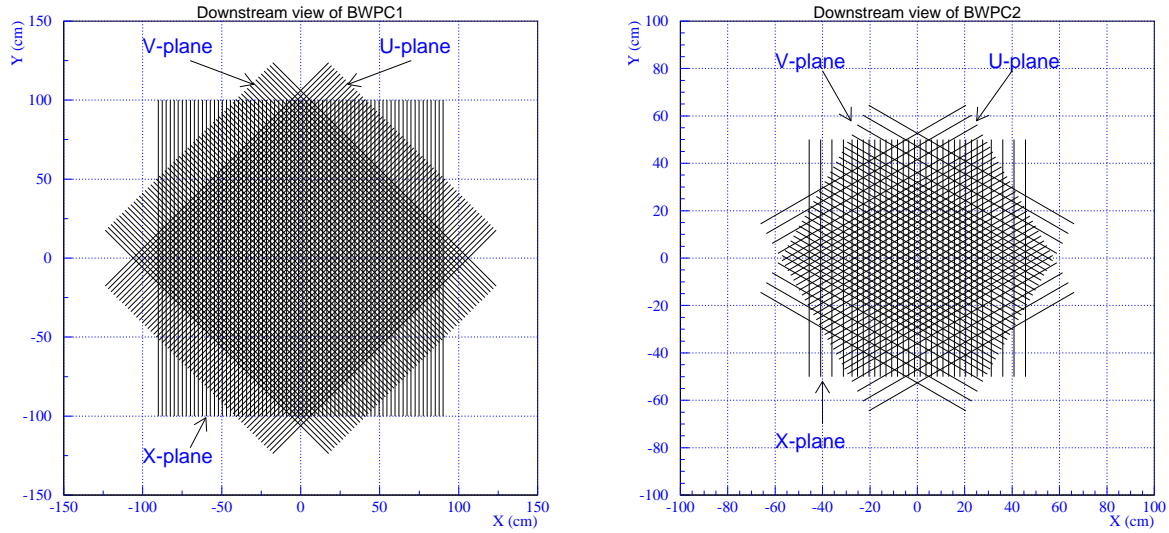


Figure 7: Cross-sectional views of the beam wire chambers (BWPCs): the first BWPC (left) and the second BWPC (right).

MeV/c have $\beta_{K^+} = 0.821$ and $\beta_{\pi^+} = 0.981$, respectively; the Čerenkov light from kaons and pions is unreflected and reflected at the inner surface of the radiator, respectively. The light from a kaon exits the radiator and is reflected by a parabolic mirror to the outer ring of 14 photomultiplier (PMT) tubes (Kaon Čerenkov Counter), while that from a pion is internally reflected within the radiator and detected in the inner ring of 14 PMTs (Pion Čerenkov Counter). The PMT signals are fed to time-to-digital converters (TDCs) via discriminators as well as to 500 MHz transient digitizers based on gallium-arsenide (GaAs) charge-coupled devices (CCDs) [33]. The pulse-height information in every 2 ns interval is recorded in CCDs to reproduce the time development of the pulses. A charged particle passing through the Čerenkov counter fires a number of PMTs in the Kaon or Pion Čerenkov Counters; PMT hits coincident with each other are called a "cluster". A kaon is identified by requiring that the Kaon Čerenkov Counter has a hit cluster and the Pion Čerenkov Counter has no hit cluster. The average time of the hits in each cluster is compared to the K^+ decay time; any extra particle coincident with the K^+ decay time is rejected, since it is likely that an extra particle, not the initial kaon, may be the origin of the charged track that enters the fiducial region of the detector. Two incoming particles close in time can fire the same PMTs, and a pileup signal may not be found by the TDCs; the pulse shapes recorded in the CCDs can be used to discriminate such pileup signals.

Behind the Čerenkov counter, two beam wire chambers (BWPCs) are located, and allow to monitor the beam profile and to identify multiple incoming particles. Cross-sectional views of the BWPCs are shown in Figure 7. The first chamber (BWPC1) consists of 3 planes of sense wires, labeled U, V and X. The direction of the sense wires in the X-plane is vertical and the U- and V-planes are at $\pm 45^\circ$ to the vertical plane. The sense wires are made of gold-plated tungsten with 0.012 mm diameter. The BWPC1 has 72, 60 and 60 readout channels for the X-, U- and V-planes, respectively, with a 2.54 mm wire

spacing. The spacial resolution is 1.54 mm, and the active area is 178 mm (horizontal) by 50.8 mm (vertical). The cathode foils are 0.025-mm thick aluminized mylar coated with carbon. The anode-cathode distance is 3.175 mm, and the total thickness of the BWPC1 is approximately 56 mm. The BWPC1 is filled with a mixture of CF₄ (80%) and Isobutane (20%). The second chamber (BWPC2) is located at 90 cm downstream of the BWPC1 and consists of three planes (U, V and X). The direction of the sense wires in the X-plane is vertical, and the U and V sense wires are at $\pm 60^\circ$ to the vertical plane. Each plane has 24 readout channels with a 2.40-mm wire spacing in the central region (57.6 mm) and 8 channels with a 4.80-mm wire-spacing in the peripheral region (19.2 mm on each end). The cathode foils are 0.008-mm single-side aluminized mylar coated with carbon. The anode-cathode distance is 1.5875 mm. The BWPC2 is filled with the same gas as BWPC1.

Downstream of the BWPCs, cylindrical degraders are located for slowing down the kaons so that they come to rest in the target. The degraders have inactive and active parts. The upstream inactive degrader is made of 111.1-mm long beryllium oxide (BeO) and 4.76 mm Lucite. The total thickness is appropriate for stopping kaons with a momentum of 710 MeV/c. BeO, with high density and low atomic number, minimizes multiple scattering. The downstream active degrader (AD) consists of 40 layers of 2 mm thick scintillator disks (in 139 mm diameter) alternating with 2-mm thick copper disks (in 136 mm diameter). The AD is split into 12 azimuthal segments, and the scintillation lights in each segment are sent to a single PMT through 14 wave length shifting (WLS) fibers. The PMT outputs are fed to TDCs and CCDs. The signals from 4 PMTs are multiplexed and fed to a single analog-to-digital converter (ADC). Using this information, the AD has abilities to identify the beam particles and to detect the activities coincident with kaon decays.

After passing through the degraders, just in front of the target, a beam hodoscope (B4 Hodoscope) detects the incoming particle and identifies the particle as a kaon by measuring the energy deposit. An end view of the B4 Hodoscope is shown in Figure 8. The B4 Hodoscope consists of two planes (U- and V-plane, 119 mm diameter) to provide position information. Each plane has 12 scintillator fingers. The cross section of the finger has a "Z-shape", as shown in Figure 9, which has a 6.35-mm thick middle part and 3.175-mm thick edge parts. This shape makes the B4 Hodoscope to have no inactive region and to improve the spatial resolution. In each finger, 3 WLS fibers are embedded and fed to a single PMT that is read out by TDCs, ADCs and CCDs. A double-pulse fitting is performed to the signals recorded in the CCDs to find a pileup. The time development of the output signals are fitted with single- or double-pulse assumption. If the fitted pulse is more likely to be a double pulse and the time of the second pulse is coincident with the K^+ decay time, the event is rejected.

Kaons with decay-in-flight, nuclear interactions in the degrader materials or scatterings out of beam do not reach the target. It is measured that about 3.9×10^6 kaons enter the target per beam spill.

2.3 Target

Kaons, slowed down by the degraders, enter the scintillating fiber target located in the center of the spectrometer. Kaons lose energy, come to rest, and decay in the target.

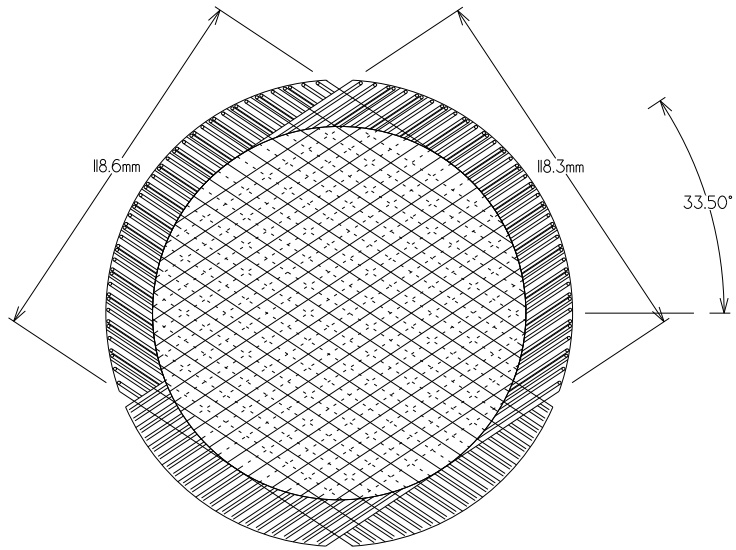


Figure 8: End view of the B4 Hodoscope.

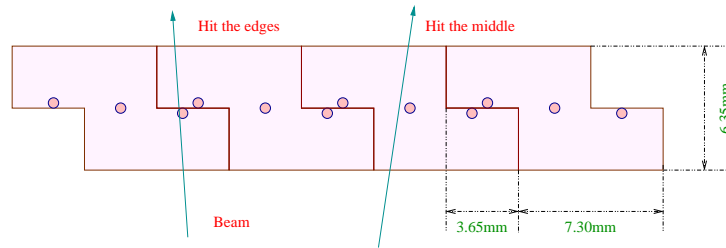


Figure 9: Schematic cross section of the B4 Hodoscope.

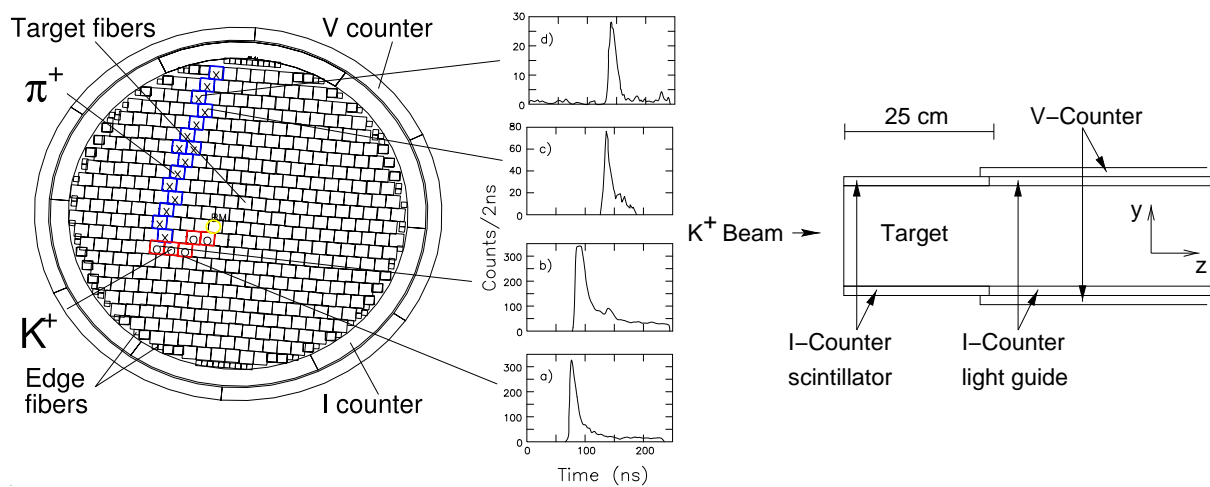


Figure 10: End (left) and side (right) views of the target. The CCD pulse-shape information is used to find kaon and pion clusters, as shown in the left figure; the lower two plots, labeled by "a)" and "b)", are CCD pulses for a kaon, and the upper two plots, labeled by "c)" and "d)", are those for a pion. Two layers of 6 plastic scintillators, I-Counter (IC) and V-Counter (VC), surround the target.

The target consists of 413 5-mm square and 3.1-m long plastic scintillating fibers that are bundled to form a 12-cm diameter cylinder. A number of smaller fibers (called "edge fibers") are filled in the gaps near the outer edge of the target. End and side views of the target are shown in Figure 10. Each of the 5.0-mm fibers is connected to a PMT, whereas the edge fibers are grouped into 12 and each group of the edge fibers is connected to a single PMT. The PMTs are read out by ADCs, TDCs and CCDs. Kaons, whose velocities are small, typically lose a large amount of energy (few tens MeV) in each fiber, while pions from kaon decays lose about 1 MeV per fiber, since they travel as minimum ionizing particles (MIPs). Pattern recognition is performed to find fibers that belong to a kaon's path or a pion's path. The CCD pulse information is used to find clusters for kaons (kaon fibers) and pions (pion fibers). A double-pulse fitting is performed to find the fiber where a $K^+ \rightarrow \pi^+$ decay vertex is located and to estimate the energy loss and range of the pion hidden in the kaon fiber.

The fiducial region of the target is defined by two layers of 6 plastic-scintillating counters that surround the target (see Figure 10). The inner scintillators, called I-Counter (IC), tag charged decay products for a trigger before they enter the drift chamber. The IC is 6.4-mm thick at an inner radius of 6.0 cm, and extends 24 cm downstream from the upstream face of the target. Each scintillator is instrumented with a PMT, and is read out by an ADC, a TDC and a 500 MHz transient digitizer based on flash ADC (TD) [34]. The outer scintillators, called the V-Counter (VC), overlap the downstream edge of the IC by 6 mm, and serve to detect particles that decay downstream of the fiducial region of the target. The VC is 5-mm thick and 1.96-m long, and is staggered with respect to the IC. Each scintillator is instrumented with a PMT, which is read out by an ADC and a TDC.

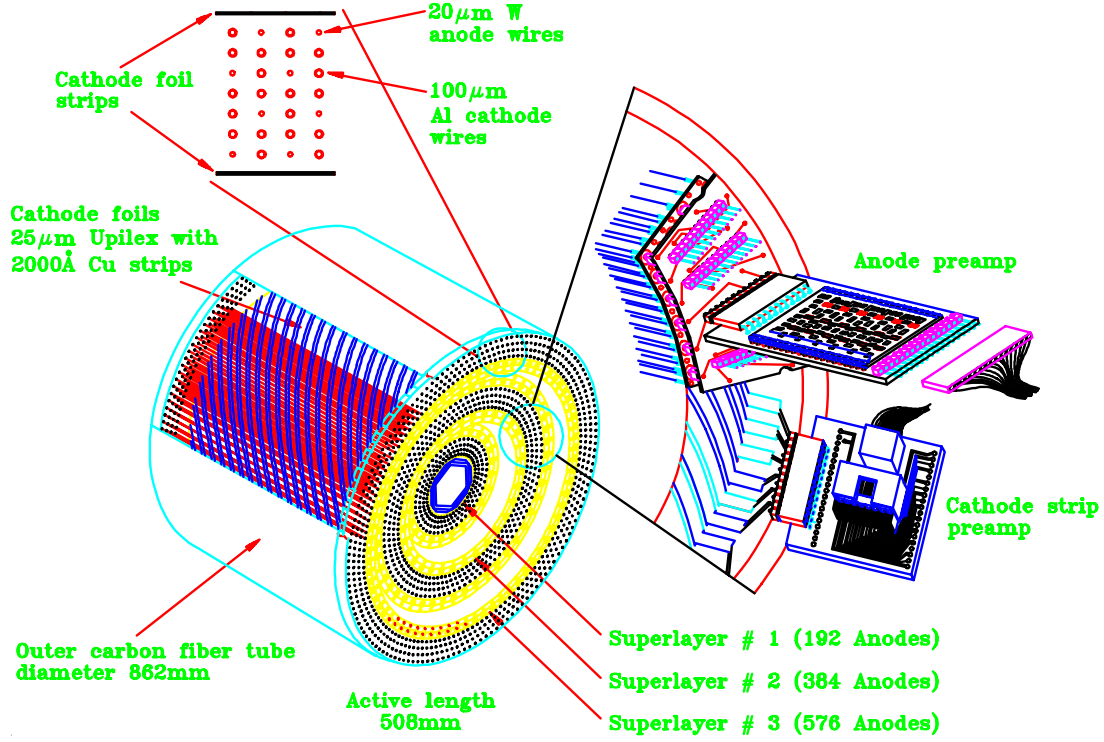


Figure 11: Schematic view of the Ultra Thin Chamber.

2.4 Tracking Chamber

The tracking chamber is also called "Ultra Thin Chamber" (UTC), which is located just outside of the IC. The whole spectrometer is in a 1 Tesla magnetic field. Positively charged particles are bent clockwise in the view from downstream. The primary functions of the UTC are momentum measurements of charged particles and to provide a matching of the tracks between the target and in the Range Stack (RS).

The UTC has a length of 51 cm and inner and outer radii of 7.85 cm and 43.31 cm, respectively. The UTC is composed of 12 layers of drift cells, grouped into 3 superlayers; the inner superlayer has 4 layers of 48 cells, the middle superlayer has 4 layers of 96 cells, and the outer superlayer has 4 layers of 144 cells (shown in Figure 11). Each cell is composed of 9 wires strung axially; a single anode wire, made of gold-coated tungsten with 20-μm diameter, is surrounded by 8 cathode wires made of gold-coated aluminum with 100-μm diameter, which are arranged in a "square". Adjacent cells share the cathode wires at the boundaries. The cells in each layer are staggered by one-half cell with respect to the neighboring layers in order to resolve a left-right ambiguity. The superlayers are filled with a mixture of argon (49.6%), ethane (49.6%) and ethanol (0.8%) gases. The cathode wires are grounded, and the anode wires are maintained at 2 kV (gain = 8×10^4 , drift velocity = 5 cm/μs). Each anode wire is instrumented with an ADC and a TDC. The drift time to the anode wires provides (x, y) positions for charged tracks.

The inner and outer radii of each superlayer have helical arrays of cathode strips, whose pitch-angle is 45°. The strips, whose width is 7 mm, are made of 1200-Å thick copper coated with 300-Å thick nickel, and mounted on a 25-μm thick Kapton foil. The

separation between the strips is 1 mm. The cathode foils have 48, 72, 108, 144, 180, and 216 strips from the inner to the outer layers, respectively. The Z position of a charged track is measured from the charge-weighted mean of the cluster of hit strips. The resolution for a z-position measurement is about 1 mm. Each cathode strip is instrumented with an ADC and a TDC.

There are 2 inactive regions filled with nitrogen gas between the 3 superlayers. The differential pressure in the 5 gas volumes supports the cathode foils (excluding the innermost and outermost foils, which are held in place by support tubes). The total mass in the active region of UTC (excluding the inner and outer support tubes and innermost and outermost foils) amounts to 2×10^{-3} radiation lengths. The momentum resolutions ($\Delta P/P$) for the two body decays $K_{\pi 2}$ and $K_{\mu 2}$ are 1.1% and 1.3%, respectively. Detail information can be seen elsewhere [35].

2.5 Range Stack scintillator counters

The Range Stack (RS) scintillator counters are used for measuring the energy and range of charged particles and particle identification as well. The RS is located just outside the UTC at an inner radius of 45.08 cm and an outer radius of 84.67 cm. It consists of 19 layers of plastic scintillators, azimuthally segmented into 24 sectors (see Figure 12). Conventionally, the 24 sectors are grouped into 6 (sectors 1-4, 5-8, 9-12, 13-16, 17-20, 21-24); a group of 4 sectors is called a "hexant". The scintillators of layers 2-18 have a thickness of 1.905 cm and a length of 182 cm. The scintillators of layer 19 have a thickness of 1 cm; this layer is mainly used to veto charged particles with long range by requiring that they do not reach the layer-19 scintillators. The scintillation light in the layer 2-19 counters is led by light guides to PMTs at both the upstream and downstream ends. The innermost counters, called T-Counters, have a thickness of 6.35 mm and a length of 52 cm. Seventeen WLS fibers are embedded in each scintillator for read out, and are grouped and fed to a single PMT at each end. The T-Counter signals are used to produce a trigger signal and to define the fiducial region as 2π sr solid angle, which is almost the same as the solid-angle acceptance of UTC. Each PMT of the RS scintillators is read out by an ADC and a TDC. Signals from 4 PMTs at the same end, same hexant and same layer are mixed together and read out by a single Transient Digitizer based on flash ADC (TD). The signals are demultiplexed in offline event reconstruction by using TDC information in order to determine from which counter the signal comes. The ADCs record charges in 100 ns, and the TDCs record the timings of hits in the range of 10 μ s. The TDs record pulse-heights of PMT signals in 2 ns intervals (500 MHz sampling) up to 2 μ s to provide information on the time development of the pulses. This 500 MHz sampling provides detailed information about the pulse shapes, which enables the separation of two pulses as close as 5ns in time by performing an offline pulse fitting (explained later). The gate width of the TDs is narrower than that of the TDCs in order to reduce the data size. The time of a hit in the RS counters is obtained from the average of the upstream and downstream TDC times, and the z position of the hit is obtained from the time difference. In the case that TDC hit information is missed due to some reasons, the hit information is complemented with corresponding TD information if available.

The π^+ from the $K^+ \rightarrow \pi^+ \nu \bar{\nu}$ decay, whose momentum is up to 227 MeV/c, should

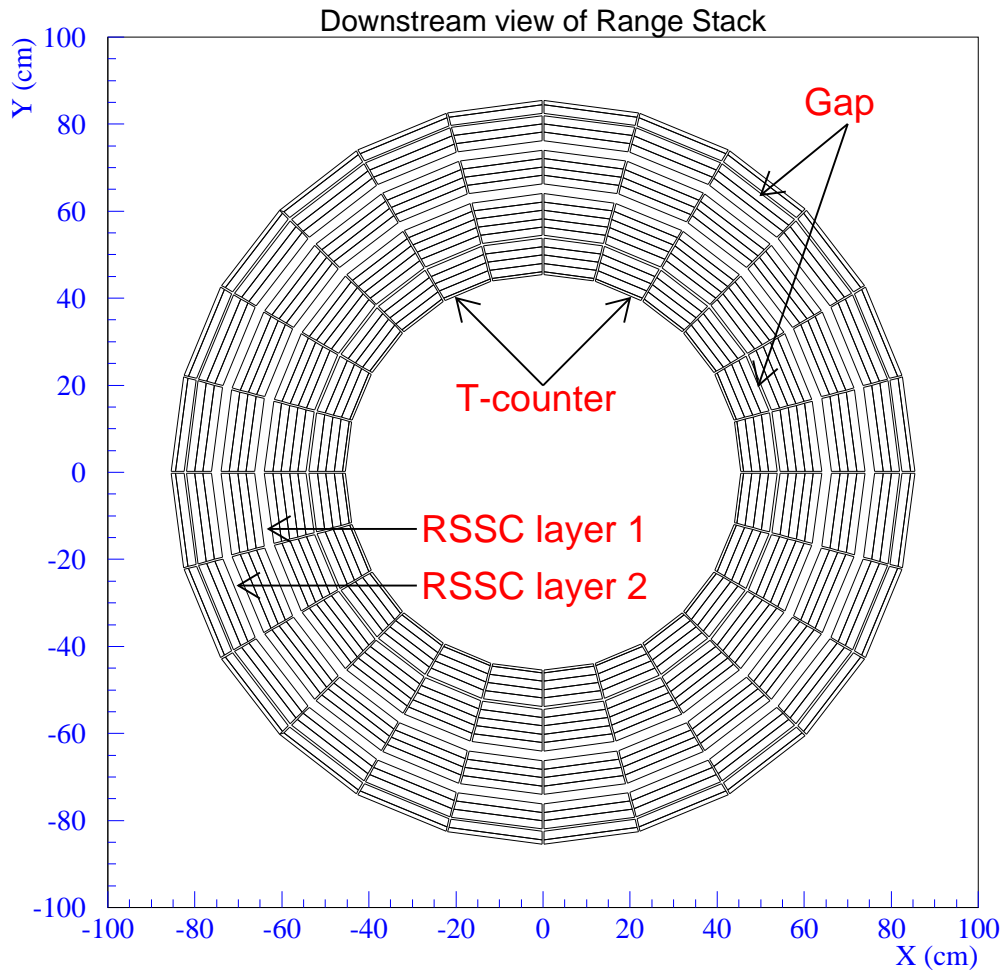


Figure 12: End view of the Range Stack. Two layers of the Range Stack Straw Chambers are located after layers 10 and 14.

come to rest in the RS. Pions with 227 MeV/c can propagate into plastic scintillators by roughly 40 cm. The total radial thickness of the RS and target is 45 cm. Almost all of the π^+ 's, bent in a 1 Tesla magnetic field, therefore lose their entire kinetic energy and come to rest in the Range Stack. On the other hand, the momenta of μ^+ 's from kaon decays at rest are at most 236 MeV/c. Muons with 236 MeV/c (such as μ^+ 's from $K_{\mu 2}$ decays) can propagate into plastic scintillators by 54.3 cm. Hence, $K_{\mu 2}$ decays are largely suppressed by requiring that charged tracks come to rest in the RS. However, the μ^+ 's from $K^+ \rightarrow \mu^+ \nu_\mu \gamma$ and $K^+ \rightarrow \mu^+ \pi^0 \nu_\mu$ decays could come to rest in the RS. Besides, a π^+ can decay in flight and the secondary μ^+ may come to rest in the RS. The identification of π^+ in the RS is performed by observing the $\pi^+ \rightarrow \mu^+ \rightarrow e^+$ decay sequence in the TDs and TDCs of the counter where the π^+ comes to rest (called the stopping counter). Typical TD pulses in and around the stopping counter for a pion track are shown in Figure 13. The μ^+ from the $\pi^+ \rightarrow \mu^+ \nu_\mu$ decay at rest has the kinetic energy of 4 MeV (equivalent range in plastic scintillator is 1 mm) and rarely goes out of the stopping counter. On the contrary, the e^+ from the $\mu^+ \rightarrow e^+ \nu_e \bar{\nu}_\mu$ decay at rest has a kinetic energy of up to 52 MeV, and the e^+ track loses kinetic energy not only in the stopping counter, but also in the neighboring counters. The $\pi^+ \rightarrow \mu^+$ decay at rest, whose lifetime is 26 ns, is detected by using TD information of the stopping counter by performing a double-pulse fitting, while the sequential $\mu^+ \rightarrow e^+$ decay, whose lifetime is 2.2 μ s, is detected by using TDC information of the stopping counter as well as the neighboring counters by requiring that the times of the hits from the e^+ track are consistent with each other.

Range Stack Straw Chambers (RSSCs) are located after layers 10 and 14 in the RS. The inner RSSC consists of two layers of 24 straws per sector, and the outer RSSC consists of two layers of 28 straws per sector. The RSSCs are used to determine the trajectory and the range of a charged particle in the RS. Information on the RSSC is given in [36].

Energy and range measurements of charged tracks, as well as momentum measurement, are crucial to distinguish the π^+ 's in the signal region from backgrounds due to $K_{\pi 2}$ and $K_{\mu 2}$ decays, which have monochromatic momenta of 205 and 236 MeV/c, respectively. Energy resolutions of 2.8% and 2.5% and range resolutions of 2.9% and 3.1% are achieved for fully contained $K_{\pi 2}$ and $K_{\mu 2}$ decays, respectively.

2.6 Photon veto counters

The detection of any activities coincident with the charged track is crucial for suppressing the backgrounds for $K^+ \rightarrow \pi^+ \nu \bar{\nu}$. Photons from $K_{\pi 2}$ and other radiative decays are detected by hermetic photon detectors, which are shown in Figure 14. The photon detectors, surrounding the K^+ decay vertex in a 4π solid angle, are located in the barrel, upstream and downstream end caps, and near the beam line. Photon veto is performed by the Barrel Veto (BV), the Barrel Veto Liner (BVL), the upstream and downstream End Caps (ECs), the upstream and downstream Collar detectors (CO), the downstream Microcollar detector (MC), as well as the target and Range Stack.

The Barrel Veto, 1.9-m long, is located in the outermost barrel region with an inner radius of 94.5 cm and an outer radius of 145.3 cm. It surrounds two thirds of the 4π sr solid angle. The BV consists of 48 azimuthal sectors; each sector consists of four radial segments. The radial modules consist of 16, 18, 20, 21 layers of 1-mm thick lead and

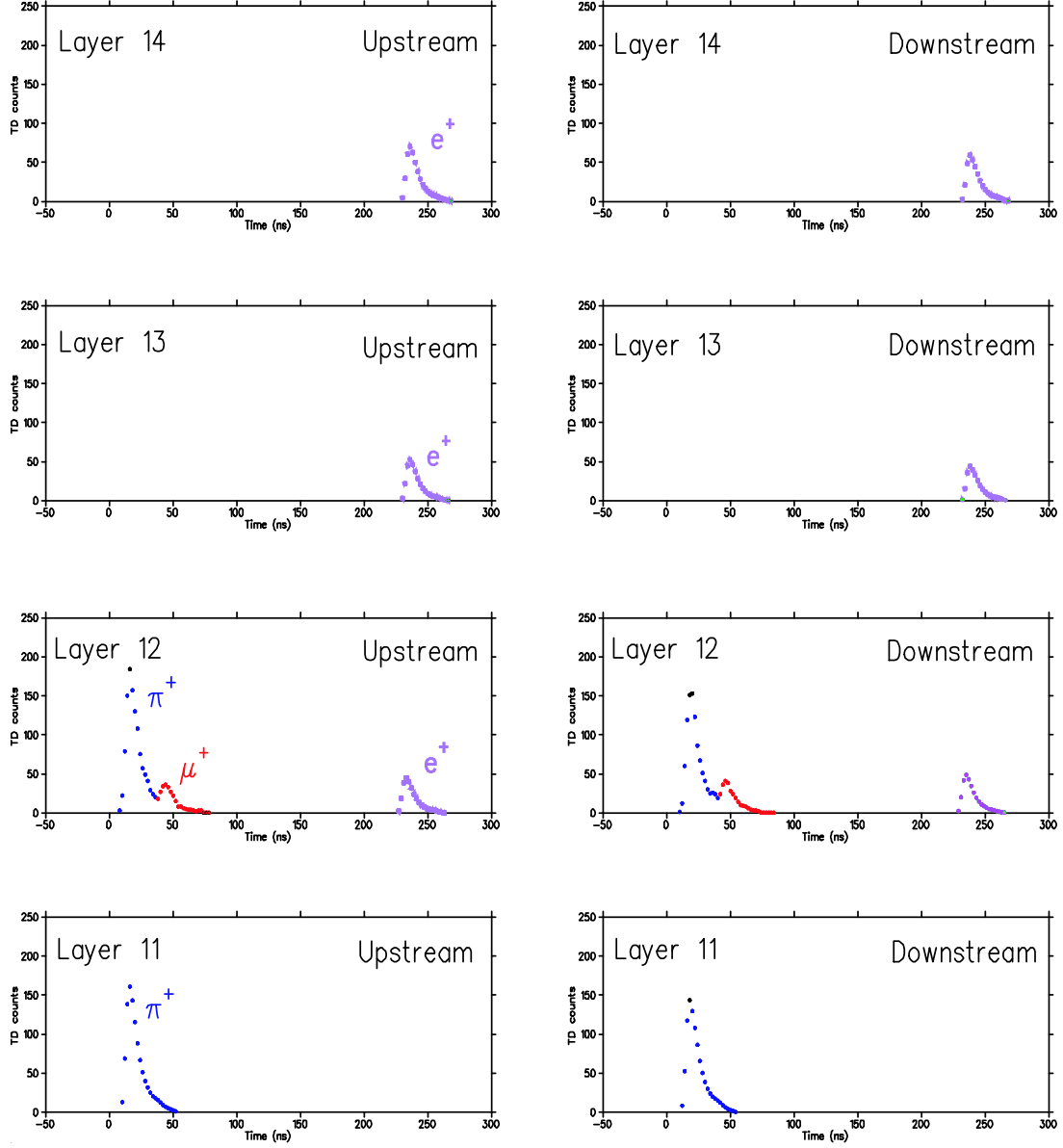


Figure 13: Pulses in and around the stopping counter recorded by the TDs of the upstream and downstream ends. The $\pi^+ \rightarrow \mu^+ \rightarrow e^+$ decay sequence is found in the stopping counter (Layer 12 in this figure). The μ^+ from the $\pi^+ \rightarrow \mu^+ \nu_\mu$ decay is contained in the stopping counter. The positron from the $\mu^+ \rightarrow e^+ \nu_e \bar{\nu}_\mu$ decay should also be found in the counters around the stopping counter (Layers 13 and 14 in this figure).

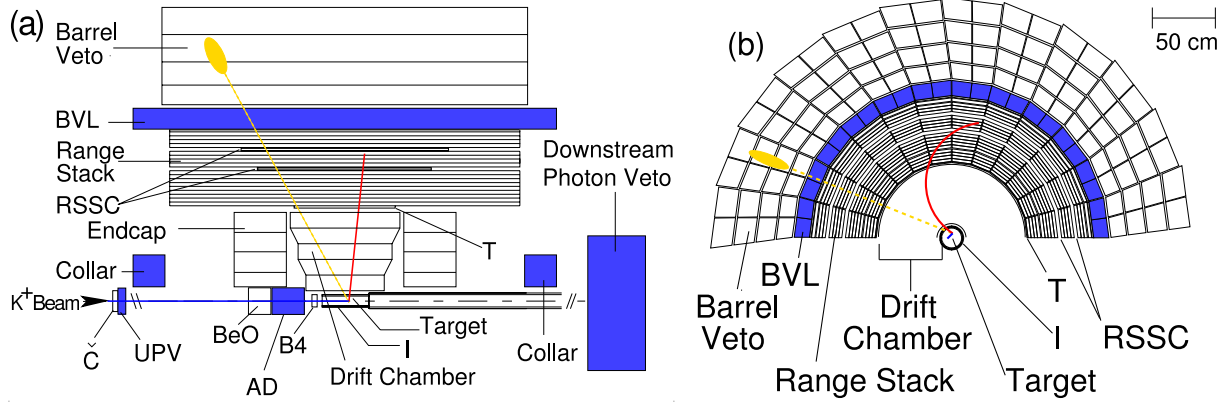


Figure 14: Schematic side (left) and end (right) views of the upper half of the E949 detector. Newly installed or upgraded photon detectors for E949 are shaded in this figure.

5-mm thick plastic scintillator from inner to outer modules, respectively. The azimuthal boundaries of each sector are tilted so that photons from the decay vertex should not travel along the inactive inter-sector gaps without losing their energy in the active regions. The BV has the 14.3 radiation lengths in total. Each end of every module is read out by a PMT and the signals are recorded by an ADC and a TDC. The time resolutions of individual BV counters are found to be 1.0 ns. The resolution is limited by the sampling time of the TDCs. The fraction of the photon energy left in scintillators is about 30%.

The Barrel Veto Liner, which is newly installed for the E949, is located just outside the Range Stack and inside the Barrel Veto. The BVL, with the inner radius of 85.2 cm and the outer radius of 93.5 cm, consists of 48 azimuthal sectors; each sector consists of 12 layers of 1-mm thick lead and 5-mm thick plastic scintillators. The BVL has 2.3 radiation lengths in total. The length of the BVL (2.2 m) is larger than that of the BV, so that the BVL adds active material to the region where the radiation length is relatively small. Each end of each module is read out by a PMT and the signals are recorded by an ADC and a TDC. Groups of adjacent sectors in each end are read by the TDs. The time resolutions of the individual BVL counters are found to be 0.5 ns. Their resolution is also limited by the TDC sampling time¹. The fraction of the photon energy, detected by scintillator, is about 30%.

The End Cap photon detector [37] is located in the 1 Tesla magnetic field and covers roughly one-third of the 4π sr photon coverage. The End Cap is exposed in a high counting-rate environment near the beam line; beam particles cause many hits that are not coincident with kaon decays. These hits from beam particles may mask photons from $K_{\pi 2}$ decays in the case that an accidental hit arises earlier than the photon hit (see Figure 15). The upstream End Cap detector consists of 75 undoped Cesium Iodide (CsI) crystals segmented to the four rings (13, 14, 21 and 27 crystals from the inner to outer rings, respectively), and the downstream End Cap detector consists of 68 crystals in the

¹The BVL's TDCs have shorter sampling times.

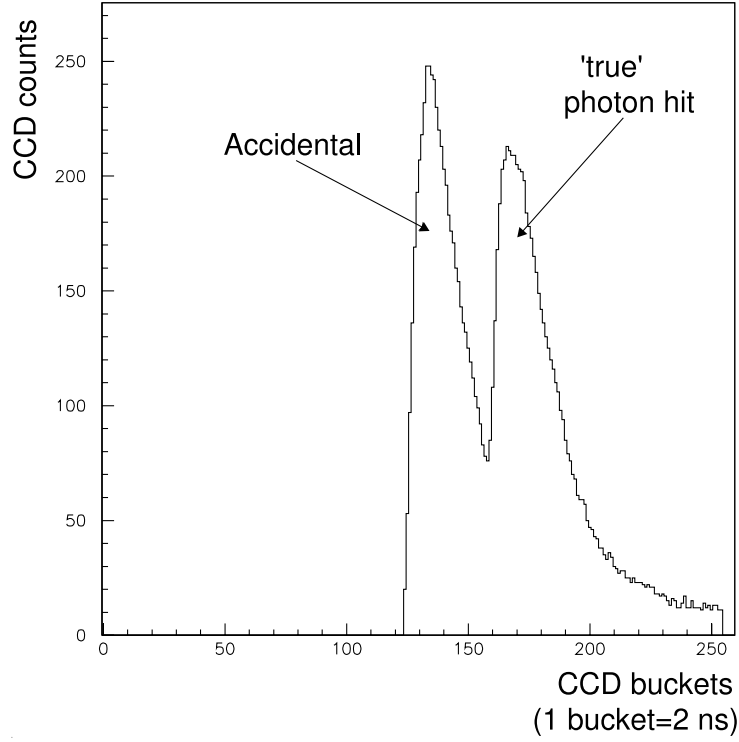


Figure 15: Pulses recorded in the End Cap CCD. The first pulse is due to an early accidental hit and the second pulse is due to the photon from $K_{\pi 2}$ decays.

four rings (11, 13, 19 and 25 from inner to outer rings, respectively). A total of 143 crystals with a pentagonal cross-section are used (Figure 16). Each crystal has a length of 25 cm (13.5 radiation lengths) and the whole End Cap detector is designed to minimize photon escape through its radial cracks. Fine-mesh PMTs [38], which maintain high gains in strong magnetic fields, are attached directly to the crystals to achieve efficient light collection (Figure 16). Only the fast component of the CsI light output with a decay time of a few tens of nanosecond at a wavelength of 305 nm is selected by ultraviolet (UV) transmitting optical filters. The PMT signals are read out by ADCs, TDCs, and CCDs. The pulses recorded in the CCDs are used to separate two pulses close in time by using a pulse-finding algorithm, which can reduce accidental vetoes and photon inefficiencies.

There are other photon detectors. The Collar, Microcollar, Upstream Photon Veto (UPV), Downstream Photon Veto (DPV), and Ring Veto (RV) are located around the beam line and cover the region with small angles around the beam line. They can detect photons that are emitted toward the beam line and which can not be detected by the BV, BVL, EC and RS.

2.7 Trigger and DAQ

About 3.9×10^6 kaons enter the E949 target for a 2.2-second long spill once every 5.4 seconds. The information on an incoming kaon and a secondary charged track (and photons) is recorded by ADCs, TDCs, CCDs and TDs of various detector subsystems. The trigger selects signal-like events out of all kaon decays. Digitized information of the

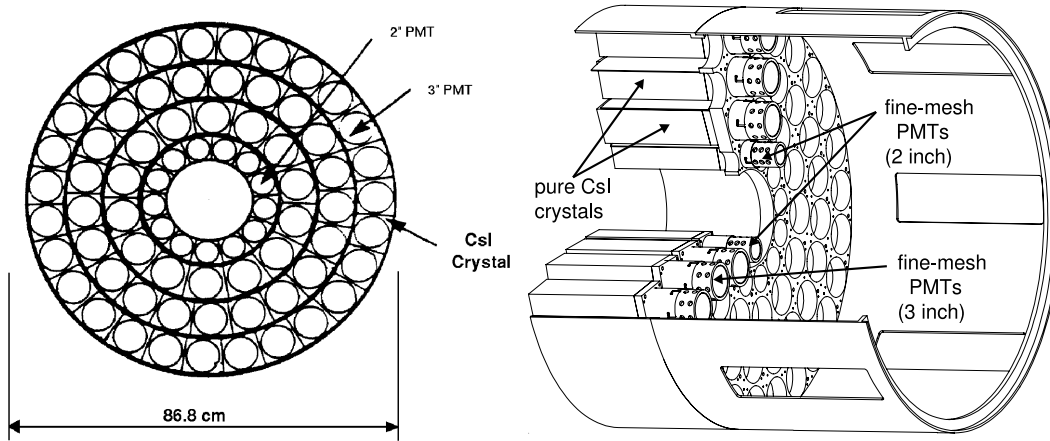


Figure 16: End view (left) and back view (right) of the End Cap.

selected events, which correspond to 70-80 Kbyte of data per event, is transferred from the electronics hut to the main computer for data taking.

The trigger is composed of a fast level-0 trigger and level-1.1 and -1.2 triggers. The level-0 trigger makes decisions entirely with logic pulses from detectors. The level-0 trigger has a rejection of 10^3 and introduces 38 ns of dead time for every coincident hit in the first two layers of the Range Stack (T-2). The level-1.1 and -1.2 triggers involve partial processing of ADC and TD data, and operate on the lower rate events that pass the level-0 trigger. The level-1.1 trigger has a rejection of 12 after level-0, and introduces 10 to 20 μ s of dead time per level-0 trigger. The level-1.2 trigger has a rejection of 2 after level-1.1 and introduces a dead time of up to 100 μ s per level-1.1 trigger. The entire trigger for $K^+ \rightarrow \pi^+ \nu \bar{\nu}$ therefore has a rejection of 24000, and reduces the 2.6×10^6 kaon decays to 100 events per spill.

3 Triggers and data sample

BNL-E949 collects data with triggers for both $K^+ \rightarrow \pi^+ \nu \bar{\nu}$ signal and background. The later are prescaled and used for the purpose of calibration and measurement of acceptance. In this paper, the triggers for background are called as “monitor sample”.

3.1 Trigger logic

BNL-E949 has three levels of trigger, including a fast level-0 trigger, Level 1.1 and Level 1.2. The level-0 trigger makes decisions entirely with logic pulses from all the detector systems. The level-1.1 and level-1.2 triggers involve partial processing of ADC and TD data, and operate on the lower rate events that pass the level-0 trigger. Trigger conditions for $K^+ \rightarrow \pi^+ \nu \bar{\nu}$ are designed differently according to its pion momentum region. For the

high pion momentum part, the trigger condition, called as $\pi^+\nu\bar{\nu}(1)$, is defined as follows

$$\begin{aligned}
K^+ \rightarrow \pi^+\nu\bar{\nu}(1) = & K_B \cdot DC \cdot (T \cdot 2) \\
& \cdot (6_{ct} + 7_{ct}) \cdot \overline{19_{ct}} \cdot RR \cdot \overline{L0rr1} \\
& \cdot \overline{(BV + BVL + EC)} \cdot HEX \\
& \cdot L1.1 \cdot L1.2
\end{aligned} \tag{15}$$

Where K_B requires that a K^+ in the beam enters the target, and DC is the online Delayed Coincidence bit which requires that the time of the outgoing pion is at least 1.5ns later than the time of the incoming kaon. The $T \cdot 2$ signal is a coincidence of the first and second layer of the RS in the same sector, which ensures the pion enters the RS. The trigger bit $6_{ct} + 7_{ct}$ requires that pion reaches the 6th or 7th layer of the RS and suppresses the $K^+ \rightarrow \pi^+\pi^-\pi^+$ or $K^+ \rightarrow \pi^+\pi^0\pi^0$ backgrounds. The $\overline{19_{ct}}$ signal requires that the pion does not reach the 19th layer, in order to suppresses $K^+ \rightarrow \mu^+\nu_\mu$ (called $K_{\mu 2}$) background. The “ct” designates the RS sectors that are associated with a $T \cdot 2$ ($T \cdot 2$ sector plus the next two clockwise sectors: this is the direction that a positive particle moves in the magnetic field). The RR bit is a refined range of the charged track calculated from the online information which rejects events with long range such as μ^+ from $K_{\mu 2}$ decay. $\overline{BV + BVL + EC}$ and HEX are online photon bits from the barrel region, Endcap region and RS, respectively, which remove events with photons such as $K^+ \rightarrow \pi^+\pi^0$ (called $K_{\pi 2}$) or $K^+ \rightarrow \mu^+\nu_\mu\gamma$. $\overline{L0rr1}$ is an online fiducial cut on the z-position of the high-momentum charged track. $L1.1$ and $L1.2$ are for Level 1.1 and Level 1.2 triggers, which involve the processing of TD and ADC data with a longer decision time but at the lower rate of events that pass the fast Level-0 trigger.

For the low pion momentum part, the trigger condition, called as $\pi^+\nu\bar{\nu}(2)$, is defined as follows

$$\begin{aligned}
K^+ \rightarrow \pi^+\nu\bar{\nu}(2) = & K_B \cdot DC \cdot (T \cdot 2) \\
& \cdot 3_{ct} \cdot 4_{ct} \cdot 5_{ct} \cdot 6_{ct} \cdot \overline{(13_{ct} + \dots + 18_{ct})} \cdot \overline{19_{ct}} \\
& \cdot L0rr2 \cdot \overline{(BV + BVL + EC)} \cdot HEX \\
& \cdot L1.1 \cdot L1.2 \cdot (ps16 + \overline{C_\pi})
\end{aligned} \tag{16}$$

Where $L0rr2$ is an online fiducial cut on the z-position of the low-momentum charged track.

In addition to the $K^+ \rightarrow \pi^+\nu\bar{\nu}$ trigger, there are monitor triggers for the purpose of calibration and normalization, and triggers for other physics modes. All triggers are prescaled except for the $K^+ \rightarrow \pi^+\nu\bar{\nu}$ trigger. All trigger decisions, defined as combinational logic on Level-0 trigger bits, are performed by the L0 trigger board.

3.2 $K^+ \rightarrow \pi^+\nu\bar{\nu}$ data sample

The BNL-E949 experiment has its first physics runs for 12 weeks from March to June in 2002, about 20% out of the approved beam time by DOE. The data collected on disk in this run period corresponds to 1.77×10^{12} kaons exposure in the target. The $K^+ \rightarrow \pi^+\nu\bar{\nu}$ data sample are classified into two categories: the momentum region above and below the $K_{\pi 2}$ peak, referred as $\pi^+\nu\bar{\nu}(1)$ and $\pi^+\nu\bar{\nu}(2)$ sample.

3.3 Calibration samples

To monitor the detector performance, BNL-E949 also has other triggers for $K_{\pi 2}$, $K_{\mu 2}$, pion beam and kaon beam samples. These so-called monitor samples are used for calibration and acceptance studies. They are taken simultaneously with the $\pi\nu\bar{\nu}$ triggers and are prescaled down to a level of one event/per spill.

3.3.1 $K_{\mu 2}$ monitor

The $K_{\mu 2}$ decay has the largest branching ratio. The final state does not contain photon, the daughter muon does not interact with the nuclei. Therefore, the sample is clean and can be used for the detector calibration. In addition, this sample can be used for the acceptance study and for the normalization to the $K_{\mu 2}$ branching ratio. The trigger condition for $K^+ \rightarrow \mu^+ \nu_\mu$ is defined as follows

$$K^+ \rightarrow \mu^+ \nu_\mu = KB \cdot (T \cdot 2) \cdot (6_{ct} + 7_{ct}) \cdot \overline{17_{ct} + 18_{ct} + 19_{ct}} \quad (17)$$

3.3.2 $K_{\pi 2}$ monitor

The final state of this decay mode contains one charged pion and two photons from π^0 decay. Since the pion momentum is monochronic, it can be used to check the measurements of charged track momentum, range and energy. Also the pion can be used to study the particle identification, and the photons can be used to study the photon veto. The trigger condition for $K^+ \rightarrow \pi^+ \pi^0$ is defined as follows

$$K^+ \rightarrow \pi^+ \pi^0 = KB \cdot (T \cdot 2) \cdot (6_{ct} + 7_{ct}) \cdot \overline{19_{ct}} \quad (18)$$

3.3.3 Beam pion monitor

Among the incoming beam particles, there are still some pions. These beam pions can be identified by the Cherenkov counters. The selected pions undergo scattering in the target and change their flight direction from downstream to the effective detector region. Therefore, the kinematic feature of this pion sample is almost the same as the signal $K^+ \rightarrow \pi^+ \nu\bar{\nu}$ except that the target pattern is different. This sample is suitable for calibrating the dE/dx and for studying the relevant acceptance wherever possible. The trigger condition for the beam pion is defined as follows

$$\text{Beam pion} = \frac{\pi B \cdot \overline{\text{DCIC}} \cdot (T \cdot 2)}{\cdot (\overline{BV + BVL + EC}) \cdot HEX} \quad (19)$$

3.3.4 Kaon beam monitor

In the kaon beam monitor, only the kaon Cerenkov counters are involved. Therefore, this monitor sample can be used to evaluate the individual trigger efficiency. The trigger condition for the kaon beam monitor is defined as follows

$$\text{Beam kaon} = KB \quad (20)$$

3.3.5 Charge exchange monitor

Charge exchange process (CEX) of $K^+n \rightarrow p + K_L^0$, $K_L^0 \rightarrow \pi^+l^-\overline{\nu_l}$ can affect the signal search when low momentum charge lepton is undetected. The main issue for this background study is that how to precisely obtain the corresponding reaction rate. Since K^0 has equal fraction for K_L^0 and K_S^0 , there is no difference between $K^+n \rightarrow p + K_L^0$ and $K^+n \rightarrow p + K_S^0$. The K_S^0 decaying to $\pi^+\pi^-$ can be well detected. Using the decay rate measured from the $K^+n \rightarrow p + K_S^0$ can be applied to the $K^+n \rightarrow p + K_L^0$. The trigger condition for charge exchange process (CEX) of $K^+n \rightarrow p + K_S^0$, $K_S^0 \rightarrow \pi^+\pi^-$ is defined as

$$\text{CEX} = KB \cdot \overline{DC} \cdot 2(T \cdot 2) \cdot (6_{ct} + 7_{ct}) \cdot \overline{EC + \pi B} \quad (21)$$

3.3.6 Cosmic ray

High energy cosmic ray can go through the whole detector with almost no deflection, and thus leaving a stright line in the detector when the magnetic field is off. This feature of high energy cosmic ray can be used for UTC geometrical alignment. The trigger condition requires

$$\text{Cosmic} = T \cdot 2 \cdot IC \cdot \overline{BG} \text{ or } T \cdot 2 \cdot (> 1 \text{ non} - \text{adj } IC) \quad (22)$$

3.4 Monte Carlo Simulation

The detector and the physics processes in it are modeled by a Monte Carlo (MC) simulation program, which is an amalgam of subroutines from the EGS package and a number of routines written specially for this detector. The MC includes all of the detector elements, except for the beam instrumentation upstream of the target. It generates data, except for the TD and CCD pulse-shape information. The simulation of kaon decays in the E949 detector starts from a "beam file" with the x, y, z positions of kaon decays in the target obtained from an analysis of $K_{\mu 2}$ decays.

Multiple Coulomb scatterings of charged particles with various nuclei in the detector are calculated according to the theory of Moliere [39], with corrections for the spin of the scattered particle and the form factor of the nucleus [40]. Hadronic interactions of positively charged pions in the plastic scintillators are calculated using a combination of data and phenomenological models [41]. Photon and electron interactions are calculated using the EGS4 electromagnetic-shower simulation package [42].

The accuracy and the performance of the MC are verified by comparing the different kinematic variables from data and MC for $K_{\pi 2}$ and $K_{\mu 2}$ decays.

4 Data collection and processing

4.1 Data collection

(to be written)

4.2 Event reconstruction and data processing

The data collected by the trigger are analyzed by a series of offline software programs. Event reconstruction starts from investigations of the trigger bit and of such information as the online stopping counter. Then, hit counters of a positively-charged track (track counters) are searched for in the Range Stack. The search starts from finding a (offline) T·2 sector. If there are coincident hits in the first two RS layers in the same sector, it is treated as the T·2 sector. Otherwise, the online T·2 sector is used. The counters that are coincident with the T·2 hit are searched for in the outgoing and clockwise direction, and such counters are treated as track counters. The average time of the track counters is defined as the "track time". The counter in the outermost layer and the most clockwise sector is treated as the offline stopping counter.

Track reconstructions in the target and UTC are performed twice. At first, in x-y plane, a circular track is fitted to the UTC hit wires. The fitted track is extrapolated to the target to determine the target fibers that belong to the track (pion fibers) and the kaon decay vertex. Pattern recognition in the target is conducted to determine the kaon and pion fibers using the UTC track information. Once the pion fibers are found, the UTC fitting is repeated with the information on the pion passage and kaon decay vertex in the target, in order to have a better solution for the left-right ambiguity in the UTC measurement. The pattern recognition is also re-done after the UTC track fitting is finalized. The times of the mother kaon and the daughter pion are obtained from the average of the kaon and pion fiber times, respectively, while the corresponding energies are the sums of the energy deposits in the kaon and pion fibers. The total momentum is obtained by correcting the momentum in the UTC by the target range, the I-Counter range and the amount of dead materials due to the inner wall of the UTC.

In the stopping counter, a pulse fitting is performed to find a $\pi^+ \rightarrow \mu^+$ decay signature. Both single-pulse and double-pulse fittings are applied to the TD pulse shape and the fitting algorithm returns the χ^2 of both single-pulse and double-pulse fittings, the energy and time of the second pulse, etc.

The total energy deposit of the track in the RS is obtained by summing up the energy deposits in the track counters. The muon energy in the stopping counter is subtracted from the total energy using the result from the TD pulse fit to the stopping counter. The range of the track is calculated via a track-fitting method, taking into account that a track is propagated by losing energy with Bethe-Block equation and by bending in a 1 Tesla magnetic field. A projection of the track onto the x-y plane is fitted to the sector crossing points, the RSSC hit positions and the energy in the stopping counter by changing the incident momentum and the angle at the entrance of the RS until the fitting χ^2 is minimized (see Figure 17). The projection of the track onto the r-z plane is from the extrapolation of the UTC track to the center of stopping counter. In the r-z plane, a

Cuts	$K_{\pi 2}$ enhanced	Muon enhanced	Beam enhanced
Target reconstruction cut	✓	✓	✓
Photon veto cut		✓	✓
$\pi^+ \rightarrow \mu^+$ double pulse fitting cut	✓		✓
Beam dE/dx & extra beam cut	✓	✓	
Target photon veto		✓	✓
Delayed coincidence cut		✓	
$\pi_{scatter}$ selection cut			✓

Table 2: Pass 2 cuts to produce the $K_{\pi 2}$, muon and beam enhanced background samples. The photon veto cut means photon veto in the BV, BVL, EC and RS. The $\pi_{scatter}$ selection cut selects those events with prompt decay timings and with any activities in the target.

matching of the extrapolated track to the measured z positions, obtained from the end-to-end time differences in the individual RSSCs and the RS counters, is examined. The range in the RS is calculated from the path length of the fitted track, and the total range of the track is calculated by adding the target range, the I-Counter range and the range in the dead materials.

Data collected by the $\pi\nu\bar{\nu}(1)$ trigger are stored on 300 magnetic tapes with a total data size up to 7 Tera bytes. In order to reduce the data to a reasonable size, two steps of data reductions are taken prior to the background study. In the first step, called "Pass 1", badly reconstructed events and obvious muon and beam background events are removed by several cuts which maintain high acceptance for $K^+ \rightarrow \pi^+\nu\bar{\nu}$ events. This "Pass 1" processing reduces the data by a factor of 10. In the second step, called "Pass 2", some loose versions of the final analysis cuts are applied to the "Pass 1" output data sample. In the "Pass 2" data reduction, some combinations of the "Pass 2" cuts are used to divide the data sample into 3 groups: $K_{\pi 2}$ enhanced, muon enhanced and beam enhanced background samples. The "Pass 2" cuts are tabulated in Table 2. The developments of the Bifurcation cuts and the background estimations are performed with the Pass 2 output data sample.

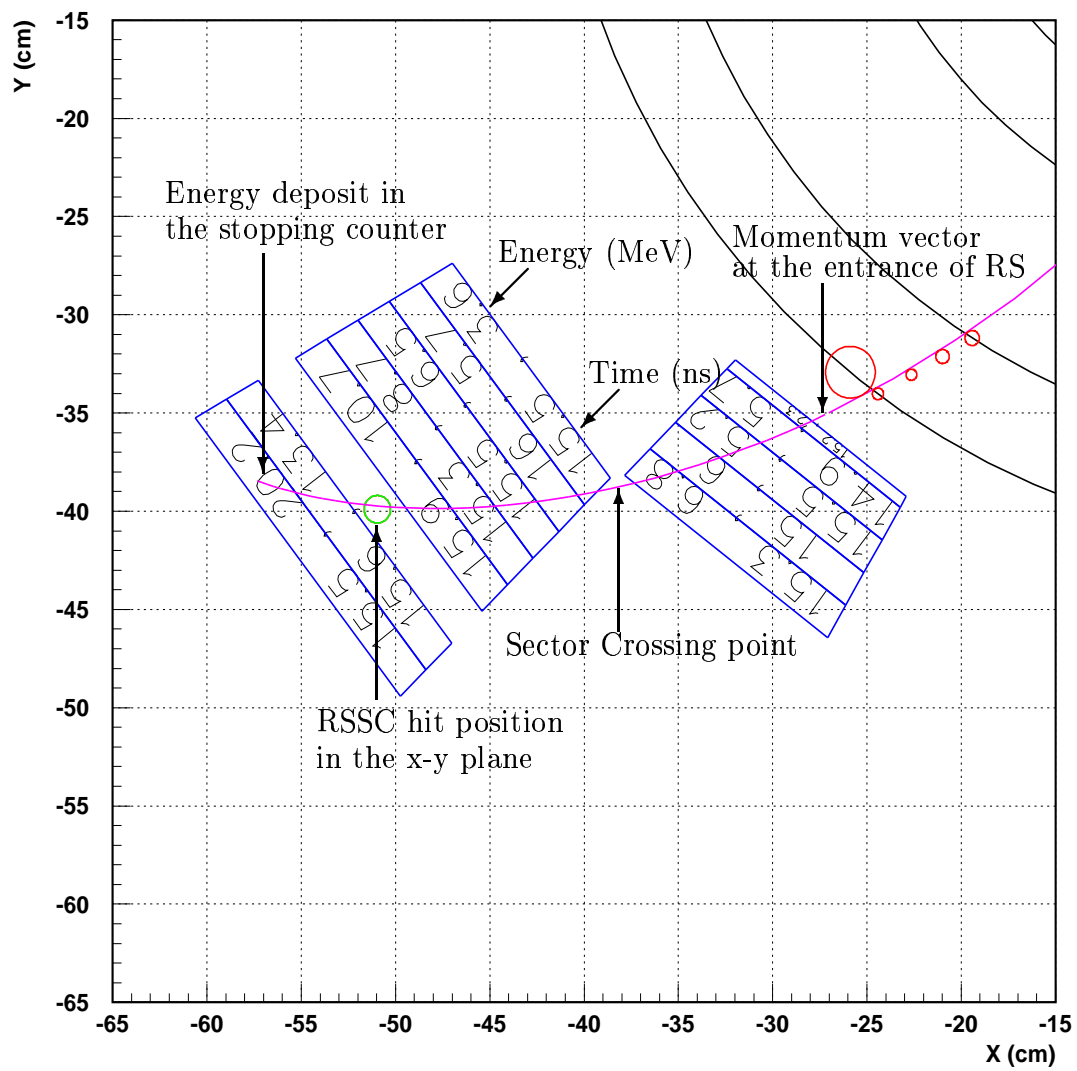


Figure 17: Range Stack track fitting in the x-y plane.

5 Selection criteria and data analysis

In this section, issues concerning offline analysis, particularly the characteristics of the backgrounds that pass the online trigger conditions, the signal selection criteria (cuts) used to suppress them, and the methods used to perform the offline analysis, are described.

5.1 Background Overview

The branching ratio of the $K^+ \rightarrow \pi^+ \nu \bar{\nu}$ decay is expected to be 10^{-10} in the Standard Model. Considering the acceptance factors of the analysis, more than 10^{12} kaons have to decay in the apparatus so that one candidate event can be observed. The backgrounds should be suppressed to be less than one event in order to have confidence that the candidate event really comes from the $K^+ \rightarrow \pi^+ \nu \bar{\nu}$ decay. Although the trigger already overwhelmingly suppresses the backgrounds, the data accumulated by the trigger still contain many background events. It is therefore important to investigate the backgrounds that pass the trigger and to understand their characteristics.

Figure 18 shows the range in a plastic scintillator (in cm) versus the momentum (in MeV/c) of charged particles for the events that pass the $K^+ \rightarrow \pi^+ \nu \bar{\nu}(1)$ or $K^+ \rightarrow \pi^+ \nu \bar{\nu}(2)$ trigger. In this figure, there are various sources of background. Events in the $K_{\pi 2}$ peak are due to π^+ tracks from $K^+ \rightarrow \pi^+ \pi^0$ decays with a momentum of 205 MeV/c, an energy of 108 MeV and a range of 30 cm. Events in the $K_{\mu 2}$ peak are due to μ^+ tracks from $K^+ \rightarrow \mu^+ \nu_\mu$ decays with a momentum of 236 MeV/c, an energy of 153 MeV and a range of 55 cm. Both events in the $K_{\pi 2}$ range tail and events in the $K_{\mu 2}$ range tail ($K_{\mu 2}$ Range Tail events) have ranges (and energy) smaller than that expected from these decays, due to elastic (inelastic) scattering in the Range Stack. Events in the muon band (Muon Band events) are due to multi-body decays, such as $K^+ \rightarrow \mu^+ \nu_\mu \gamma$ (radiative $K_{\mu 2}$, or $K_{\mu \nu \gamma}$) and $K^+ \rightarrow \mu^+ \pi^0 \nu_\mu$ ($K_{\mu 3}$), π^+ decay in flight in the target, and $K_{\mu 2}$ decay with inelastic scattering in the target, such that the range, energy and momentum are all smaller than the $K_{\mu 2}$ peak values. The momentum end points of the $K_{\mu \nu \gamma}$ and $K_{\mu 3}$ decays are 236 MeV/c and 215 MeV/c, respectively. Events in the pion band are due to pions in the beam that scatter into the Range Stack.

The backgrounds can be categorized into two types: backgrounds that arise from K^+ decays and those from beam particles. The K^+ -originated backgrounds can be further categorized into two types based on the particle type: π^+ -related and μ^+ -related backgrounds. As shown in Figure 4, the K^+ -originated backgrounds from the multi-body decays are suppressed by choosing a momentum region higher than the $K_{\pi 2}$ peak for the signal region. They can also be suppressed by not allowing photon activities, since some of them include π^0 's in their decay. The remaining and most contributing backgrounds from K^+ decays are therefore $K_{\pi 2}$ and $K_{\mu 2}$. The momentum, energy and range distributions for the $K_{\pi 2}$ and $K_{\mu 2}$ are shown in Figure 19. $K_{\mu \nu \gamma}$ can also be one of main backgrounds because the momentum of the decay could be in the signal region.

A $K_{\pi 2}$ event can fake a $K^+ \rightarrow \pi^+ \nu \bar{\nu}$ if the momentum, energy and range cannot be well measured and two photons from the π^0 decay are missed in the detection. This background can be removed by setting a lower boundary of the signal region above the $K_{\pi 2}$ peaks. The $K_{\pi 2}$ events are also suppressed by requiring no photon activity in the

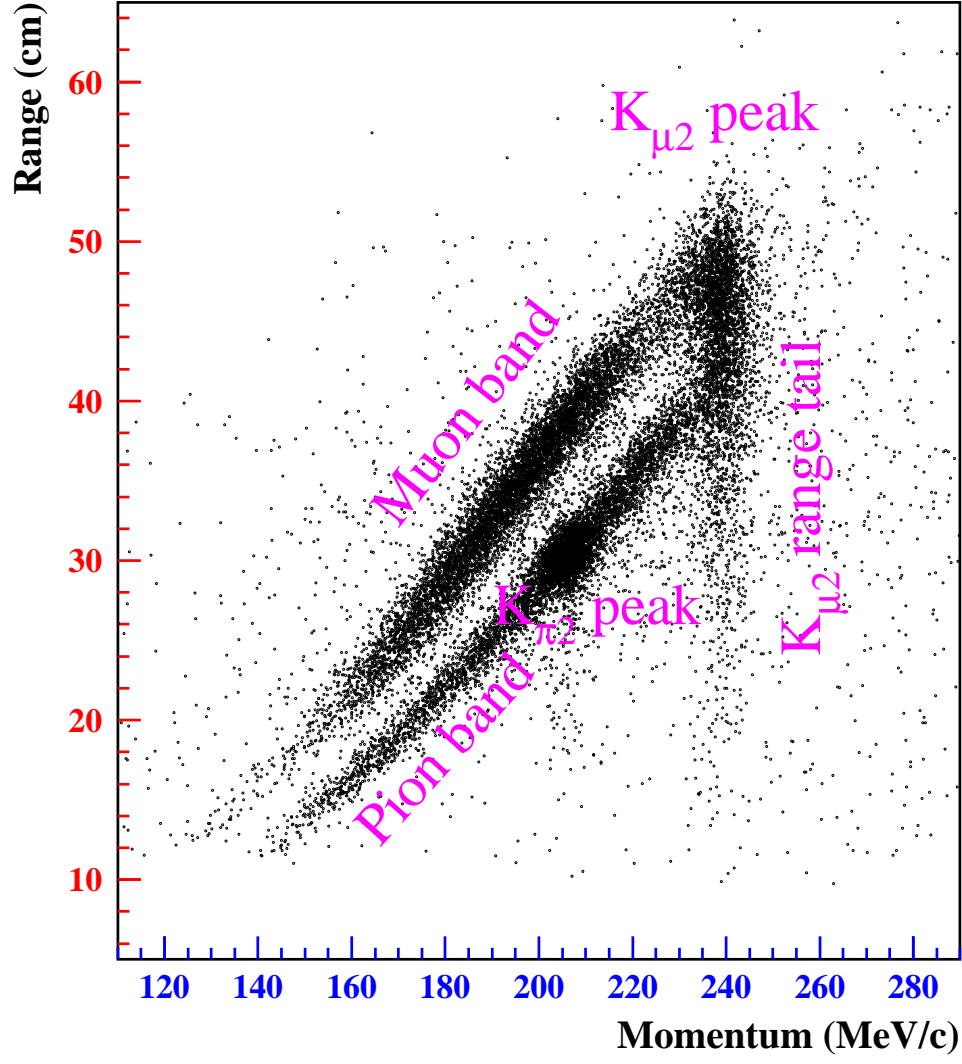


Figure 18: Range in a plastic scintillator (in cm, y -axis) and the momentum (in MeV/c, x -axis) of the charged particles for events that pass the $K^+ \rightarrow \pi^+ \nu \bar{\nu}(1)$ or $K^+ \rightarrow \pi^+ \nu \bar{\nu}(2)$ trigger.

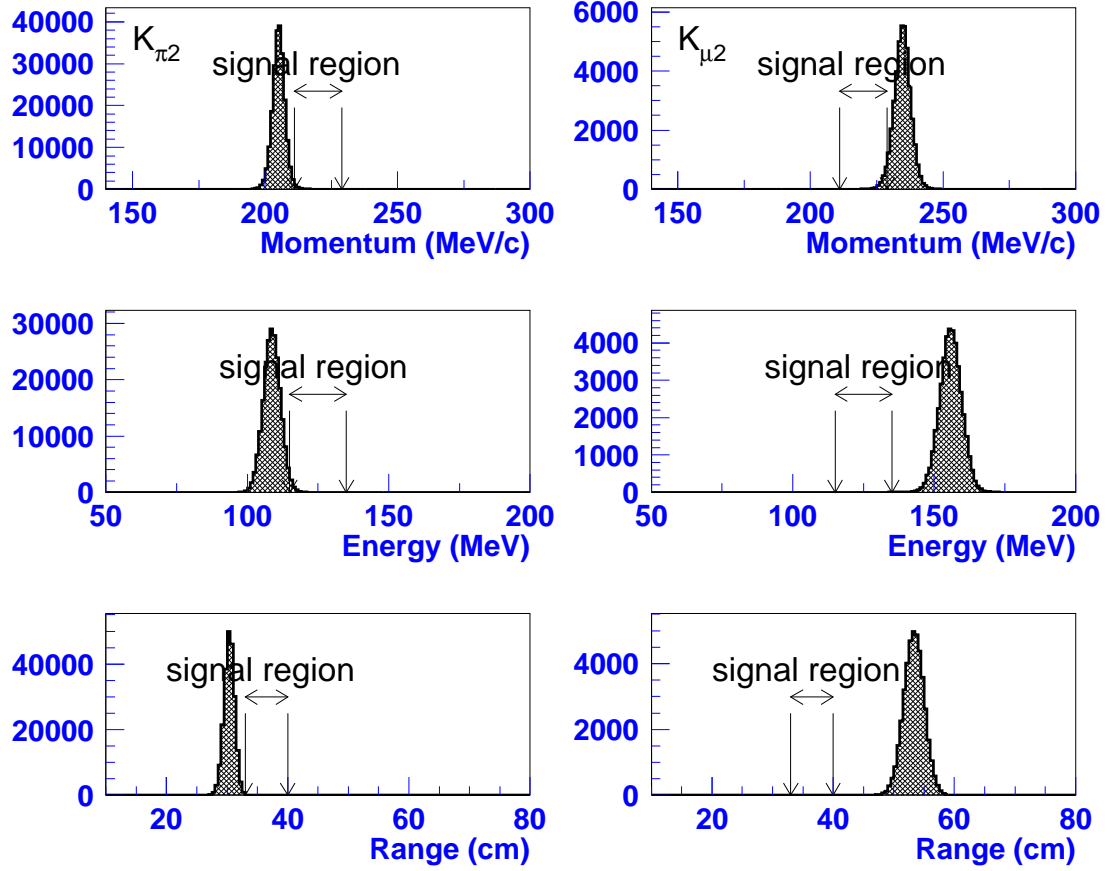


Figure 19: Momentum (top), energy (middle) and range (bottom) distributions for the $K_{\pi 2}$ (left column) and $K_{\mu 2}$ (right column) decays. The arrows indicate the boundaries of the signal region.

detector. The energy of photons from $\pi^0 \rightarrow \gamma\gamma$ in the $K_{\pi 2}$ decay is evenly distributed in the region $20.2 < E_\gamma < 225.3$ MeV. The $K_{\pi 2}$ events have been removed by an online photon veto in the trigger. The online rejection against $K_{\pi 2}$ events is on the order of 10^4 . A further rejection of 10^2 is needed to suppress the $K_{\pi 2}$ background to much less than one event. Offline photon veto is performed by imposing timing windows with respect to the charged track timing and the energy thresholds to the photon hits.

A event in the $K_{\mu 2}$ momentum peak can fake a $K^+ \rightarrow \pi^+ \nu \bar{\nu}$ if the momentum, energy and range cannot be well measured and the μ^+ is misidentified as a π^+ . This background can be removed by applying the cuts on the kinematic values. The upper bound of the signal region is set at a momentum of 229 MeV/c, an energy of 135 MeV and a range of 40 cm. The upper bound for the momentum is set at about 2σ apart from the $K_{\mu 2}$ peak; those for the energy and range are much away from the peaks. The events in the $K_{\mu 2}$ peak can therefore hardly contribute to the signal region. On the contrary, the $K_{\mu 2}$ Range Tail events have the same momentum as that in the $K_{\mu 2}$ peak, but their energy and range can be shifted into the signal region due to the muon scattering effect in the RS. In this case, only a cut on the upper bound of the momentum at 2σ works. Thus, the contribution of the $K_{\mu 2}$ Range Tail events to the signal region is supposed to be larger than the other sources of the background. The Muon Band events, particularly the $K_{\mu\nu\gamma}$ decay, can also sneak into the signal region. These momentum and energy fall into the signal region, but the range for the μ^+ 's is slightly longer than that for the π^+ 's at a given value of the momentum (see Figure 18). The Muon Band events are thereby removed by requiring acut on the relation between the range and the momentum expected for the π^+ tracks. The details of this cut are described in Section 5.4. These μ^+ -related backgrounds (referred to as "Muon background") can also be removed by observing the signature of a $\pi^+ \rightarrow \mu^+ \rightarrow e^+$ decay sequence in and around the stopping counter. However, if the $\mu^+ \rightarrow e^+$ decay has an additional accidental hit, the Muon background can fake a $\pi^+ \rightarrow \mu^+ \rightarrow e^+$ decay sequence, and thus needs a rejection to it. The details are described in Section 5.5.

The non- K^+ decay backgrounds are categorized into three types: Single Beam background, Double Beam background, and charge exchange interaction background (referred to as "CEX" background).

The Single Beam background can be further categorized into two cases; kaon entering and pion entering cases. If a single kaon entering the apparatus decays in flight (DIF) to π^+ and π^0 ($K_{\pi 2}$ DIF, see the top diagram in Figure 20), the kinematic values of the π^+ can be shifted upward due to the Lorentz boost. If the two photons from the $K_{\pi 2}$ DIF are missed, such an event can fake a $K^+ \rightarrow \pi^+ \nu \bar{\nu}$ signal. The kaon DIF events tend to have earlier decay timings in the target than the stopped kaon decay events. The Single Kaon Beam background is suppressed by imposing a delayed coincidence (DC) to the decay time. If a pion in the beam scatters in the target and then enters the fiducial region of the detector (Pion Scattering events, see the bottom diagram in Figure 20), the event can fake a the $K^+ \rightarrow \pi^+ \nu \bar{\nu}$ signal because some of these scattered pions satisfy the kinematics of the signal. The scattered pion leaves the target immediately after entering the target. The Single Pion Beam background can be suppressed by the DC and the kaon identification using the Čerenkov counter and the B4 Hodoscope measurements.

The Double Beam background can be categorized into two; kaon-kaon entering and

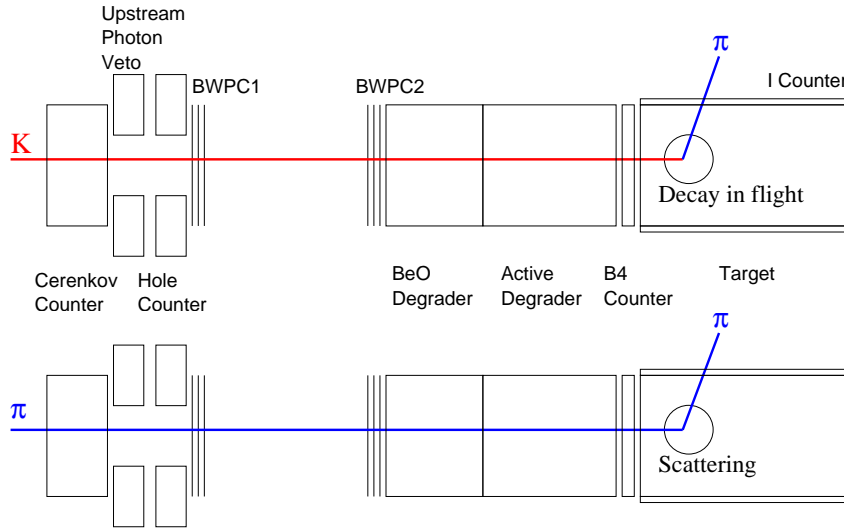


Figure 20: Schematic diagrams of the Single Beam background: a Single Kaon Beam background (top) and a Single Pion Beam background (bottom).

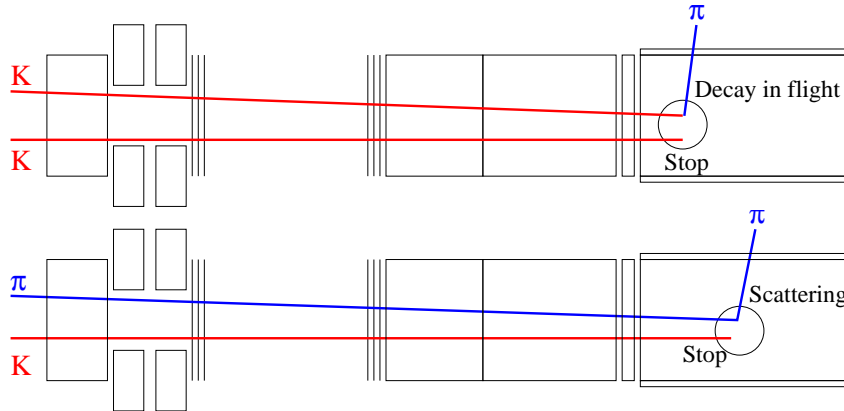


Figure 21: Schematic diagrams of the Double Beam background: a $K - K$ Double Beam background (top) and a $K - \pi$ Double Beam background (bottom).

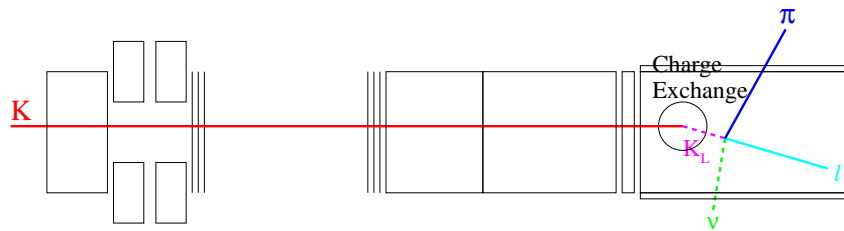


Figure 22: Schematic diagram of the charge exchange interaction background.

Background	BR	kinematics	PV	PID	multi-tracks	beam PID	extra beam	DC
$K^+ \rightarrow \mu^+ \nu_\mu$	0.64	✓		✓				
$K^+ \rightarrow \pi^+ \pi^0$	0.21	✓	✓					
$K^+ \rightarrow \mu^+ \nu_\mu \gamma$	0.005	✓	✓	✓				
Single K Beam			✓					✓
Single π Beam						✓		✓
Double $K - K$ Beam			✓		✓		✓	
Double $K - \pi$ Beam					✓	✓	✓	
CEX					✓			✓

Table 3: Tools against the main backgrounds: 1) kinematics: Phase Space Cuts (P, E and R), dE/dx cuts, Range-Momentum Consistency cut; 2) PV: Photon Veto Cuts; 3) PID: $\pi^+ \rightarrow \mu^+ \rightarrow e^+$ Decay Sequence Cuts; 4) multi-tracks: veto the multi-track events; 5) beam PID: the particle identification in the beam instrumentation; 6) extra beam: veto the extra beam particles coincident with the charged track; and 7) DC: Delayed Coincidence Cuts.

kaon-pion entering cases. In the kaon-kaon entering case, the first kaon enters and stops in the target, and the second kaon entering the target decays in flight to π^+ and the π^+ enters the fiducial region of the detector (see the top diagram in Figure 21). The kaon-pion case is the same as the kaon-kaon case, except that the second pion scatters in the target and enters the fiducial region to satisfy the kinematics of the signal (see the bottom diagram in Figure 21). For both cases, the Double Beam backgrounds can imitate the $K^+ \rightarrow \pi^+ \nu \bar{\nu}$ signal, if the decay products from the first kaon are missed and the second kaon or pion is not detected in the beam line detectors. These backgrounds can be suppressed by looking for any extra activities that are coincident with the charged track in the beam instrumentation, target, and Range Stack.

The charge exchange (CEX) interaction background can occur as follows: a kaon entering the target interacts with a neutron in the carbon of the scintillators ($K^+ n \rightarrow K^0 p$) and the resultant K_L^0 decays to $\pi^+ l^- \bar{\nu}_l$, where $l^- = e^-$ or μ^- (see Figure 22). If the π^+ satisfies the signal kinematics and the l^- is missed, the event can imitate the $K^+ \rightarrow \pi^+ \nu \bar{\nu}$ signal. The K_L^0 does not deposit energy along the path in the target; the CEX background event has a gap between kaon and pion fibers in the target. It is therefore suppressed by requiring no large gap between the kaon and pion fibers. The CEX background is also suppressed by the DC, since only the K_L^0 's that travel a short distance can be allowed by requiring no large gap.

The rejection tools for each background in this experiment are tabulated in Table 3.

5.2 Analysis Strategy and Method

The predicted branching ratio for $K^+ \rightarrow \pi^+ \nu \bar{\nu}$ is at a level of 10^{-10} in the Standard Model. The backgrounds should therefore be suppressed down below this level, in order to make a measurement. This large suppression of the backgrounds challenges the prevailing background estimate methods, because any measurement involving low statistics can be subject to large statistical fluctuations. Furthermore, the development of signal selection criteria or cuts using limited statistics can result in a "bias", because the cuts designed

to remove a single event or a small number of events may not work properly on a larger data sample.

To avoid this bias, a "blind" analysis is indispensable. That is, background sources are identified *a priori* and a signal region for the $\pi^+\nu\bar{\nu}(1)$ is determined so that the sensitivity is expected to be optimized. The signal region is masked out until all the cut development and the background estimation are finalized. Cuts to suppress the backgrounds are developed using events outside the signal region.

The analysis is performed in the following way:

- Real data are used wherever possible, because a Monte Carlo simulation does not necessarily represent pathological events left over in the real data due to hardware problems or unexpected biases; these events may pass through all the cuts designed by the MC sample and mimic the $K^+ \rightarrow \pi^+\nu\bar{\nu}$ signals.
- A so-called "Bifurcation Method" is exploited to evaluate the background levels. The background is estimated by at least two uncorrelated cuts, or groups of cuts; they can be independently inverted to create high-statistic background samples from real data. The details of the Bifurcation Method are explained in Section 6.1.
- For a background study, the real data are divided into two portions: a uniformly-sampled one-third portion of the whole data is used to develop the cuts, and the remaining two-third portion is used to measure the final background levels. This helps to estimate the background levels in a less-biased manner.
- Balance between the background levels and the signal acceptances can be controlled continuously by changing the severities of the cuts used in the Bifurcation Method. The variations of the background levels and acceptances at various cut positions can be numerically tabulated to give the so-called background functions.
- Acceptance measurements of the signal selection cuts are made with some monitor trigger data. The $K^+ \rightarrow \pi^+\nu\bar{\nu}$ phase space acceptance and the π^+ stop efficiency are obtained from the Monte Carlo $K^+ \rightarrow \pi^+\nu\bar{\nu}$ sample, in which the rate of π^+ nuclear interactions in the Range Stack and π^+ decay-in-flights are both taken into account.
- The branching ratio is calculated by a likelihood analysis.

5.3 Single kaon beam selection criteria

It is crucial to require that a single kaon enters the target and decays at rest. In order to ensure these requirements, several cuts explained in the following paragraphs are prepared.

Delayed Coincidence Cuts

The (offline) Delayed Coincidence Cuts require that a kaon should decay at least 2 ns later than it enters the target, namely $t_\pi - t_K \geq 2$ ns, where t_K is the target kaon time from the average time of the target kaon fibers, and t_π is the target pion time, which

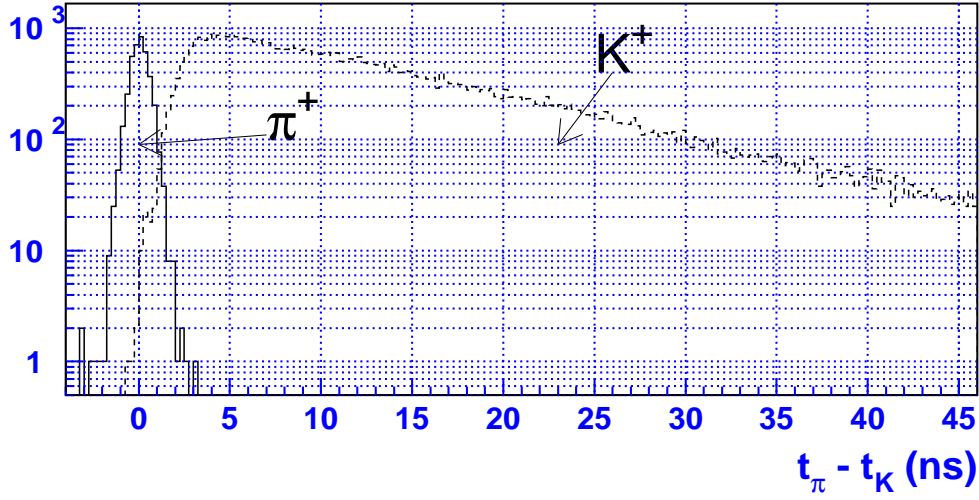


Figure 23: Distribution of the time difference, $t_\pi - t_K$, for stopped kaon (dashed) and scattered pion (solid) events. The time difference for kaons is derived from stopped kaon events in the $K_{\mu 2}$ monitor trigger data, and that for scattered pions is from Pion Scattering events in the $\pi\nu\bar{\nu}(1)$ trigger data.

is the average time of the target pion fibers. The distribution of $t_\pi - t_K$ is shown in Figure 23. The $t_\pi - t_K$ distribution for the stopped kaons shows an exponential curve with a kaon lifetime of 12 ns, while that for the scattered pions or kaons decaying in flight shows a prompt peak of around 0 ns. Most of these events are removed by the requirement $t_\pi - t_K \geq 2$ ns. Since the precision of timing measurement depends on how many fibers are hit by the pions and the kaons, a number of consistency checks are also performed between the measurement of target fibers and the measurement from the other sub-detectors, in order not to introduce any beam background due to a bad timing measurement. If there is any hint of bad consistency, the above delayed coincident cut will be tightened up to 6ns.

dE/dx Cut in the B4 Hodoscope

The dE/dx cut in the B4 Hodoscope requires that the energy deposit of an incoming beam particle is consistent with that of the kaons. The velocity of kaons, whose energy loss in the degrader is large, is $\beta \approx 0.57$, while that of pions is $\beta \approx 0.97$ [43]. Kaons (pions) therefore deposit large (small) energies in the B4 Hodoscope. The dE/dx in the B4 Hodoscope is shown in Figure 24. Events are required to satisfy the B4 dE/dx greater than 1.85 MeV. The pion events in the peak of the Landau distribution are removed by this cut.

Cuts on Extra Beam Particles at the Track Time

Timing measurement from the beam counters are first checked and compared to the track time determined by the RS. The TDC times measured by both the C_K and the C_π are used to compare with the track time determined by the RS. Events are rejected if the timing consistency is observed to be within ± 2 ns. Figure 25 show the single kaon beam

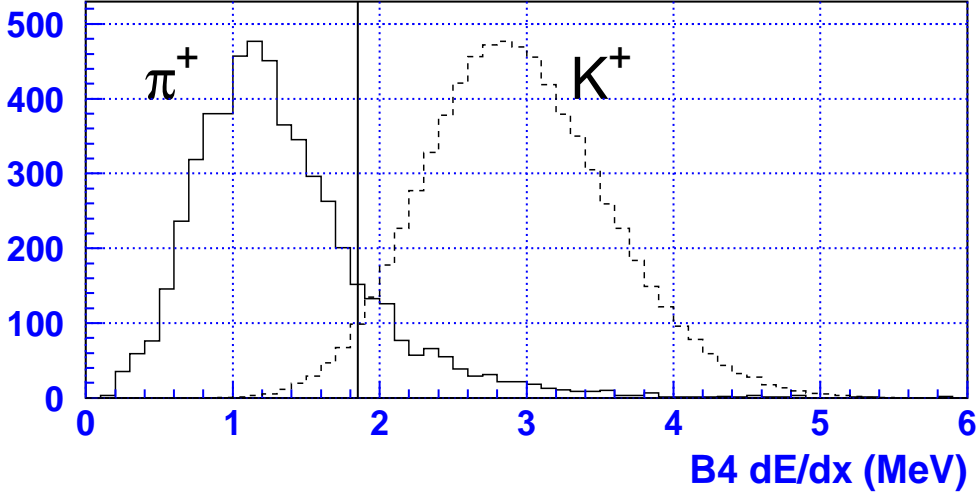


Figure 24: dE/dx in the B4 Hodoscope for beam kaons (dashed) and pions (solid). The kaon events are derived from the stopped kaon events in the $K_{\mu 2}$ trigger data and the pion events are from Pion Scattering events in the $\pi\nu\bar{\nu}(1)$ trigger data. Events with B4 dE/dx less than 1.85 MeV are rejected.

signal indicated by the $K_{\mu 2}$ monitor and the $\pi^+\nu\bar{\nu}$ triggers. Since the high incoming kaon beam intensity can cause a TDC pile-up problem, the CCD times and the TDC trailing-edge times provided by the Čerenkov counters are also used to do the same comparison with the track time. Events are rejected if the CCD times of the Čerenkov counters or the TDC trailing-edge times of C_π are consistent with the track times within $\pm 2\text{ns}$. For the TDC trailing-edge times of C_K , the timing windows vary from $\pm 2\text{ns}$ to $\pm 3.5\text{ns}$, depending on the length of kaon decay time determined by the target fibers. The rejected timing regions for the $\pi^+\nu\bar{\nu}$ triggers do not show either a $K_{\mu 2}$ momentum peak or a $K_{\pi 2}$ momentum peak, indicating that the corresponding events are not single-kaon beams. A close look into the events rejected by C_K times contains almost equal amounts of single beam background and double beam background, while the single beam background increase to about 70% in the events rejected by C_π times. Since the BWPC can provide timing measurement for the incoming beam, the times from both two chambers are also compared to the track time to see if they are within the timing windows of $\pm 4.5\text{ns}$. The TDC time and the CCD time measured by the B4 Hodoscope are also compared to the track time. Events are rejected if the average TDC time of hit modules is within $\pm 2.5\text{ns}$ of the track time, or the the average CCD time of hit modules is within $\pm 1.5\text{ns}$ of the track time. The CCD pulse shape recored by the B4 Hodoscope is fitted with a double-pulse assumption. Events are rejected if a signature of double pulses and the time for the corresponding second pulse agrees with the track time within $\pm 3.5\text{ns}$.

Beam Likelihood Cut

Kaons, which come to rest in the target, satisfy a relation between the energy deposits in the B4 Hodoscope (B4 dE/dx), the energy deposits in the target (E_K) and the stopping z positions, which are related to the kaon path length ($Z_{K\text{stop}}$). The stopping z position

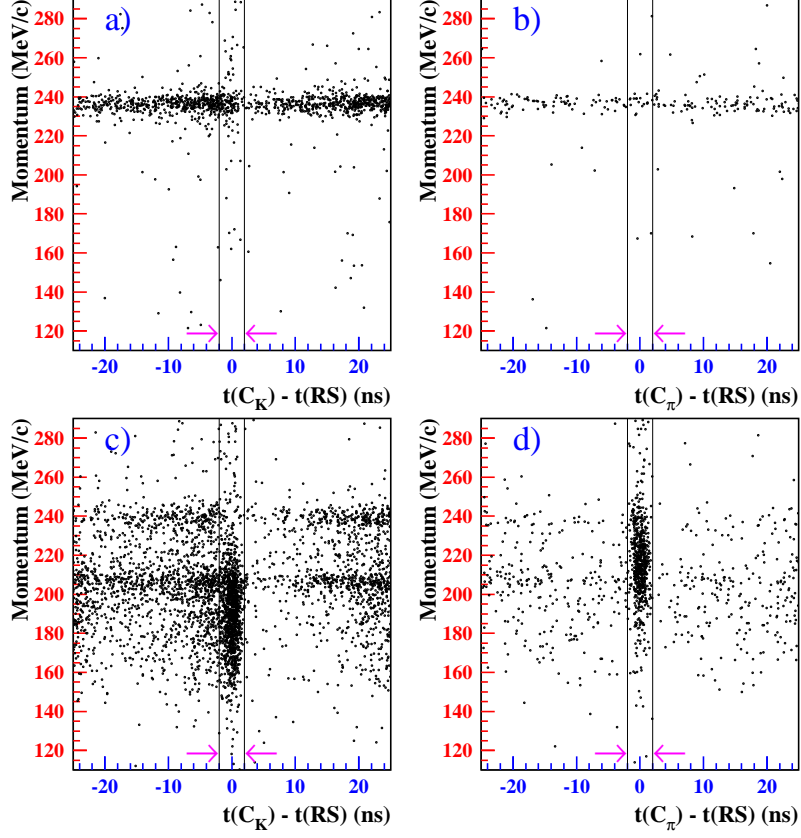


Figure 25: The momentum of charged particle versus the TDC time given by the Čerenkov counters relative to that given by the RS. $K_{\mu 2}$ monitor is used for representing the single kaon beam events as shown in a) and b). The corresponding plots for the events in $\pi^+\nu\bar{\nu}$ triggers are shown in c) and d). The arrows indicate the rejected timing regions with beam background contamination. The statistics in these plots for $\pi^+\nu\bar{\nu}$ triggers accounts for about 0.1% of total kaon flux.

for the kaon can be well measured by the target and can only be derived by extrapolating the UTC track to the decay vertex using the x-y position measurement in the target. The stopping z positions for scattered pions and kaons decaying in flight represent the positions where the scattering and decay-in-flight occur. Therefore, one will expect that the path length will disagree with a normal stopped kaon in the target. A likelihood is constructed by these three quantities to separate the stopped kaons from the other beam particles. The likelihood values for stopped kaons and scattered pions are shown in Figure 26. This cut requires that events should have the likelihood value greater than 2. It also requires that a stopped kaon should have an energy greater than 25 MeV and the number of kaon fibers greater than 2.

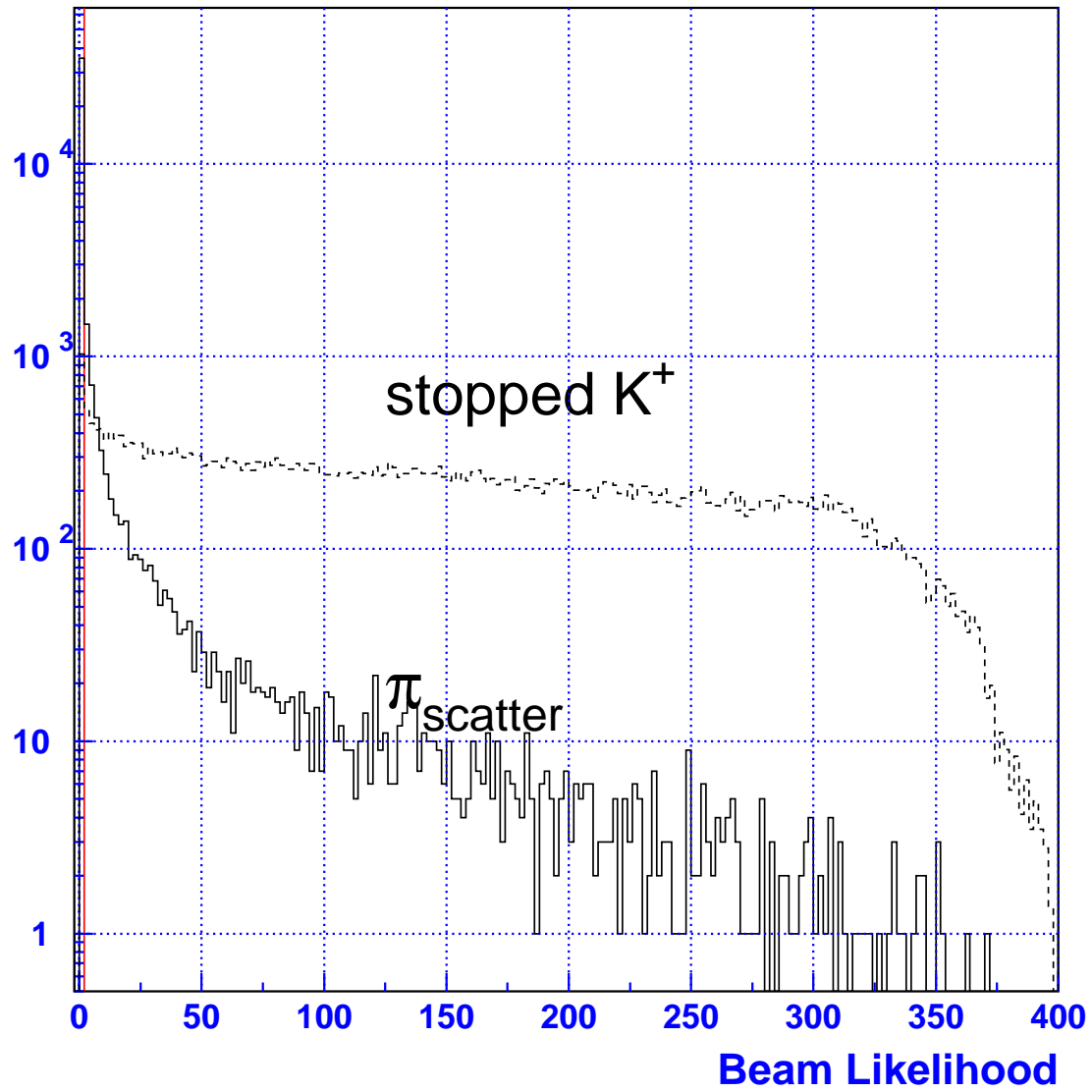


Figure 26: Beam likelihood for stopped kaons (dashed) and scattered pions (solid). The vertical line shows the cut position. It is required that the beam likelihood value is greater than 2. The stopped kaon and scattered pion events were derived from the $K_{\mu 2}$ monitor trigger data and the $\pi\nu\bar{\nu}(1)$ trigger data, respectively.

5.4 Kinematic reconstruction

Since the signal is defined inside the region between the $K_{\pi 2}$ and $K_{\mu 2}$ kinematic peaks in this analysis, it is very important to provide a correct measurement of the charged track kinematics and a powerful particle identification. The $K^+ \rightarrow \pi^+ \nu \bar{\nu}$ signal is selected by the following requirements:

Phase Space Cuts

The Phase Space Cuts require that the momentum, kinetic energy and range should be in the following regions:

$$\begin{aligned} \text{Momentum} & : 211 \leq P \leq 229 \text{ MeV}/c, \\ \text{Energy} & : 115 \leq E \leq 135 \text{ MeV}, \\ \text{Range} & : 33 \leq R \leq 40 \text{ cm}. \end{aligned}$$

As shown in Figure 19, the upper edges of the signal region are apart from the $K_{\mu 2}$ peaks. However, the lower edges are on the tails of the $K_{\pi 2}$ kinematics distributions. Since a systematic shift on either momentum or energy or range of charged track can lead to the $K_{\mu 2}$ background migrating into the signal box, the above kinematic variables are first checked. It is observed that the resolutions of these kinematic variables are somewhat dependent on the polar angle of the charged track. The measurement suffers a worse resolution effect when a charged track has a smaller polar angle. To reduce this impact on the background level in the signal box, the Phase Space cuts are tightened according to the following conditions:

$$\begin{aligned} P_{dev} & \equiv \frac{P_{meas} - P_{peak}}{\sigma_P} \geq 2.5, \\ E_{dev} & \equiv \frac{E_{meas} - E_{peak}}{\sigma_E} \geq 2.5, \\ R_{dev} & \equiv \frac{R_{meas} - R_{peak}}{\sigma_R} \geq 2.75, \end{aligned}$$

where P_{meas} , E_{meas} , R_{meas} are the measured values of momentum, energy and range; P_{peak} , E_{peak} , and R_{peak} are the $K_{\pi 2}$ kinematic peak positions as functions of the polar and azimuthal angles; and σ_P , σ_E , and σ_R are their resolutions as a function of the polar angle. Because of these tightened cut conditions, the background contamination does not depend on the polar and azimuthal angles.

dE/dx Cuts in the Range Stack

A main purpose of the cuts is to remove events with energy deposits in the RS track counters that are not consistent with those of a π^+ track. There is a case that charged particles inelastically (or elastically) scatter in the RS scintillators and lose energy of a few tens MeV in the scattering process. If a μ^+ from $K_{\mu 2}$ consumes its kinetic energy in the scattering process, the measured kinetic energy is underestimated, leading to a background event in the signal region. There is another case that a photon or an extra

track deposits energy in the track counters and the extra energy is counted by ADCs. If one photon from $K_{\pi 2}$ decay deposits the energy in some of the track counters and another photon is missed in the detection, the measured kinetic energy for the charged track will be overestimated, resultign in a possible contamination in the signal region. To remove these background, one must need the dE/dx Cuts in the Range Stack, which are composed of three cuts:

- Cut on Maximum Energy Deviation:
The energy deviation in each track counter is investigated.

$$\text{Energy deviation } (\chi_i) \equiv \frac{\log E_{exp}^i - \log E_{meas}^i}{\sigma^i}, \quad (23)$$

where E_{exp}^i and E_{meas}^i are the expected and measured energy deposits in the i th track counter, respectively, and σ^i is the sigma of $\log E_{meas}^i$. The expected energy deposit is calculated from the measured path length in the counter, assuming that the track is a pion. The logarithm is used for both the expected and measured energies to reduce the Landau tail effect. σ^i is calibrated with the Pion Scattering events in the $\pi_{scatter}$ monitor trigger, and the energy dependence on the σ 's is taken into account. The distributions of the maximum energy deviation for pion and muon tracks are shown in Figure 27. Events are rejected if the absolute value of the maximum deviation is greater than or equal to 4.

- Cut on the Confidence Level in RS Energy Measurements:
A confidence level is computed with the energy deviations in all of the track counters, except for the T-Counter, the stopping counter and the counter in which a sector crossing occurs. The confidence-level distributions for pion and muon tracks are shown in Figure 28. Events are rejected if the confidence level is less than 0.04. In the case that the maximum energy deviation is positive, the cut position on the confidence level is tightened from 0.04 to 0.2.
- Cut on Likelihood for RS Energy Measurements:
A likelihood is constructed with the energy differences $\Delta E \equiv \log E_{exp}^i - \log E_{meas}^i$ for layers up to the previous layer of the stopping layer. The distributions of the likelihood value for pion and muon tracks are shown in Figure 29. Events are rejected if the likelihood value, \mathcal{L}_{RS} , is not in the region $0 < \mathcal{L}_{RS} \leq 10$.

Range-Momentum Consistency Cut

This cut is used to check whether the range of the charged track is consistent with that for pions. A muon typically has a longer range than a pion for a given momentum. The range deviation in the Range Stack is defined as

$$\chi_{R-P} \equiv \frac{R_{meas} - R_{exp}}{\sigma_R}, \quad (24)$$

where R_{meas} is the measured range in the RS, R_{exp} is the expected range in the RS, which is calculated from the momentum measured by the UTC with an assumption that

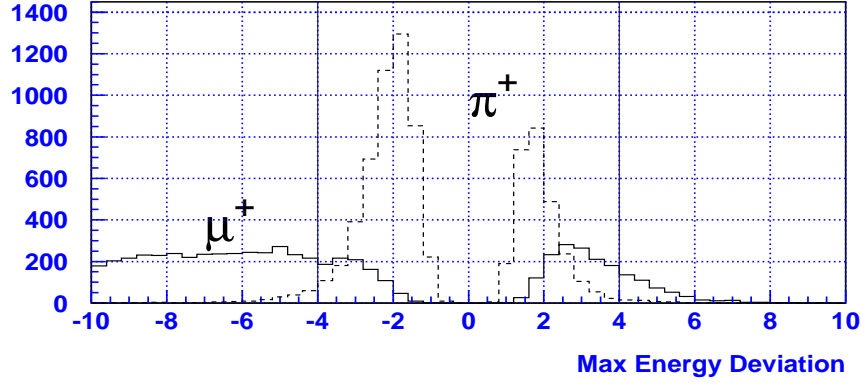


Figure 27: Distributions of the maximum energy deviation for pion (dashed) and muon (solid) tracks. The pion and muon events are derived from the $\pi\nu\bar{\nu}(1)$ trigger data. It is required that the maximum energy deviation is between -4 and 4 .

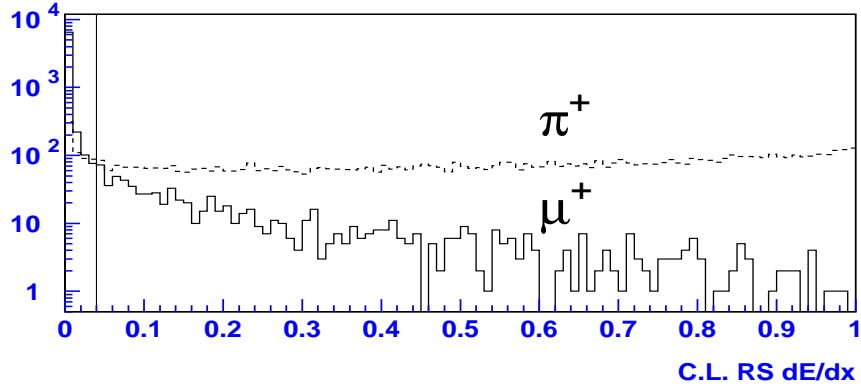


Figure 28: Distributions of the confidence level in the RS dE/dx measurement for pion (dashed) and muon (solid) tracks. The pion and muon events are derived from the $\pi\nu\bar{\nu}(1)$ trigger data. Events with a confidence level less than 0.04 are rejected.

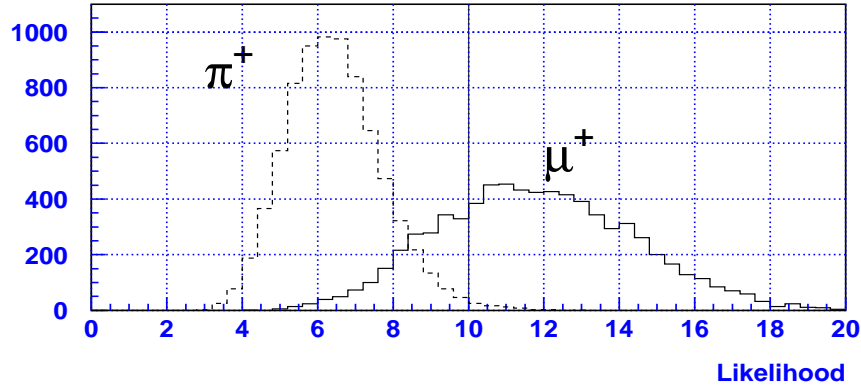


Figure 29: Distributions of the likelihood for the RS energy measurement for pion (dashed) and muon (solid) tracks. The pion and muon events are derived from the $\pi\nu\bar{\nu}(1)$ trigger data. It is required that the likelihood value \mathcal{L}_{RS} is $0 < \mathcal{L}_{RS} \leq 10$.

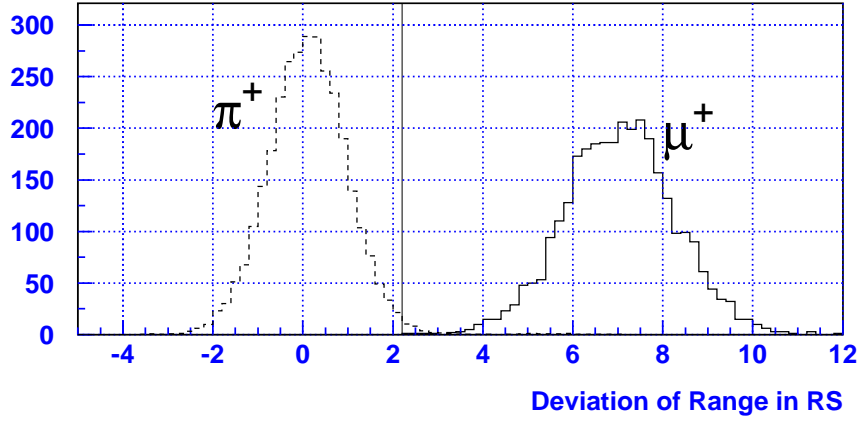


Figure 30: Distributions of the range deviation in the RS for pion (dashed) and muon (solid) tracks. The pion and muon events are derived from the $\pi\nu\bar{\nu}(1)$ trigger data. It is required that the range deviation is less than or equal to 2.2.

the track is a pion, and σ_R is the sigma of the measured range as a function of the momentum. The distributions of the range deviation for pions and muons are shown in Figure 30. Events are rejected if the range deviation is greater than 2.2.

5.5 Pion Identification

A powerful pion identification is from the search of a $\pi^+ \rightarrow \mu^+ \rightarrow e^+$ decay sequence in the stopping counter. As explained in Section 2.5, the signature for this decay sequence is as follows:

- Three pulses of the $\pi^+ \rightarrow \mu^+ \rightarrow e^+$ decay sequence are found in the stopping counter.
- The kinetic energy of the μ^+ from $\pi^+ \rightarrow \mu^+ \nu$ decay is 4.2 MeV. The actual energy measured by TDs is 3.04 MeV, due to a saturation effect in plastic scintillators [44]. The path length of the μ^+ with 4.2 MeV is about 1 mm, and the μ^+ should therefore be detected only in the stopping counter.
- The e^+ from $\mu^+ \rightarrow e^+ \bar{\nu}_e \nu_\mu$ decay has a kinetic energy of $0 < E < 53$ MeV. Most of the e^+ 's exit the stopping counter and deposit energy in the other RS counters.

For a charged pion, three pulses from the $\pi^+ \rightarrow \mu^+ \rightarrow e^+$ decay sequence should be observed by the TDs at both ends of the stopping counter. On the contrary, for the charged muon, only two pulses from the $\mu^+ \rightarrow e^+$ decay can be observed. A muon can fake a pion when an extra pulse is detected, in addition to the two pulses of $\mu^+ \rightarrow e^+$ decay. To eliminate the Muon background, two stages of suppressions are imposed.

In the first stage, $\pi^+ \rightarrow \mu^+$ double-pulse fitting is performed. The pulse development in the stopping counter is recorded, in a period of 2 μ s, by the 500 MHz Transient Digitizers based on flash ADCs (TDs). In the event reconstruction, the pulse shapes in the time range of 100 ns are fitted with both single-pulse and double-pulse assumptions (sometimes

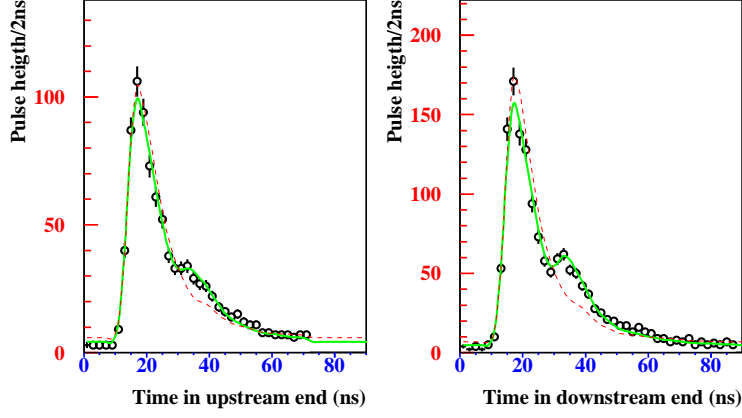


Figure 31: Double-pulse fitting of the TD pulse shapes in the stopping counter for a pion event. The upper and lower plots are the TD pulse shapes for the downstream and upstream ends, respectively. Data (open circles) from upstream end and downstream end of the stopping counter are fitted separately. The solid curve is for the double-pulse assumption with both pion and muon pulses presenting in the stopping counter, while the dash curve is for the single-pulse assumption with only a pion pulse.

a triple-pulse assumption if more than two pulses are found), as shown in Figure 31. The first two pulses of the $\pi^+ \rightarrow \mu^+$ decay can be observed by requiring that the double-pulse fitting qualities are better than those from the single-pulse fitting.

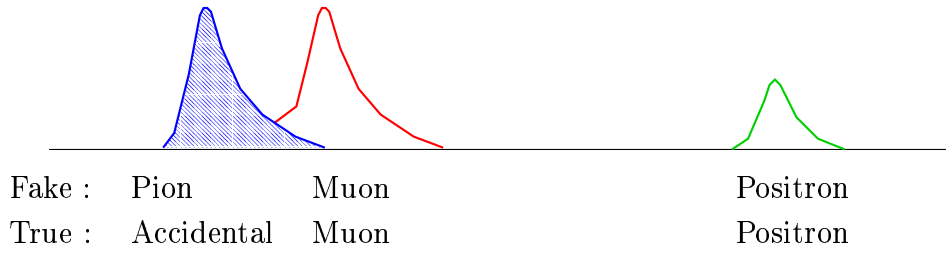
In the second stage, a further suppression is made to the muon events that pass the Double-Pulse Fitting Cut. There are four cases that a two-pulse $\mu^+ \rightarrow e^+$ decay can fake a three-pulse $\pi^+ \rightarrow \mu^+ \rightarrow e^+$ decay sequence.

- Pion time accidental: An accidental activity produces the first pulse, while the $\mu^+ \rightarrow e^+$ decay gives the second and third pulses in timing sequence (see the top figure in Figure 32).
- Early muon decay: The two-pulse $\mu^+ \rightarrow e^+$ decay occurs at an early time ($0 \sim 100$ ns), producing the first and second pulses, and an accidental activity makes the third pulse (see the upper middle figure in Figure 32).
- Muon time accidental: The two-pulse $\mu^+ \rightarrow e^+$ decay makes the first and third pulses, while an accidental activity occurs in between (see the lower middle figure in Figure 32).
- Tail fluctuation: The muon makes the first pulse, and a tail fluctuation of the first pulse recorded in TD is identified as the second pulse. The decay positron from the muon decay makes the third pulse (see the bottom figure in Figure 32).

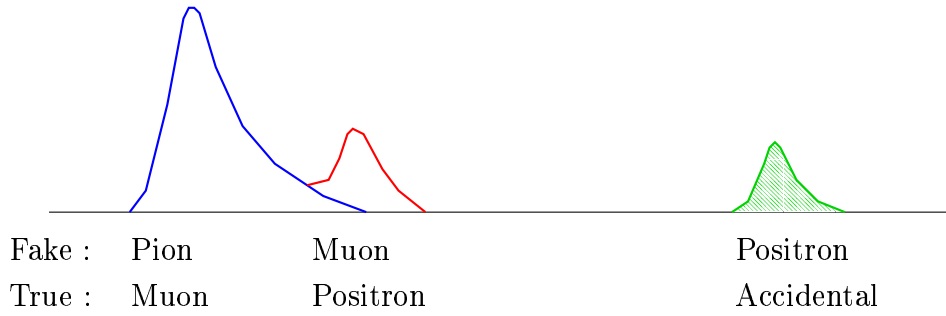
Five cuts are prepared to remove these fake $\pi^+ \rightarrow \mu^+ \rightarrow e^+$ backgrounds (see Table 4).

π^+ Time Consistency Cut

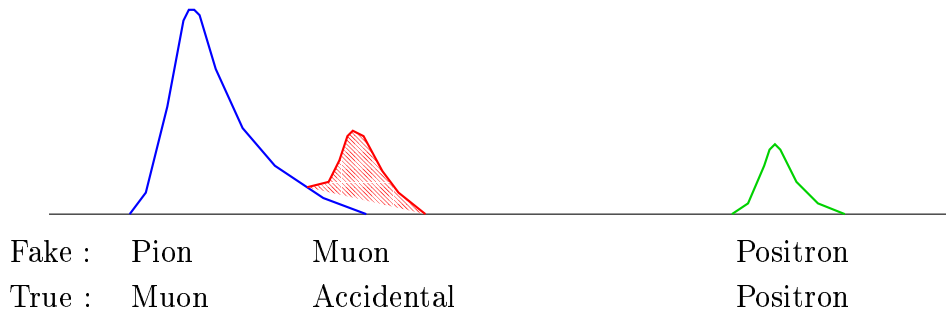
- Pion time accidental



- Early muon decay



- Muon time accidental



- Tail fluctuation

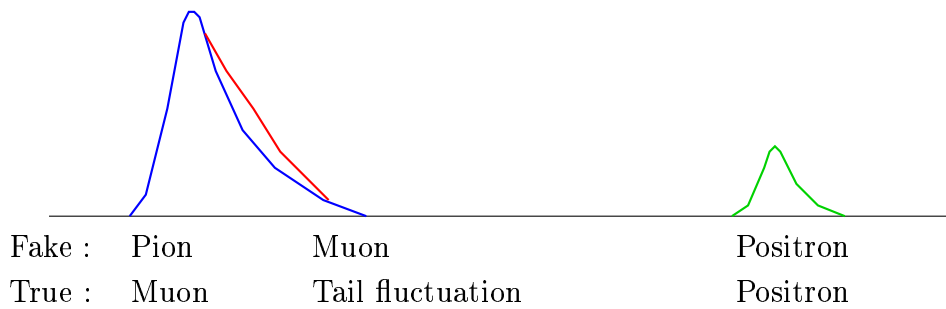


Figure 32: Cases where the two-pulse $\mu^+ \rightarrow e^+$ decay fakes the three-pulse $\pi^+ \rightarrow \mu^+ \rightarrow e^+$ decay sequence.

Cut	Pion time accidental	Early muon decay	Muon time accidental	Tail Fluctuation
π^+ Time Consistency Cut	✓			
$\mu^+ \rightarrow e^+$ Decay Requirement		✓		
Cut on Muon Time Accidental			✓	
Cut on Muon Time Accidental in the Track Counters			✓	
Neural Net $\pi^+ \rightarrow \mu^+$ Decay Cut			✓	✓

Table 4: List of the $\pi^+ \rightarrow \mu^+ \rightarrow e^+$ Decay Sequence Cuts and the targeting backgrounds.

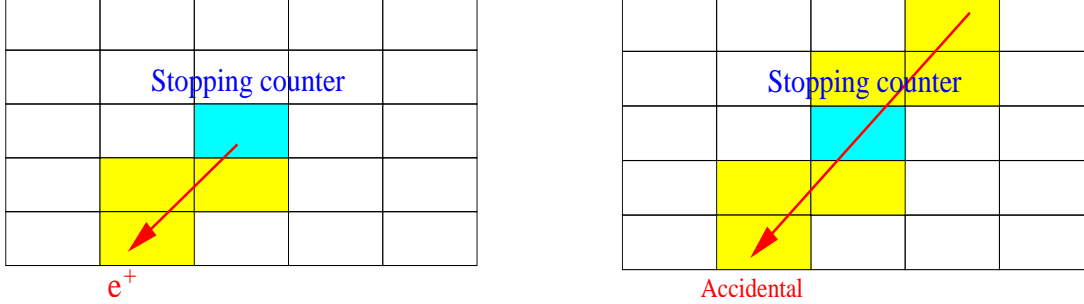


Figure 33: Schematic downstream views of signals (left) and backgrounds (right) of the $\mu^+ \rightarrow e^+$ decay. Each rectangle shows an RS scintillator. The counter in the center shows the stopping counter and the counters on the arrow show the hit counters.

This cut targets the pion time accidental background. When an accidental activity makes the first pulse and a charged track makes the second pulse in the stopping counter, the timing of the first pulse obtained by the TD (referred to as TD pion time) is not coincident with the track time. Events are rejected if the TD pion time ($t_{\pi,TD}$) and the track time (t_{RS}) do not satisfy

$$|t_{\pi,TD} - t_{RS}| \leq 2.5 \text{ ns.} \quad (25)$$

$\mu^+ \rightarrow e^+$ Decay Requirement

This cut requires that the third pulse in the stopping counter should be due to the positron originating from the $\mu^+ \rightarrow e^+$ decay. The positron from the $\mu^+ \rightarrow e^+$ decay is emitted from the stopping counter, and it deposits energy in other counters (see left figure in Figure 33). The positron finding starts from examining the RS hit counters (referred to as a cluster) in the region ± 1 sectors and ± 2 layers of the stopping counter. The cluster is required to be adjacent to the stopping counter and to have hits in the same sector as the stopping counter. Candidates for the positron are found by requiring that the average time of the hits in the cluster is coincident (within ± 2.4 ns) with the time of the third pulse in the stopping counter and the z positions of the hits in the cluster, obtained from the end-to-end time differences of the hits, are consistent with that of the third pulse in the stopping counter. In the case that an accidental track that passes through the stopping counter makes a third pulse, the track deposits energy in the counters on both sides of the stopping counter (see right figure in Figure 33). The positron from the stopping counter can be determined by distinguishing between one-side and both-side tracks. The early muon decay background is removed by requiring that the third pulse, not the second pulse, is due to the positron from the $\mu^+ \rightarrow e^+$ decay.

Cut on Muon Time Accidental

This cut targets the muon time accidental background. It is possible that the accidental activities with energy deposit in the stopping counter can also make hits in other RS counters around the stopping counter. Any accidental activities coincident with the muon time are searched for in the neighboring RS counters of the stopping counter and the counters in BV, BVL and EC. The time windows and energy thresholds for the various subsystems in RS, BV, BVL and EC are optimized in order to have the highest rejection power at a given acceptance value of 94%. Events are rejected if the energy sum of the hits within a time window in any subsystem is greater than the threshold.

Cut on Muon Time Accidental in the Track Counters

This cut rejects the muon time accidental background by performing double-pulse fitting in the two RS track counters prior to the stopping counter. The purpose of the double-pulse fitting in the track counter is to eliminate the accidental activities that overlap the charged track, and make a second pulse in the stopping counter. Events are rejected if the qualities of fits with a double-pulse assumption are better than those with the single-pulse assumption, and if the time of the fitted second pulse is coincident (within ± 5 ns) with the muon time in the stopping counter, the events are rejected.

Neural Net $\pi^+ \rightarrow \mu^+$ Decay Cut

This cut targets the tail fluctuation background. Tail fluctuations can be observed when there is a discrepancy between the measured pulse shape and the template pulse shape calibrated by using the pion pulses. The qualities of fits to the fluctuated pulses are worse than those to the well-separated first and second pulses. Tail fluctuations of pulses originate from noises in the transportation of signals from PMTs to TDs. The pulse fluctuations at both ends should not be correlated. The pulse area and time of the fitted second pulse tend to be small in the fluctuated pulse. The separations between pion (which have clear double pulses) and muon (which have fluctuated pulse) tracks are good in the distributions of the following variables:

- Energy of the second pulse (E_μ).
- Time of the second pulse (T_μ).
- Log of the product of the χ^2 ratios of single- to double-pulse fits for both ends ($\log_{10}(R(1) \cdot R(2))$ where $R(i)$ is the χ^2 ratio for end i ²).
- Log of the product of the single-pulse fit χ^2 's for both ends ($\log_{10}(\chi_1^2(1) \cdot \chi_1^2(2))$ where $\chi_1^2(i)$ is the single-pulse fit χ^2 for end i).
- Difference between the z positions of the first (z_π) and second (z_μ) pulses obtained by the energy ratio of both ends ($z_\pi - z_\mu$).
- Time difference between both ends (dt).

²End 1 and 2 mean upstream and downstream ends, respectively.

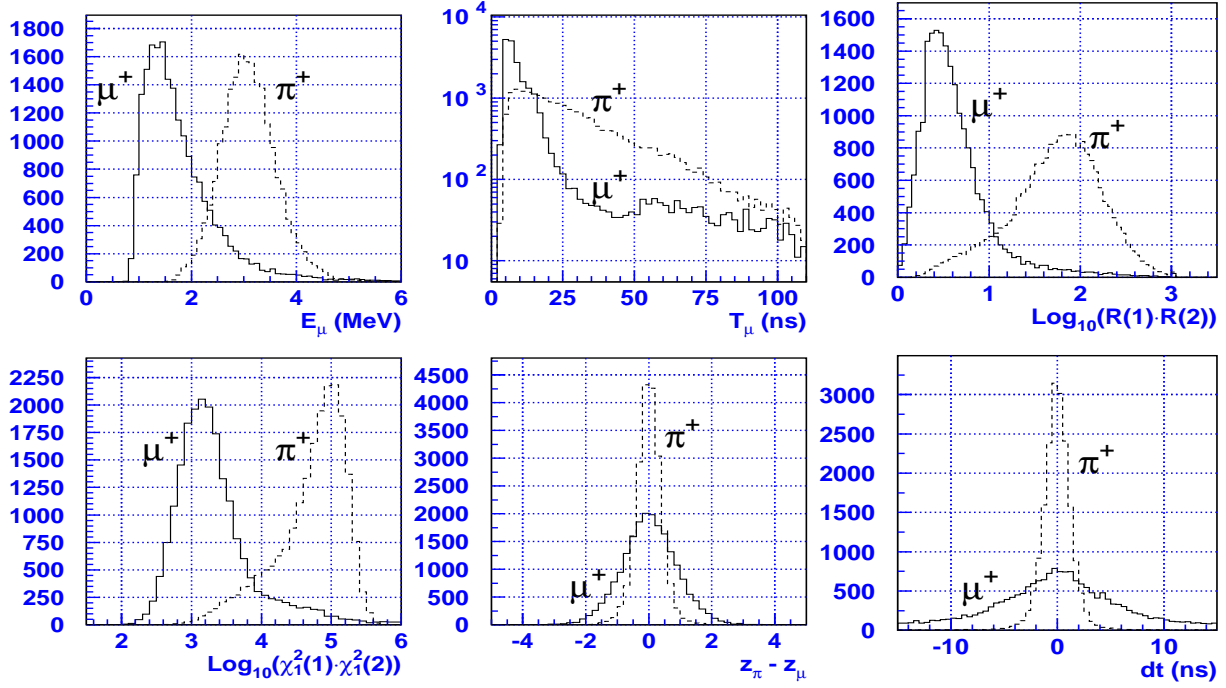


Figure 34: Distributions of the input variables for the Neural Net function in pion (dashed) and muon (solid) events. The energy of the second pulse (top left), time of the second pulse (top middle), log of the product of the χ^2 ratios of single- to double-pulse fits for both ends (top right), log of the product of the single-pulse fit χ^2 's for both ends (bottom left), z position difference between the first and second pulses obtained from the energy ratio of both ends (bottom middle), and time difference of the second pulses in both ends (bottom right).

The distributions of the variables for pions and muons are shown in Figure 34. Applying a fixed cut to each variable causes a non-negligible acceptance loss. In order to achieve a higher acceptance at the same rejection as the fixed cuts, a Neural Network (NN) technique is adopted.

NN functions are derived via a Multi-Layer Perception (MLP) program incorporated in the library of Physics Analysis Workstation (PAW) [45]. The NN functions give their output from several input variables (sometimes referred to as neuron). The NN functions peak their output values for a signal sample around 1 and those for a background sample around 0. In order to achieve a good separation between signal and background events, the MLP program performs a number of trials for training the NN functions. Half of the sample is used for training the NN functions, and the other half is used for confirming that the trained function has the same performance on both samples.

To create a NN function, the Pion Scattering and $K_{\mu 2}$ Range Tail events in the $\pi\nu\bar{\nu}(1)$ trigger, which pass all other $\pi^+ \rightarrow \mu^+ \rightarrow e^+$ Decay Sequence Cuts, are used as signal and background samples, respectively. The tail fluctuation background is enhanced in the background sample by imposing all the other $\pi^+ \rightarrow \mu^+ \rightarrow e^+$ Decay Sequence Cuts and removing the other backgrounds. A 5-variable NN function is obtained using the above six variables as neurons. The z position and time differences are combined to create a χ^2

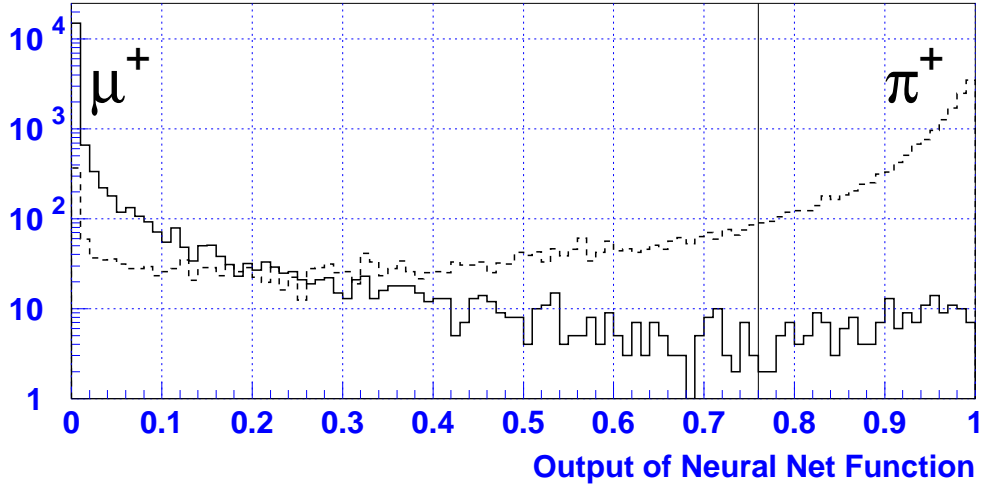


Figure 35: Distributions of the outputs of the NN function for pion (dashed) and muon (solid) events. Events with an output of the NN function less than 0.76 are rejected.

as a neuron,

$$\chi^2 \equiv \left(\frac{dz}{\sigma_{dz}} \right)^2 + \left(\frac{dt}{\sigma_{dt}} \right)^2, \quad (26)$$

where $dz \equiv z_\pi - z_\mu$ and σ_{dz} (σ_{dt}) is the sigma of the dz (dt) distribution. The distributions of the outputs of the NN function for pions and muons are shown in Figure 35. Using the pions' and muons' distributions, the rejection of this cut as a function of the acceptance is obtained by changing the cut position (see Figure 36). The cut position at 0.76 in the output of the NN function is determined so that the acceptance of this cut is 85%.

5.6 Photon veto

The signature of $K^+ \rightarrow \pi^+ \nu \bar{\nu}$ is a single π^+ track, and no other particle is observed in the detector. Any activities that originate from a K^+ decay must be detected in the subsystems of the detector. The main backgrounds, including photon activities, are the $K_{\pi 2}$ and $K_{\mu \nu \gamma}$ decays. The energy of photons from $\pi^0 \rightarrow \gamma \gamma$ in $K_{\pi 2}$ decays is $20.2 < E_\gamma < 225.3$ MeV in the rest frame of K^+ . On the contrary, the energy of a photon from $K_{\mu \nu \gamma}$ decays is in the range $0 < E_\gamma < 236$ MeV, in which the photons are mostly below with low energy (50 MeV) are dominant [46]. The detection of a few MeV photons is necessary to eliminate backgrounds related to photons.

The total rejection against backgrounds associated with photons is required to be in an order of 10^6 , including those from both online and offline. A rejection of 10^4 is already achieved by the online photon veto, leaving a further 10^2 rejection to be achieved by the offline analysis.

Searches for the photons coincident with the track time are performed in the subsystems of the Barrel Veto (BV), the Barrel Veto Liner (BVL), the Range Stack (RS), the End Caps (EC), the target, the I-Counter (IC), the V-Counter (VC), the Collar (CO) and the Microcollar (MC). Different time windows and energy thresholds are set to the individual subsystems. For the BV, BVL and RS, whose scintillator signals are read out

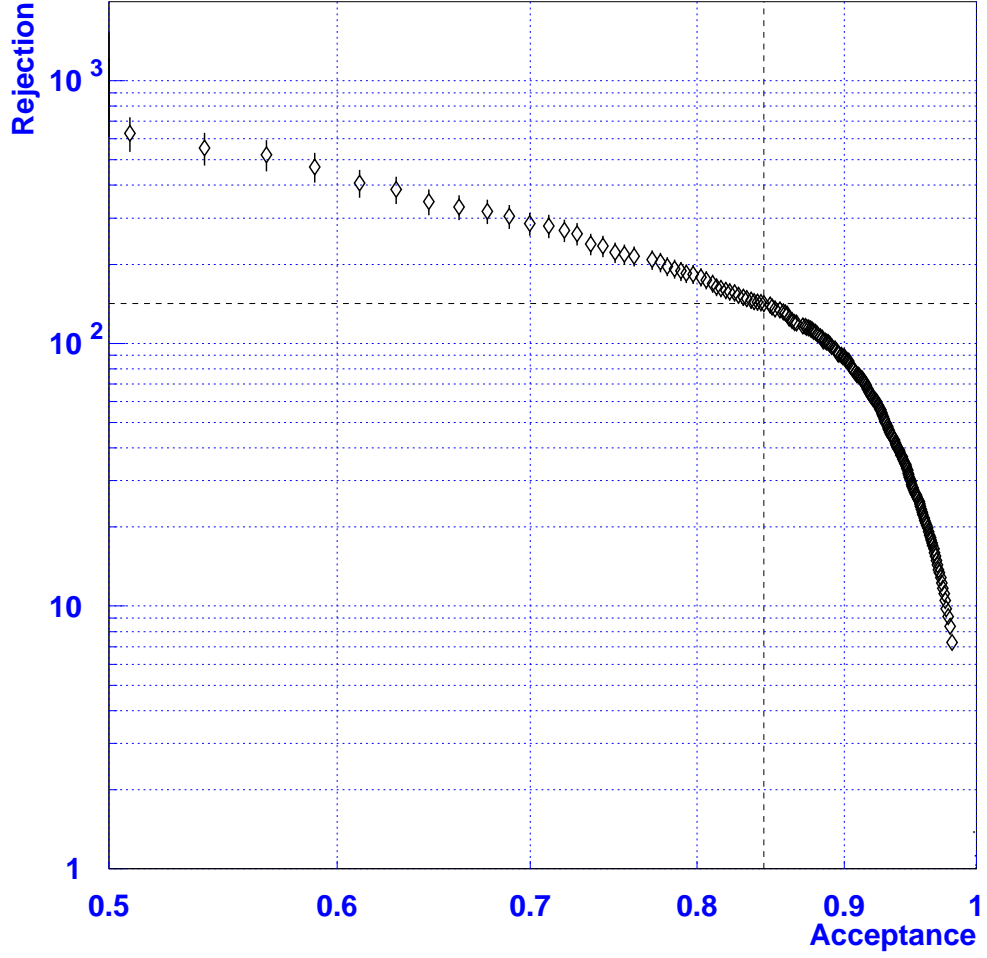


Figure 36: Rejection of the Neural Net $\pi^+ \rightarrow \mu^+$ Decay Cut as a function of the acceptance. The cross point of the vertical and horizontal lines shows the rejection and acceptance at the cut position.

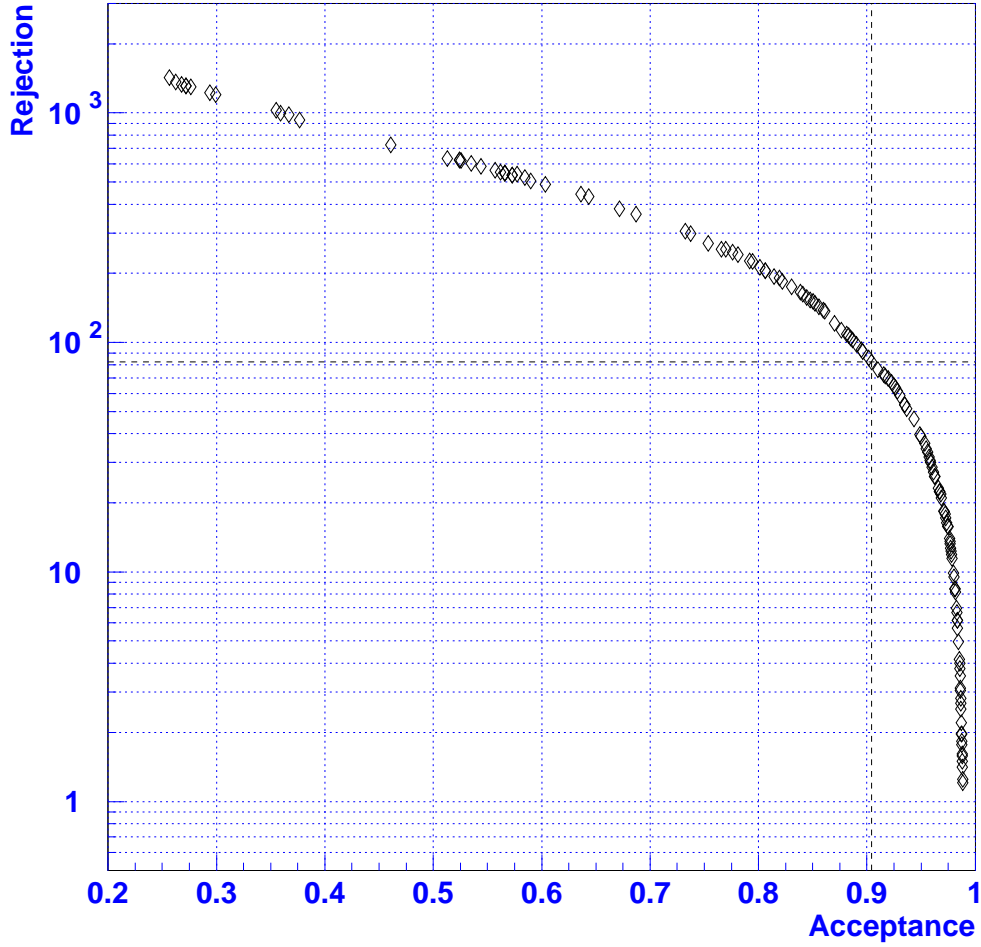


Figure 37: Rejection of the Photon Veto Cuts against the $K_{\pi 2}$ background as a function of the acceptance. The cross point of the vertical and horizontal lines shows the rejection and acceptance at the cut position.

by both-end PMTs, energies and times of photon hits are basically obtained from the geometrical mean and the average time of both ends, respectively. In the case that the energies or times are missed in a single end of the ADCs or TDCs, these single-end hits are categorized separately and different time windows and energy thresholds are applied because the precisions of the time and energy measurements of the single-end hits are worse than those of the both-end hits.

The time window and energy threshold in each category are optimized by changing their cut positions to achieve better acceptance and rejection. Figure 37 shows the rejection of the Photon Veto Cuts against the $K_{\pi 2}$ background as a function of acceptance. The cut position for each category is determined so that the $K_{\pi 2}$ background is reasonably suppressed in the background estimation. An acceptance of 90.5% and a rejection of 84.3 are achieved using this set of cut positions.

6 Signal box and background Estimation

In this section, estimations of the background levels in the Signal Region are described. The backgrounds for $K^+ \rightarrow \pi^+ \nu \bar{\nu}$ are categorized into three groups:

- $K_{\pi 2}$ background,
- Muon background ($K_{\mu 2}$ Range Tail and Muon Band backgrounds), and
- Beam background (Single Beam, Double Beam, and Charge Exchange (CEX) backgrounds).

All of the backgrounds, except for the CEX background, are estimated with real data via a technique of the Bifurcation Method. Estimations of the $K_{\pi 2}$ and Beam backgrounds are performed with a uniformly-sampled 2/3 portion of the $\pi \nu \bar{\nu}(1)$ trigger data (referred to as a 2/3 sample). The background estimation with a 2/3 sample is expected to have less bias than that with a 1/3 sample, which is used for designing the cuts. After it is confirmed that the estimations obtained from 2/3 and full samples are consistent. An estimation of the muon background is performed with the full $\pi \nu \bar{\nu}(1)$ trigger data, because larger statistics are needed for the estimations.

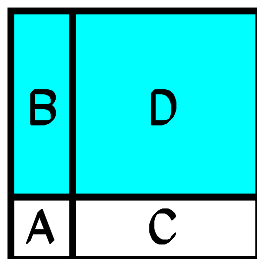
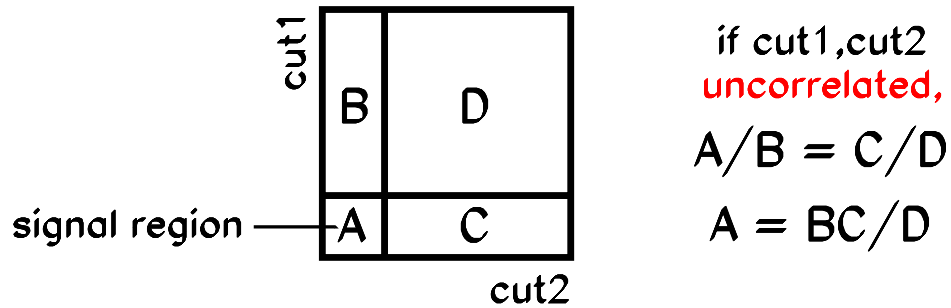
6.1 Method of Background Estimation

In this analysis, the number of expected signal events is small. Background levels in the Signal Region have to be smaller than the expected signal events. Background measurements based on small samples have large statistical uncertainties. Estimations of background levels by the Bifurcation Method help to enhance the statistics and to make reliable measurements of background levels having less than one event. The estimation is performed with two uncorrelated cuts or groups of cuts, which are independently inverted to enhance the statistics. In other words, background samples are created by selecting events that fail at least one of the selection criteria used in this analysis.

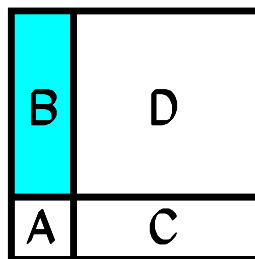
A pictorial explanation for the Bifurcation Method is shown in Figure 38. First of all, a sample targeting one specific background source is selected by removing the other background sources. The number of events remaining after applying the setup cuts is $A + B + C + D$ events. Each figure in Figure 38 shows the parameter space of two cuts, namely "cut1" and "cut2". The number of background events in the Signal Region (i.e., region "A") is A events. If the two cuts are uncorrelated, that is, if the rejection of a cut does not depend on the rejection of the other cut, the ratio of the number of background events in region "A" to region "B" must be equal to the ratio in region "C" to region "D", i.e., $A/B = C/D$. Background events in the Signal Region are therefore obtained from the relation $A = BC/D$. This is how background levels in the Signal Region are estimated using events outside the Signal Region.

The way to proceed with the Bifurcation Method is as follows:

- A specific background sample is prepared by inverting "cut1" ($B + D$ events remain); "cut2" is applied to the sample and B events remain (see the second row in Figure 38). This stream is called a "Normalization Branch".



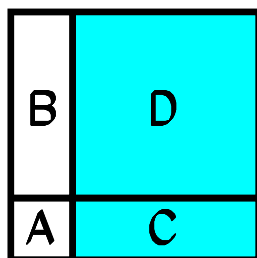
invert cut1
B+D events



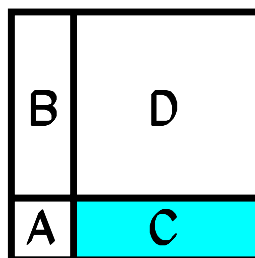
apply cut2
B events

$$N = B$$

← Normalization branch



invert cut2
C+D events



apply cut1
 $R = (C+D)/C$

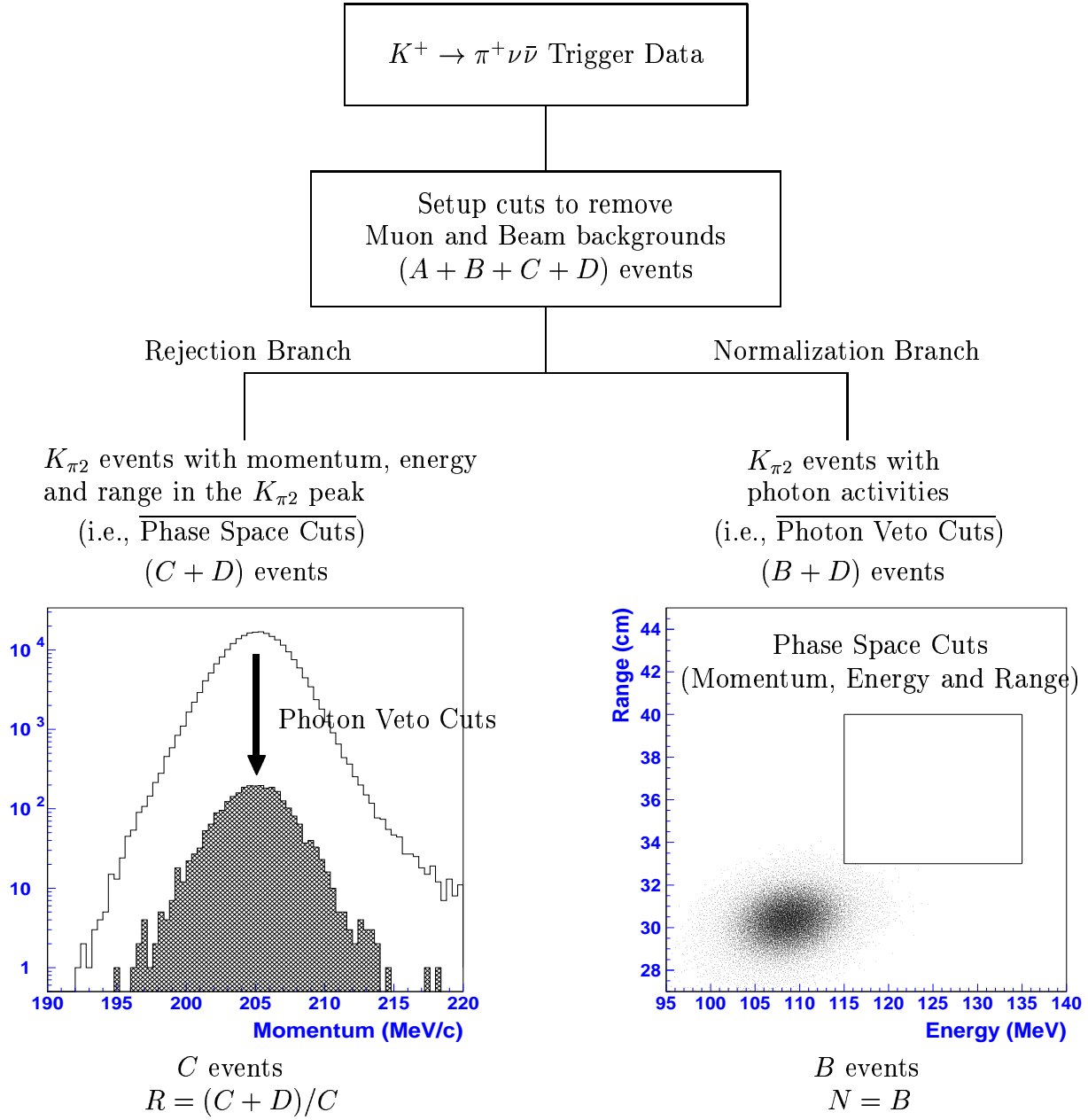
$$bg = N/(R-1) = BC/D$$

← Rejection branch

Figure 38: Pictorial explanation of the Bifurcation Method.

- On the other hand, another background sample is also prepared by inverting "cut2" ($C + D$ events remain). By imposing "cut1", the ratio D/C is obtained (see the third row in Figure 38). The rejection factor of this "cut1", R , is calculated from the ratio $(C + D)/C$. This stream is called a "Rejection Branch".
- The number of background events in the Signal Region is estimated by the number of events remaining in the Normalization Branch, $N (= B)$, divided by the rejection factor, $R - 1 (= D/C)$, i.e., $N_{Bkg} = N/(R - 1)$.

As an example, a brief explanation for the $K_{\pi 2}$ background estimation via the Bifurcation Method is presented in Figure 39. The $K_{\pi 2}$ background sample in the $K^+ \rightarrow \pi^+ \nu \bar{\nu}$ trigger data is selected by removing the Muon and Beam backgrounds (corresponding to the first row in Figure 38). In the Normalization Branch, $K_{\pi 2}$ events are selected by requiring photon activities (i.e., the Photon Veto Cuts ("cut1") are inverted). The Phase Space Cuts (i.e., cuts on momentum, energy and range, "cut2") are applied to the $K_{\pi 2}$ sample and N events remain in the Normalization Branch (corresponding to the second row in Figure 38). In the Rejection Branch, $K_{\pi 2}$ events with momentum, energy and range in the $K_{\pi 2}$ peak are selected (i.e., the Phase Space Cuts, "cut2", are inverted). the Photon Veto Cuts ("cut1") are applied to the $K_{\pi 2}$ events in the kinematic peak (corresponding to the third row in Figure 38) and the rejection factor of the Photon Veto Cuts, $R - 1$, is measured. Finally, the $K_{\pi 2}$ background level is estimated based on the number of remaining events in the Normalization Branch (N) and the rejection factor ($R - 1$).



$$\text{Background Level (A events)} = BC/D = N/(R - 1)$$

Figure 39: Example of the Bifurcation Method.

6.2 Determination of Signal Region

In cut developments using uniformly sampled 1/3 data in the $\pi\nu\bar{\nu}(1)$ trigger, all of the cut positions have been determined. Although the signal region should basically be a region inside the cut positions of all the selection criteria, the definition of the signal region is modified, before looking into the potential signal regions, in order to enlarge the signal acceptance. The modification is motivated as follows:

- The distributions of both signals and backgrounds in the cut space are understood well by the functions.
- The background levels can also be controlled well in the enlarged signal regions.
- In the likelihood ratio technique, the signal-to-background ratios of the cells that contain candidate events, not the total background level in the whole signal region, contribute to the branching-ratio measurement.

The cuts to be loosened are those related to the $K_{\pi 2}$ kinematic, Photon Veto and $\pi^+ \rightarrow \mu^+ \rightarrow e^+$ functions. The cuts for the Muon and Beam backgrounds are not loosened, because the cut positions for the $K_{\mu 2}$ Range Tail and Muon Band backgrounds are at the knee in the background level v.s. acceptance curve; loosening them does not provide much acceptance gain. Loosening the cut positions of the $K_{\pi 2}$ kinematic, Photon Veto and $\pi^+ \rightarrow \mu^+ \rightarrow e^+$ functions provides a relatively large acceptance gain. However, loosening three cuts simultaneously increases the background levels. The signal region is the combination of the following three cases:

- the cuts for the $K_{\pi 2}$ kinematics are loosened,
- the Photon Veto Cuts are loosened,
- the $\pi^+ \rightarrow \mu^+ \rightarrow e^+$ Decay Sequence Cuts are loosened.

When one of the three is loosened, the cut positions of the other two are kept unchanged. The schematic figure of the signal region in 3-dimensional space is shown in Figure 40. The revised (enlarged) signal region consists of the standard signal region, which is created without loosening any cuts, plus three extensions. Hereafter, the revised and standard signal regions are referred to as the Signal Region and the 1×1 Region, respectively. The regions created by loosening the Photon Veto Cuts, $\pi^+ \rightarrow \mu^+ \rightarrow e^+$ Decay Sequence Cuts and $K_{\pi 2}$ kinematic cuts are referred to as PV Extended, $\pi^+ \rightarrow \mu^+ \rightarrow e^+$ Extended and $K_{\pi 2}$ Kinematics Extended Regions, respectively. All of which include the 1×1 Region. The loosening factors for the cuts ($f_{\pi\mu e}$, $f_{K\pi 2}$ and f_{PV}) are developed so that the background levels after loosening them are acceptable. The loosening factors and acceptance gains are summarized in Table 5. The loosening factors for these three cuts are $f_{\pi\mu e} = 4.2$, $f_{K\pi 2} = 9.5$ and $f_{PV} = 4.0$, which means 4.2-times more background related to the $\pi^+ \rightarrow \mu^+ \rightarrow e^+$ identification, 9.5-times more $K_{\pi 2}$ background and 4.0-times more background related to Photon Veto. The total acceptance gain by enlarging the signal region is 31%, which is the sum of the individual acceptance gains (12% from $K_{\pi 2}$, 12% from $\pi^+ \rightarrow \mu^+ \rightarrow e^+$ identification, and 7% from Photon Veto).

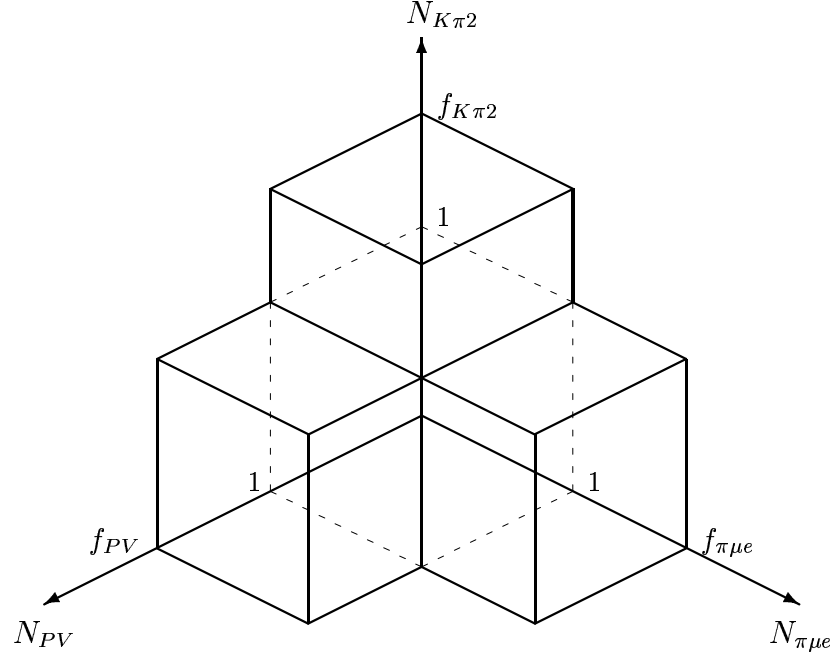


Figure 40: Schematic figure of the Signal Region in the 3-dimensional parameter space of the $\pi^+ \rightarrow \mu^+ \rightarrow e^+$, $K_{\pi 2}$ kinematic and Photon Veto functions (in the unit of relative background level).

Cuts	Loosening factor	Acceptance gain
$\pi^+ \rightarrow \mu^+ \rightarrow e^+$	4.2	$\times 1.12$
$K_{\pi 2}$ kinematic	9.5	$\times 1.12$
Photon Veto	4.0	$\times 1.07$
Total acceptance gain		$\times 1.31$

Table 5: Loosening factors for the $\pi^+ \rightarrow \mu^+ \rightarrow e^+$ Decay Sequence Cuts, the $K_{\pi 2}$ Kinematic Cuts and the Photon Veto Cuts (second column) with their acceptance gains (third column).

6.3 $K_{\pi 2}$ Background Estimation

The $K_{\pi 2}$ decay has a charged track with monochromatic momentum, range and energy, and has two photons at the track time. Two cuts for the Bifurcation are therefore the Phase Space Cuts to the π^+ track and the Photon Veto Cuts.

The $K_{\pi 2}$ background level is estimated in the following way. Setup cuts are applied to the $\pi\nu\bar{\nu}(1)$ trigger sample in order to remove other backgrounds, and to select events with well-reconstructed π^+ tracks. In the Rejection Branch, $K_{\pi 2}$ events with the momentum, energy, and range in the $K_{\pi 2}$ peak are selected (i.e., inverse of the Phase Space Cuts). Photon Veto Cuts are imposed on this $K_{\pi 2}$ -rich sample. The Photon Veto rejection is measured to be

$$R_{PV} = \frac{481362}{5710} = 84.3 \pm 1.2(stat.). \quad (27)$$

In the Normalization Branch, $K_{\pi 2}$ events are selected by requiring photon activities (i.e., inverse of the Photon Veto Cuts). The Phase Space Cuts ($P_{dev} \geq 2.5$, $E_{dev} \geq 2.5$ and $R_{dev} \geq 2.75$) are imposed on this sample to count the number of the $K_{\pi 2}$ events remaining in the Normalization Branch. The suppression of the Phase Space Cuts is so large; the statistics of the events remaining in the Normalization Branch are very small. In order to perform a more precise estimation, a so-called Second Bifurcation Method is performed.

Second Bifurcation means the Normalization Branch is further bifurcated. The Phase Space Cut for Energy ($E_{dev} \geq 2.5$) and the Cuts for Range and Momentum ($R_{dev} \geq 2.75$ and $P_{dev} \geq 2.5$) are separated as two independent cuts. The expected number of events in the Normalization Branch (N_{NB}) can be estimated by $N_{NB} = N_{RP}/(R_E - 1)$, where N_{RP} is the number of events that remain after the Phase Space Cuts for Range and Momentum are imposed, and R_E is the rejection of the Phase Space Cut for Energy.

The estimation by the Second Bifurcation Method results in 1.04 ± 0.20 events of the $K_{\pi 2}$ background (inside the 1×1 Region) in the Normalization Branch. The estimations for the PV Extended, $\pi^+ \rightarrow \mu^+ \rightarrow e^+$ Extended and $K_{\pi 2}$ Kinematics Extended Regions are performed in the same way as the 1×1 Region, except that the corresponding cuts are loosened. The expected numbers of events in the Normalization Branch are summarized in Table 6.

Region	N_{NB} (events)
1×1	1.04 ± 0.20
PV Extended	0.97 ± 0.24
$\pi^+ \rightarrow \mu^+ \rightarrow e^+$ Extended	1.15 ± 0.20
$K_{\pi 2}$ Kinematics Extended	9.01 ± 1.00

Table 6: Expected numbers of events remaining in the Normalization Branch. The errors are statistical.

The background level in the Signal Region is evaluated by the sum of the background levels in the individual Extended Regions. Since each Extended Region contains the 1×1 Region, the background levels that are over-counted should be subtracted (see Figure 41). The $K_{\pi 2}$ background level in the Signal Region is therefore obtained in the following way:

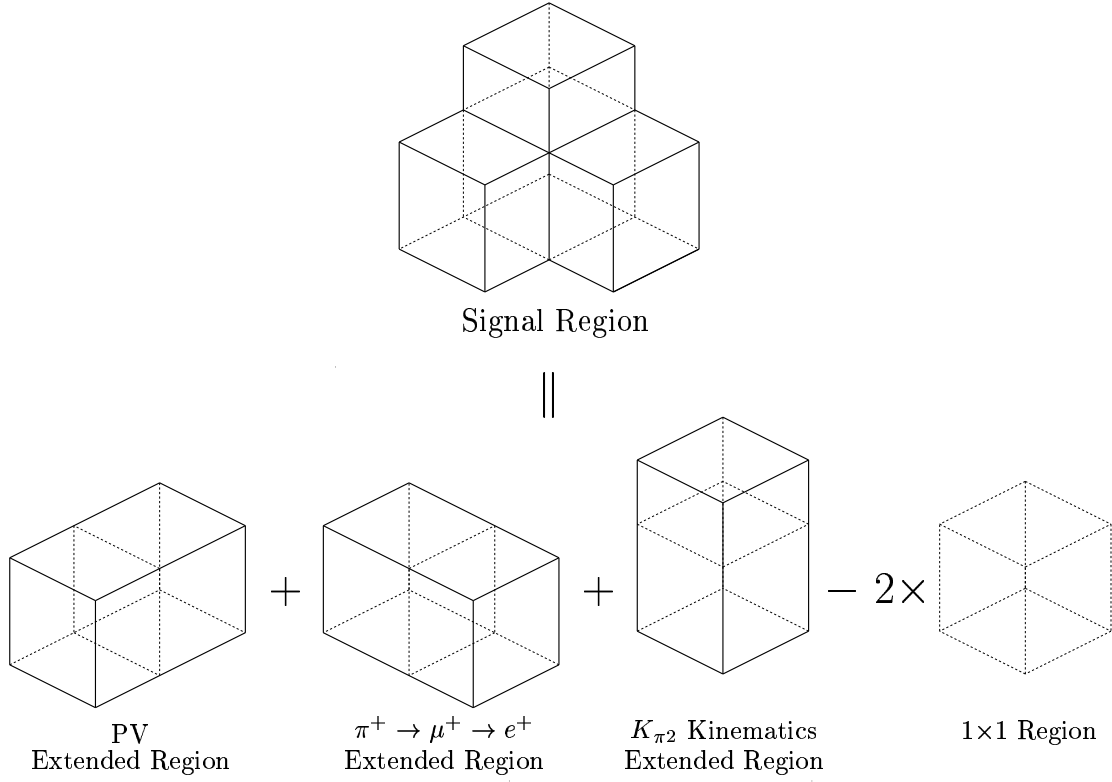


Figure 41: Method of the background level calculation in the Signal Region.

$$N_{K_{\pi 2}} = 1.5 \times \left[\frac{N_{NB}(PV)}{R'_{PV} - 1} + \frac{N_{NB}(\pi\mu e)}{R_{PV} - 1} + \frac{N_{NB}(K_{\pi 2})}{R_{PV} - 1} - 2 \frac{N_{NB}(1 \times 1)}{R_{PV} - 1} \right], \quad (28)$$

where R'_{PV} represents the Photon Veto rejection at the loose cut position and is by a factor of 4 smaller than the standard Photon Veto rejection. In this analysis, the Photon Veto rejection at the loose cut position is used for the estimation in the PV Extended Region. The coefficient 1.5 is the normalization factor from a 2/3 sample to the full sample. The $K_{\pi 2}$ background level is estimated to be

$$N_{K_{\pi 2}} = 0.216 \pm 0.023(stat.) \quad \text{in the Signal Region}, \quad (29)$$

$$N_{K_{\pi 2}} = 0.019 \pm 0.005(stat.) \quad \text{in the } 1 \times 1 \text{ Region}. \quad (30)$$

6.4 Muon Background Estimation

The Muon background consists of $K_{\mu 2}$ Range Tail events, which originate from $K_{\mu 2}$ muons with elastic (or inelastic) scattering in the Range Stack, and the Muon Band events, which originate from $K_{\mu\nu\gamma}$ and $K_{\mu 3}$ decays, or π^+ 's decaying in flight to μ^+ . In all of these events, the muon track comes to rest, or interacts in the Range Stack. The $\pi^+ \rightarrow \mu^+ \rightarrow e^+$ Decay Sequence Cuts suppress these events. On the other hand, the $K_{\mu 2}$ Range Tail events have momenta consistent with $K_{\mu 2}$ ($P = 236$ MeV/c), measured correctly in the UTC; however, their ranges (and also energies) are smaller than those from $K_{\mu 2}$, and could satisfy the Phase Space Cuts for Range and Energy ($E \leq 135$ MeV and $R \leq 40$ cm). Only the Phase Space Cut for Momentum ($P \leq 229$ MeV/c) can work to suppress this background. The Kinematic Cut targeting the Muon Band background is different from that for the $K_{\mu 2}$ Range Tail background. Muons from the Muon Band events can be in the signal phase space due to their original momenta being lower than $K_{\mu 2}$, but their ranges are longer than those expected for pions with the same momenta. The Range-Momentum Consistency Cut, Equation (24), suppresses this background. Estimations for these backgrounds are performed separately.

The Muon background level is estimated in the following way. Setup cuts are applied to the $\pi\nu\bar{\nu}(1)$ trigger sample in order to remove the $K_{\pi 2}$ and Beam backgrounds. The $\pi^+ \rightarrow \mu^+$ Double Pulse Fitting Cut is applied to select events with the $\pi^+ \rightarrow \mu^+$ decay signature. In the Rejection Branch, $K_{\mu 2}$ Range Tail events whose momenta are consistent with $K_{\mu 2}$ are selected while Muon Band events in the range deviation (χ_{R-P}) peak are selected (i.e., inverse of the Kinematic Cuts for Muon background). Phase Space Cuts for Range and Energy are imposed on both backgrounds. The rejection of the $\pi^+ \rightarrow \mu^+ \rightarrow e^+$ Decay Sequence Cuts is measured together with both backgrounds. The rejection is measured to be

$$R_{\pi\mu e} = \frac{38268}{85} = 450.2 \pm 48.8(stat.). \quad (31)$$

In the Normalization Branch, Muon events that fail the $\pi^+ \rightarrow \mu^+ \rightarrow e^+$ Decay Sequence Cuts are selected (i.e., inverse of the $\pi^+ \rightarrow \mu^+ \rightarrow e^+$ Decay Sequence Cuts). The number of Muon events remaining in the Normalization Branch is obtained by applying the Phase Space Cuts and all other Kinematic Cuts. Since only a few events remain in the Normalization Branch, the Second Bifurcation Method is performed. In the Second Bifurcation, the $K_{\mu 2}$ Range Tail and Muon Band events are separately estimated. Contaminations of the $K_{\mu 2}$ Range Tail and Muon Band backgrounds into the Signal Region are estimated by using the template momentum and range deviation distributions (referred to as the Line Shape Method).

The estimation by the Line Shape Method results in 4.65 ± 0.14 and 2.19 ± 0.14 events of the $K_{\mu 2}$ Range Tail and Muon Band backgrounds (inside the 1×1 Region) in the Normalization Branch, respectively. The numbers of events left in the Normalization Branch (N_{NB}) are summarized in Table 7. The $K_{\mu 2}$ Range Tail and Muon Band background levels in the Signal Region are obtained in the same way as the $K_{\pi 2}$ background estimation,

$$N_{\text{Muon}} = \frac{N_{NB}(PV)}{R_{\pi\mu e} - 1} + \frac{N_{NB}(\pi\mu e)}{R'_{\pi\mu e} - 1} + \frac{N_{NB}(K_{\pi 2})}{R_{\pi\mu e} - 1} - 2 \frac{N_{NB}(1 \times 1)}{R_{\pi\mu e} - 1}, \quad (32)$$

Region	N_{NB} (events)	
	Muon Band	$K_{\mu 2}$ Range Tail
1 \times 1	2.19 \pm 0.14	4.65 \pm 0.14
PV Extended	3.85 \pm 0.24	5.07 \pm 0.14
$\pi^+ \rightarrow \mu^+ \rightarrow e^+$ Extended	2.18 \pm 0.14	4.56 \pm 0.13
$K_{\pi 2}$ Kinematics Extended	2.27 \pm 0.14	4.65 \pm 0.14

Table 7: Numbers of events remaining in the Normalization Branch for the estimations of the Muon Band and $K_{\mu 2}$ Range Tail background levels. The errors are statistical.

where $R'_{\pi\mu e}$ represents a rejection of the $\pi^+ \rightarrow \mu^+ \rightarrow e^+$ Decay Sequence Cuts at the loose cut position and is by a factor of 4.2 smaller than the standard one. In this analysis, the rejection of the $\pi^+ \rightarrow \mu^+ \rightarrow e^+$ Decay Sequence Cuts at the loose cut position should be used for estimations in the $\pi^+ \rightarrow \mu^+ \rightarrow e^+$ Extended Region. The background levels in the Signal Region (and the 1 \times 1 Region) for the $K_{\mu 2}$ Range Tail and Muon Band backgrounds are summarized in Table 8.

Background	Signal Region	1 \times 1 Region
$K_{\mu 2}$ Range Tail	0.0439 \pm 0.0050	0.0103 \pm 0.0011
Muon Band	0.0244 \pm 0.0030	0.0049 \pm 0.0006
Total	0.0683 \pm 0.0058	0.0152 \pm 0.0013

Table 8: Summary of the Muon background levels. The errors are statistical.

The Muon background level is therefore estimated to be

$$N_{\text{Muon}} = 0.0683 \pm 0.0058(\text{stat.}) \quad \text{in the Signal Region,} \quad (33)$$

$$N_{\text{Muon}} = 0.0152 \pm 0.0013(\text{stat.}) \quad \text{in the } 1 \times 1 \text{ Region.} \quad (34)$$

6.5 Single Beam Background

The Single Beam background includes events in which beam pions scatter in the target, and events in which beam kaons decay in flight in the target. It is noted that the events in which K^+ decay-in-flights occur between the Čerenkov counter and target are also included in this type of background. In both cases the incoming particles scatter or decay immediately after they enter the target. The Delayed Coincidence Cuts can therefore suppress the Single Beam background. Moreover, the Timing Cuts in the beam instrumentation suppress the Single Beam background, since the times are expected to be close to the track time measured in the RS. due to the prompt scattering or decaying. The two cuts for the Bifurcation are the Delayed Coincidence Cuts and the Timing Cuts in the beam instrumentation.

The Single Beam background level is estimated in the following way. Setup cuts are applied to the $\pi\nu\bar{\nu}(1)$ trigger sample in order to remove other backgrounds. In the Rejection Branch, the Photon Veto Cuts except for the target are applied to remove $K_{\pi 2}$, $K_{\mu\nu\gamma}$, and $K_{\mu 3}$ decay-in-flight events. The Delayed Coincidence rejection is measured with the Pion Scattering events, which are tagged by requiring a small dE/dx in the B4 Hodoscope. The Delayed Coincidence rejection for K^+ decay-in-flight events is assumed to be the same as that for Pion Scattering events, since it is difficult to isolate K^+ decay-in-flight events without ambiguity. It is noted that the contribution of the K^+ decay-in-flight events is negligibly small compared to that of the Pion Scattering events. The Delayed Coincidence rejection is summarized in Table 9.

Region	Rejection
Signal Region	56178/16 = 3511.1±877.7
1×1 Region	51471/16 = 3216.9±804.1

Table 9: Rejection of the Delayed Coincidence Cuts for the Single Beam background.

In the Normalization Branch, some additional setup cuts are applied for cleanup. Prompt events are tagged by inverting the Delayed Coincidence Cuts. The Pion Scattering and K^+ decay-in-flight events are estimated together. The Timing Cut in the Kaon Čerenkov Counter, the Photon Veto Cuts and the $\pi^+ \rightarrow \mu^+ \rightarrow e^+$ Decay Sequence Cuts are applied to suppress the $K_{\pi 2}$, $K_{\mu\nu\gamma}$ and $K_{\mu 3}$ decay-in-flight events; the Timing Cut in the Pion Čerenkov Counter and the dE/dx Cut in the B4 Hodoscope are also applied to suppress the Pion Scattering events; 14 events remain in the Signal Region and 9 events remain in the 1×1 Region, respectively. With the measured Delayed Coincidence rejection, the Single Beam background level is estimated to be

$$N_{1BM} = \frac{1.5 \times 14}{3511.1 - 1} = 0.00598 \pm 0.00219(stat.) \quad \text{in the Signal Region,} \quad (35)$$

$$N_{1BM} = \frac{1.5 \times 9}{3216.9 - 1} = 0.00420 \pm 0.00175(stat.) \quad \text{in the } 1 \times 1 \text{ Region.} \quad (36)$$

The coefficient 1.5 is the normalization factor from the 2/3 sample to the full sample.

6.6 Double Beam Background

The Double Beam background consists of events with extra K^+ 's or π^+ 's in addition to the K^+ 's that come at first. The extra K^+ events ($K - K$ events) are those in which the first K^+ 's enter the target and then the second K^+ 's decay in flight and produce π^+ 's. The extra π^+ events ($K - \pi$ events) are the same as the $K - K$ events, except that the π^+ 's instead of K^+ 's scatter in the target. The Delayed Coincidence Cuts do not work on these events because the Kaon Fiber time (t_K) produced by the first K^+ and the Pion Fiber time (t_π) produced by the second K^+ or π^+ are unrelated. The Timing Cuts in the beam instrumentation (Kaon and Pion Čerenkov Counters, Beam Wire Chambers (BWPCs) and B4 Hodoscope) can reject the Double Beam background, since their timings, if recorded, are correlated to the track time produced by the extra K^+ or π^+ . The Target Pattern Recognition Cuts are also able to find extra particles other than the initial K^+ hit when the kaon cluster is apart from the second particle hits.

The Double Beam background level is estimated in the following way. Setup cuts are applied to the $\pi\nu\bar{\nu}(1)$ trigger sample in order to remove $K_{\pi 2}$, Muon and Single Beam backgrounds. In the Rejection Branch, some additional setup cuts are applied to select pion tracks. Double Beam events are selected by requiring hits in the B4 Hodoscope at the track time. The rejection of the Timing Cuts in the Kaon (Pion) Čerenkov Counter and BWPCs is measured with the $K - K$ ($K - \pi$) events tagged by requiring that the second particle has a large (small) dE/dx in the B4 Hodoscope. The rejections are summarized in Table 10.

Region	$K - K$ event	$K - \pi$ event
Signal Region	2454/28 = 87.6±16.5	43876/14 = 3134.0±837.5
1×1 Region	2323/27 = 86.0±16.5	42661/14 = 3047.2±814.3

Table 10: Rejection of the Timing Cuts in the beam instrumentation for the Double Beam background.

In the Normalization Branch, some additional setup cuts are applied. The estimations for the $K - K$ and $K - \pi$ events are separately performed with the Second Bifurcation Method.

The predicted numbers of the $K - K$ and $K - \pi$ events remaining in the Normalization Branch are $N_K = 0.16$ and $N_\pi = 0.30$ ($N_K = 0.15$ and $N_\pi = 0.29$ in the 1×1 Region), respectively. With the measured rejection of the Timing Cuts in the beam instrumentation, the Double Beam background level is estimated to be

$$N_{2beam} = 1.5 \cdot \left(\frac{0.156}{87.6 - 1} + \frac{0.298}{3134.0 - 1} \right) = 0.00284 \pm 0.00207(stat.) \quad (37)$$

in the Signal Region and

$$N_{2beam} = 1.5 \cdot \left(\frac{0.152}{86.0 - 1} + \frac{0.293}{3047.2 - 1} \right) = 0.00283 \pm 0.00207(stat.) \quad (38)$$

in the 1×1 Region.

6.7 Charge Exchange Background

A Charge Exchange (CEX) reaction of K^+ in the target creates a K_L^0 . The semi-leptonic decay of $K_L^0 \rightarrow \pi^+ l^- \bar{\nu}_l$ could produce a π^+ track with the kinematic values in the signal phase space. As described in Section 5.1, the CEX events are expected in the target to have a gap between the fibers of the incoming K^+ and the outgoing π^+ , and to have an extra l^- track; these events can be suppressed by the Target Pattern Recognition Cuts. The Delayed Coincidence Cuts also suppress them because K_L^0 should not have traveled so far away after imposing cuts on the large gap. The CEX background is therefore expected to be suppressed by the same cuts that are used for the other Beam backgrounds. The CEX background sample is difficult to be isolated from the real data. Instead of using the real data, Monte Carlo data is generated and all cuts are applied to the sample in order to estimate the remaining CEX background events.

For the Monte Carlo simulation, information on the cross section for the CEX reaction, the production points and the momentum vector of K_L^0 is necessary. Since that concerning K_S^0 and K_L^0 from the CEX reaction is the same, and the $K_S^0 \rightarrow \pi^+ \pi^-$ decay (unlike $K_L^0 \rightarrow \pi^+ l^- \bar{\nu}_l$ decay) can be reconstructed easily in the E949 detector, information concerning the K_L^0 production points and momentum vector at the points is obtained from the K_S^0 measurements with real data. The values used to calculate the K_L^0 production rate by means of $R_{K_L^0} \equiv \frac{N_{K_S^0}}{\epsilon_{K_S^0} \cdot A_{PV} \cdot \mathcal{B}(K_S^0 \rightarrow \pi^+ \pi^-) \cdot KB_{live} / PS}$. They are summarized in Table 11, and the rate is calculated to be $R_{K_L^0} = 2.73 \times 10^{-5}$.

Description	Parameter	Values
# of selected K_S^0 events	$N_{K_S^0}$	8086
K_S^0 selection efficiency	$\epsilon_{K_S^0}$	0.138
Photon Veto efficiency	A_{PV}	0.680
$K_S^0 \rightarrow \pi^+ \pi^-$ Branching Ratio	$\mathcal{B}(K_S^0 \rightarrow \pi^+ \pi^-)$	0.686
# of K^+ Triggers (10^{12})	KB_{live}	1.77
Prescale Factor	PS	384
K_L^0 Production Rate	$R_{K_L^0}$	2.73×10^{-5}

Table 11: K_L^0 production rate and the quantities that are used to estimate it.

Using the quantities measured with K_S^0 data, Monte Carlo events of both $K_L^0 \rightarrow \pi^+ \mu^- \bar{\nu}_\mu$ ($K_{\mu 3}^0$) and $K_L^0 \rightarrow \pi^+ e^- \bar{\nu}_e$ ($K_{e 3}^0$) decays are generated in order to estimate the CEX background level; 2.076×10^{11} Monte Carlo events are generated for each decay. These numbers of K_L^0 decays correspond to the number of K^+ entering the target, as

$$\begin{aligned}
 KB_{live}^{MC} &= 2.076 \times 10^{11} / R_{K_L^0} \\
 &= 7.604 \times 10^{15}.
 \end{aligned} \tag{39}$$

All of the signal selection cuts, except for the $\pi^+ \rightarrow \mu^+ \rightarrow e^+$ Decay Sequence Cuts and the Beam Cuts that are not related to the target quantities, are applied to the Monte Carlo events. 77 K_L^0 events in the Signal Region (67 in the 1×1 Region) survive, among

which 56 events are due to K_{e3}^0 decay and 21 due to $K_{\mu3}^0$ decay. The expected CEX events are estimated to be

$$\begin{aligned}
N_{CEX} &= \left(N_{pass}^{K_{e3}^0} \times \frac{KB_{live}^{real}}{KB_{live}^{MC}} + N_{pass}^{K_{\mu3}^0} \times \frac{KB_{live}^{real}}{KB_{live}^{MC}} \right) \times A \\
&= \left(56 \times \frac{1.77 \times 10^{12}}{7.604 \times 10^{15}} + 21 \times \frac{1.77 \times 10^{12}}{7.604 \times 10^{15}} \right) \times 0.250 \\
&= 0.00448 \pm 0.00051(stat.),
\end{aligned} \tag{40}$$

where $N_{pass}^{K_{e3}^0}$ and $N_{pass}^{K_{\mu3}^0}$ are the numbers of K_{e3}^0 and $K_{\mu3}^0$ events passing all cuts, KB_{live}^{real} is the KB_{live} for the real data and A is the acceptance of the cuts that are not used for the Monte Carlo CEX events, and estimated to be 0.250. The error is taken from the statistical error of the surviving Monte Carlo events.

6.8 Total Beam Background

The final Beam background levels are summarized in Table 12. The total Beam background level in the Signal Region is estimated to be

$$N_{beam} = 0.0133 \pm 0.0031(stat.). \tag{41}$$

Background	Background Level (events)	
	Signal Region	1×1 Region
1 Beam	0.0060±0.0022	0.0042±0.0018
2 Beam	0.0028±0.0021	0.0028±0.0021
CEX	0.0045±0.0005	0.0039±0.0005
Total	0.0133±0.0031	0.0109±0.0028

Table 12: Total Beam background level and the contribution from each Beam background. The errors are statistical.

6.9 Correlation study and single cut failure study

In the Bifurcation Method, it is assumed that the two Bifurcation cuts used are not correlated; if there are correlations, the estimation becomes screwed up. In order to ensure that the estimations are correct and reliable, it has to be tested whether there could be such a correlation between the two cuts or not.

The test of the correlation is performed with the events outside the Signal Region. If two Bifurcation cuts are not correlated, the background levels inside the Signal Region are correct. In other words, if the distribution of each background source both inside and outside the Signal Region is understood well by the two functions associated with the Bifurcation cuts, the amount of the background even outside the Signal Region should be estimated correctly.

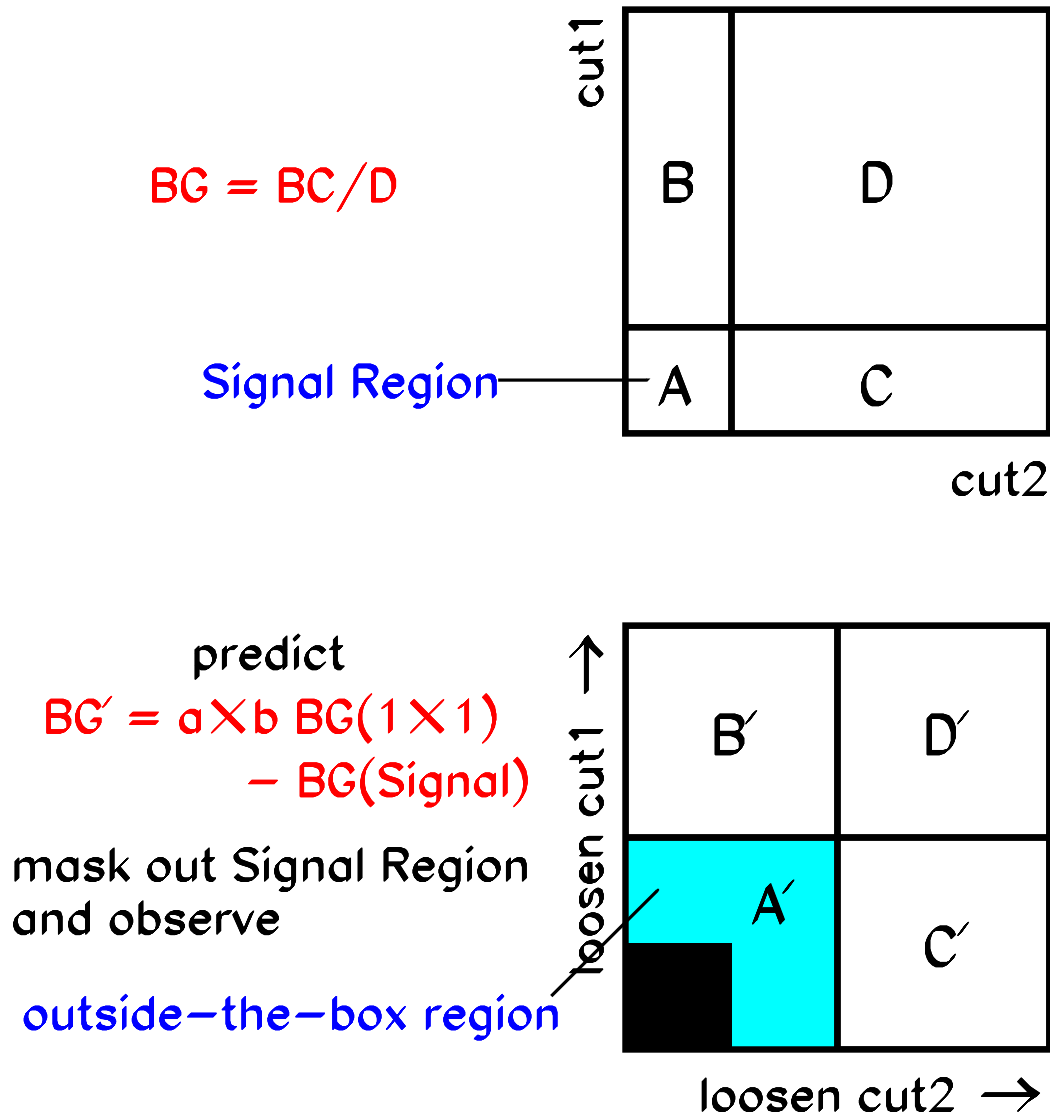


Figure 42: Pictorial explanation of the correlation study using the events outside the Signal Region.

$K_{\pi 2}$	(Photon Veto) \times ($K_{\pi 2}$ kinematics)				
	10 \times 10	20 \times 20	20 \times 50	50 \times 50	50 \times 100
	1.11 \pm 0.18 3	4.86 \pm 0.61 4	12.36 \pm 1.26 9	31.11 \pm 3.14 22	62.36 \pm 5.59 53
$K_{\mu 2}$ Range Tail	$(\pi^+ \rightarrow \mu^+ \rightarrow e^+) \times (K_{\mu 2}$ kinematics)				
	10 \times 10	20 \times 20	50 \times 50	80 \times 50	120 \times 50
	0.35 \pm 0.03 0	1.44 \pm 0.10 1	9.07 \pm 0.62 12	14.52 \pm 0.99 16	21.78 \pm 1.48 25
Muon Band	$(\pi^+ \rightarrow \mu^+ \rightarrow e^+) \times (K_{\mu 2}$ kinematics)				
	10 \times 10	20 \times 20	50 \times 20	80 \times 20	80 \times 40
	0.31 \pm 0.03 1	1.28 \pm 0.11 1	3.22 \pm 0.27 4	5.17 \pm 0.44 5	10.35 \pm 1.07 11

Table 13: Results of a correlation study for the $K_{\pi 2}$ (top), $K_{\mu 2}$ Range Tail (middle) and Muon Band (bottom) backgrounds. The first row in each background represents the loosening factors of the Bifurcation cuts; the second represents the predicted number of events in each outside-the-box region, which is obtained from Equation (42); and the third represents the number of observed events in each region. The errors in the predictions are statistical uncertainties.

Figure 42 shows a pictorial explanation of the correlation study. A region outside the Signal Region (A' in Figure 42) is defined by loosening two Bifurcation cuts (cut1 and cut2) simultaneously by certain amounts (e.g., loosening factors for the cut1 and cut2 are a and b , respectively). It should be noted that the Signal Region is still masked out. This region A' is referred to as the "outside-the-box" region. If the background functions associated with the cut1 and cut2 are correct, the expected number of background events in the outside-the-box region is estimated to be

$$BG(\text{predicted}) = a \times b \times BG(1 \times 1 \text{ Region}) - BG(\text{Signal Region}), \quad (42)$$

where $BG(1 \times 1 \text{ Region})$ and $BG(\text{Signal Region})$ are the background levels in the 1×1 and Signal Regions, respectively, which are measured in the background estimation. The number of observed events in the outside-the-box region should be compared to this predicted number of background events. If the observation does not agree with the prediction, a correlation between the Bifurcation cuts could be indicated. The observation is performed in the same way as the Bifurcation Method used in the background estimation in the Signal Region, except that two Bifurcation cuts are loosened by factors of a and b .

The results of the correlation study for the $K_{\pi 2}$, $K_{\mu 2}$ Range Tail and Muon Band backgrounds are summarized in Table 13. In this table, the first row in each background represents the loosening factors of the Bifurcation cuts; the second represents the predicted number of events in each outside-the-box region obtained from Equation (42); and the third represents the observed number of events in each region. Both the predicted and observed numbers of events are in good agreement. Figure 43 visualizes the results of the correlation study. To verify these results numerically, the observations and predictions are fitted with the form

$$N_{\text{obs}} = c \times N_{\text{pred}}, \quad (43)$$

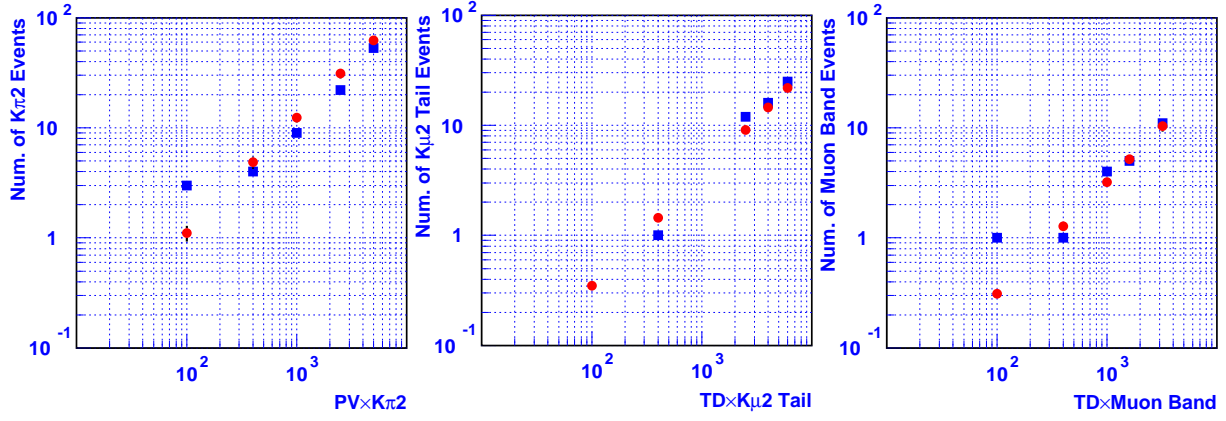


Figure 43: Visualization of the results of the correlation test for $K_{\pi 2}$ (left), $K_{\mu 2}$ Range Tail (middle), and Muon Band (right) backgrounds. The vertical axis is the number of predicted or observed events; the horizontal axis is the loosening factor. The dots represent the prediction, and square dots represent the observation.

where the values of N_{obs} and N_{pred} are arranged so as to be independent bin-to-bin. For example, the value of N_{pred} for the $K_{\pi 2}$ background for the 20×20 bin is taken as

$$\text{Prediction for } 20 \times 20 \text{ bin} = \text{Predicted}(20 \times 20) - \text{Predicted}(10 \times 10), \quad (44)$$

where $\text{Predicted}(20 \times 20)$ is the value in Table 13 for (Photon Veto) \times ($K_{\pi 2}$ Kinematics) of 20×20 . A similar procedure is used for N_{obs} . The error on N_{pred} for the 20×20 bin is taken as the difference in quadrature of the corresponding uncertainties in the table. The quantities of the fit are estimated with [6]

$$\chi^2 \equiv -2 \ln \mathcal{L} = \sum_{i=1}^5 [2(N_{th}^i - N_{obs}^i) + 2N_{obs}^i \ln(N_{obs}^i/N_{th}^i)], \quad (45)$$

where N_{obs}^i and $N_{th}^i (\equiv c \times N_{pred}^i)$ are the observed and theoretical contents of bin i , respectively. The results of the fit are summarized in Table 14.

Background	c	χ^2	χ^2 Probability
$K_{\pi 2}$	$0.850^{+0.122+0.150}_{-0.112-0.111}$	6.486	0.166
$K_{\mu 2}$ Range Tail	$1.148^{+0.245+0.156}_{-0.214-0.123}$	2.374	0.667
Muon Band	$1.063^{+0.353+0.210}_{-0.289-0.151}$	4.046	0.400

Table 14: Results of fits for the $K_{\pi 2}$, $K_{\mu 2}$ Range Tail and Muon Band backgrounds. The first and second uncertainties on c are the statistical uncertainty in N_{obs} and the uncertainty in N_{pred} , respectively.

The fit takes into account the statistical uncertainty in N_{obs} by using the above equation. To study the uncertainty in c due to the uncertainty in N_{pred} , N_{pred} is varied to be larger and smaller by the amount of uncertainty in N_{pred} , and the change in the fitted value of c is taken as an estimate of the uncertainty. The value of c for each background is close

to unity within the uncertainty. This means that the observations and predictions are consistent with each other. These results of the correlation study give us confidence that the background estimations via the Bifurcation Method are correct.

During the check on the correlations between cuts, a so-called single cut failure study is also performed, in order to find out whether or not there are any particular type of background or loop hole being missed in the study. This is done by turning off each cut and see if there is any event failing just one cut. Also checked is that if there is any correlation observed when one cut is turned off. If there is an evidence of correlation or a loop hole in the analysis, all the studies will be redone until the problem is solved.

6.10 Summary of Background Estimations

The final background levels are summarized in Table 15. The total background level in the Signal Region is estimated to be 0.297 ± 0.024 events, in which the $K_{\pi 2}$ background contribution is the largest (0.216 events). This total background level appears to be non-negligible in the expectation of a few candidate events. However, with the likelihood ratio technique, the branching ratio in this analysis is evaluated from the signal-to-background ratios of the cells where signal candidate events are observed, not from a simple counting of the number of events in the whole Signal Region and comparison with the total background level. The measured total background level is no longer a standard to judge whether the search is background-limited or not.

Background	Background Level (event)	
	Signal Region	1×1 Region
$K_{\pi 2}$	0.216 ± 0.023	0.019 ± 0.005
Muon	0.068 ± 0.006	0.015 ± 0.001
Beam	0.013 ± 0.003	0.011 ± 0.003
Total	0.297 ± 0.024	0.045 ± 0.006

Table 15: Total background level and the contribution from each background source. The errors are statistical.

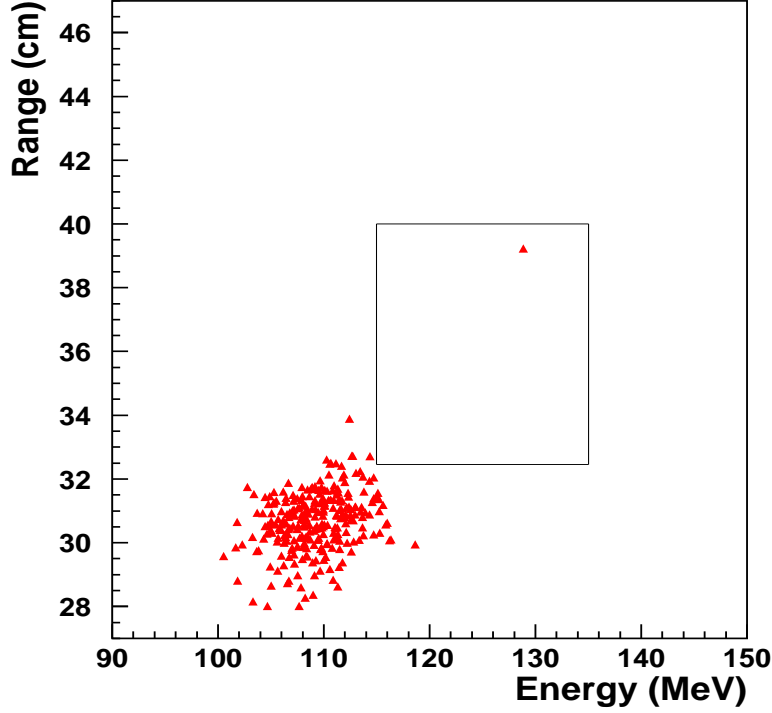


Figure 44: Range vs kinetic energy of the events satisfying all of the cuts, except for the Phase Space Cuts for Range and Energy. The rectangle represents the Signal Region in the range vs energy plane. Events around $E = 110$ MeV/c are due to $K_{\pi 2}$, which are not removed by the Photon Veto Cuts.

7 Candidate event and background probabilities

All of the signal selection criteria have been prepared as discussed in Section 5, and the background levels for all of the background sources have been estimated as explained in Section 6. The Signal Region is therefore examined with all of the $\pi\nu\bar{\nu}(1)$ trigger data.

7.1 Opening the box

One candidate event is observed near the upper kinematic limit for $K^+ \rightarrow \pi^+\nu\bar{\nu}$ decay. Figure 44 shows the range and kinetic energy of the events that pass all of the selection criteria, except for the Phase Space Cuts for Range and Energy. Figure 45 shows that the reconstruction of the candidate event is made correctly in the target, UTC and Range Stack. No other beam particle coincident with the track time is detected in the beam instrumentation. No activity is detected at the track time in the photon detectors. The properties of the candidate event are checked. No obvious flaw or loop of the data analysis is observed. The charged track of the candidate event has a momentum of $P = 227.3 \pm 2.7$ MeV/c, a kinetic energy of $E = 128.9 \pm 3.6$ MeV and a range of $R = 39.2 \pm 1.2$ cm. The momentum, kinetic energy and range distributions $K_{\pi 2}$ monitor events are also checked in the run that contains the candidate event. The corresponding peak positions and resolutions are all located at the expected values. The kinematic values of this candidate

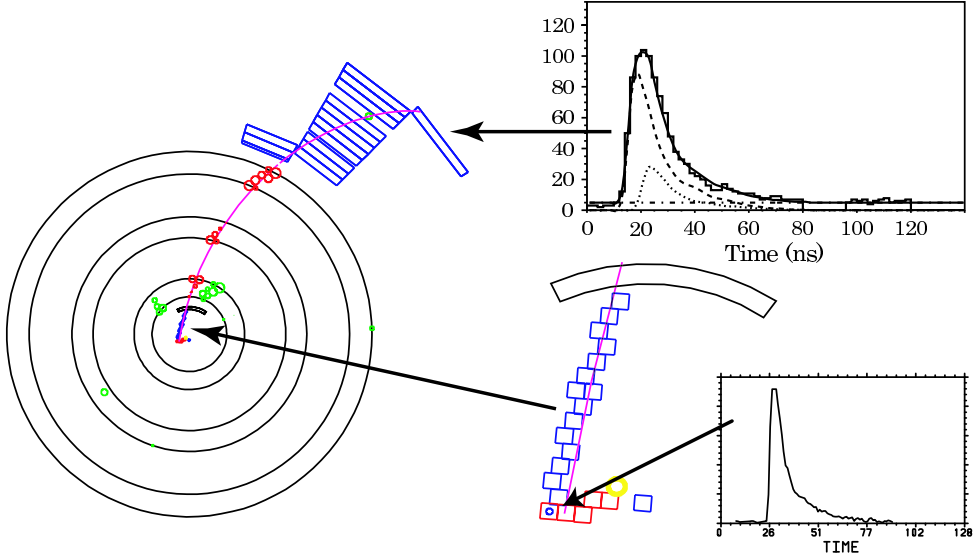


Figure 45: Reconstruction of the candidate event (end view). The TD data in the π^+ stopping counter and the reconstruction in the target are also displayed.

event are found to be near the kinematic limit of the $K^+ \rightarrow \pi^+ \nu \bar{\nu}$ decay. Comparisons with the signal distributions indicate that the candidate event has the proper kinematic quantities as a signal, although it exists in a relatively small acceptance region. Figure 46 shows the signal and background distributions of the three quantities in the Range Stack dE/dx Cuts. All of the distributions show that this event is signal-like, not background-like, and that it has a signature of neither a hard scattering nor a nuclear interaction. The possibility that this event originates from the $K_{\mu 2}$ Range Tail background is small.

The candidate event is investigated from the view point of π^+ identification with TDs. TD information in the π^+ stopping counter is shown in Figure 45. The $\pi^+ \rightarrow \mu^+$ decay time is 6.15 ns. One may doubt that the fitted double pulses are due to a tail fluctuation of a single pulse. However, π^+ 's, whose lifetime is 26 ns, could decay at early times (see Figure 47). If the first and second pulses are very close in time, the discrimination between the attached pulses becomes worse than that of detached pulses. Events with an early $\pi^+ \rightarrow \mu^+$ decay time would therefore have an ambiguity of the π^+ identification. Figure 48 shows the signal and background distributions of quantities (neurons) for the Neural Net $\pi^+ \rightarrow \mu^+$ Decay Cut in events with an early second pulse time ($T_\mu < 10$ ns). The π^+ signal events are obtained from the Pion Scattering events in the $\pi \nu \bar{\nu}(1)$ trigger by applying tight Kinematic Cuts to ensure that well-reconstructed π^+ tracks are selected. In μ^+ background events, tail fluctuation events are enhanced by imposing all of the $\pi^+ \rightarrow \mu^+ \rightarrow e^+$ Decay Sequence Cuts, except for the NN $\pi^+ \rightarrow \mu^+$ Decay Cut. With reference to the signal and background distributions in the case that the second pulse time is early, the candidate event seems to be more pion-like than muon-like with the exception of $\text{Log}_{10}(R(1) \cdot R(2))$.

In summary, this candidate event has all of the characteristics of the $K^+ \rightarrow \pi^+ \nu \bar{\nu}$ signal, although the fact that its momentum is near the kinematic limit for the $K^+ \rightarrow \pi^+ \nu \bar{\nu}$ decay and it has an early π^+ decay time of 6.15 ns gives an ambiguity concerning pion identification.

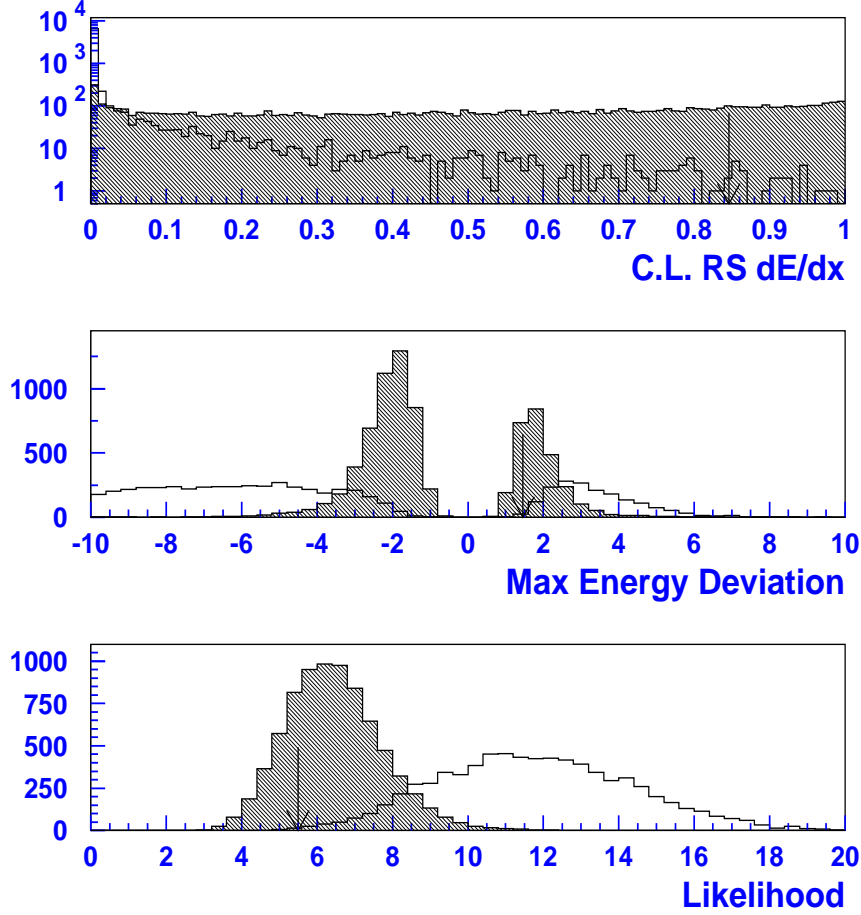


Figure 46: Distributions of the three quantities in the Range Stack dE/dx Cuts for signal (hatched) and background (opened) samples. Top, confidence level in the RS energy measurements; Middle, maximum energy deviation in the RS energy measurements; Bottom, likelihood for the RS energy measurements. The signal and background samples are obtained from the Pion Scattering and $K_{\mu 2}$ Range Tail events in the $\pi\nu\bar{\nu}(1)$ trigger, respectively. The values for the candidate event are indicated by the arrows.

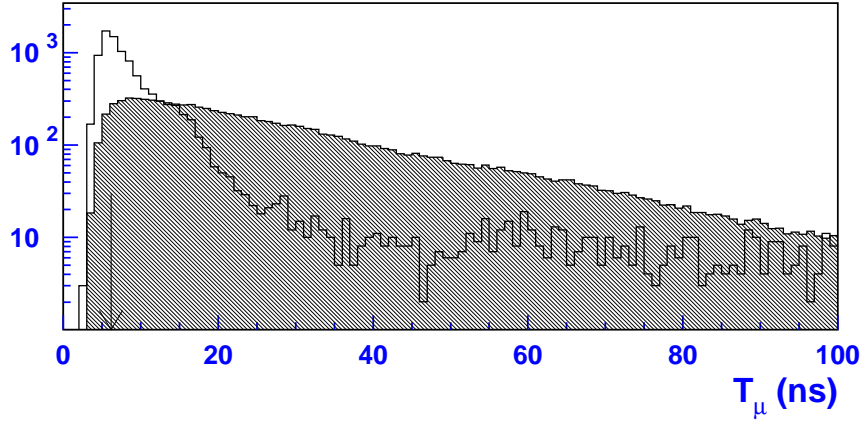


Figure 47: Distributions of the fitted second pulse time (T_μ) for π^+ signal (hatched) and μ^+ background (opened) events. Tail fluctuation events are enhanced in the μ^+ background sample. The arrow indicates the candidate event.

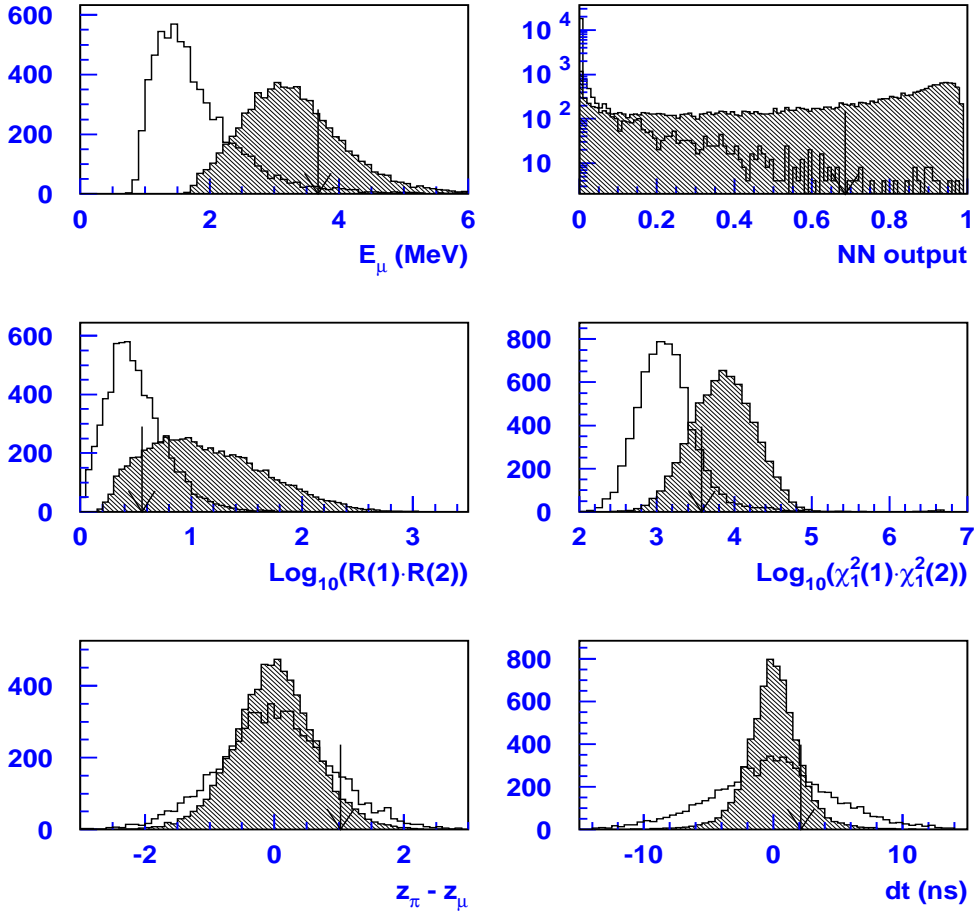


Figure 48: Quantities for the Neural Net $\pi^+ \rightarrow \mu^+$ Decay Cut in events with an early second pulse time ($T_\mu < 10$ ns). The hatched histograms are for the π^+ signal and the opened ones are for the μ^+ background. The arrows indicate the candidate event. The definition for each variable is explained in Section 5.5.

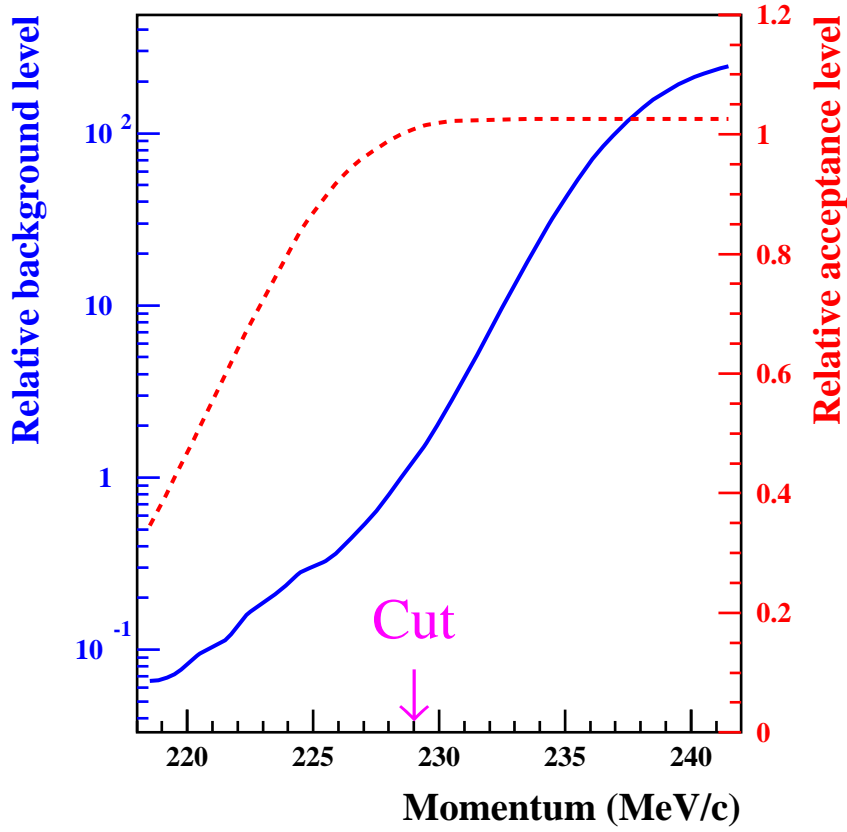


Figure 49: Background and acceptance functions related to the kinematics of the $K_{\mu 2}$ Range Tail background.

7.2 Background distributions inside the box

In determining the branching ratio of $K^+ \rightarrow \pi^+ \nu \bar{\nu}$, the probability of backgrounds for the candidate event is also taken into account. Therefore, it is necessary to measure the background distributions inside the signal box and to construct the so-called background functions.

7.2.1 $K_{\mu 2}$ background function

Because $K_{\mu 2}$ background contributes to the signal box via two ways. When the momentum is greater than 220 MeV/c, it is thought to be through momentum resolution effect. Otherwise it is through the range-momentum resolution effect.

Figure 49 shows the values of the $K_{\mu 2}$ Range Tail functions at the different cut positions of the momentum. The background levels (solid line) and acceptances (dashed line) are normalized to those at the standard cut position (momentum at 229 MeV/c). The background levels are measured with the $K_{\mu 2}$ Range Tail events in the $\pi \nu \bar{\nu}(1)$ trigger and the acceptances are measured with the Monte Carlo $K^+ \rightarrow \pi^+ \nu \bar{\nu}$ events.

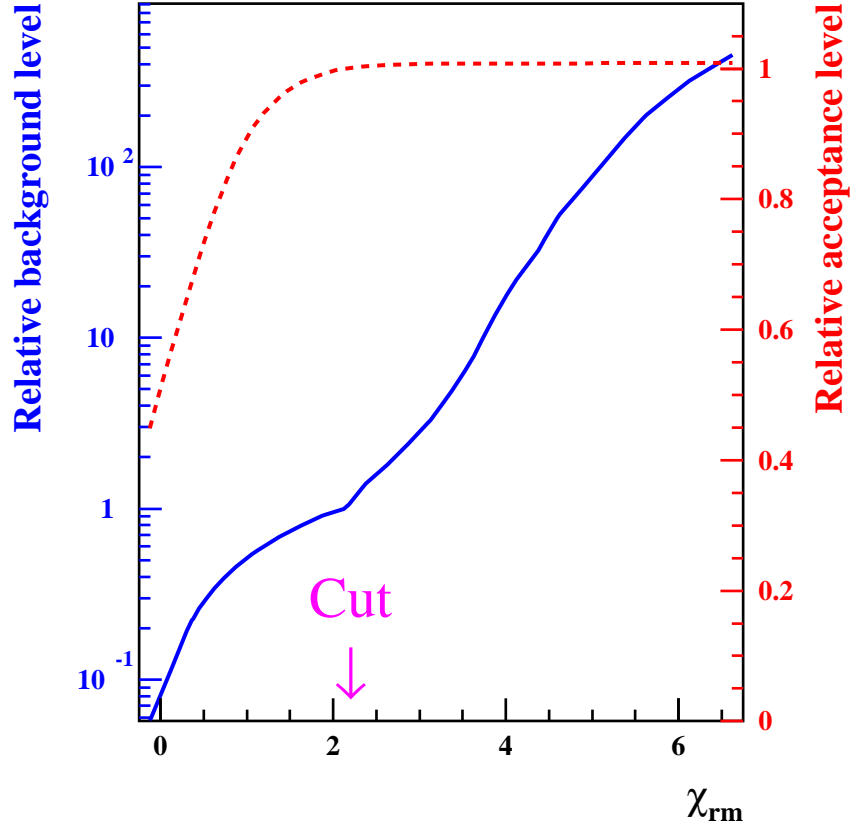


Figure 50: Background and acceptance functions related to the kinematics of the Muon Band background.

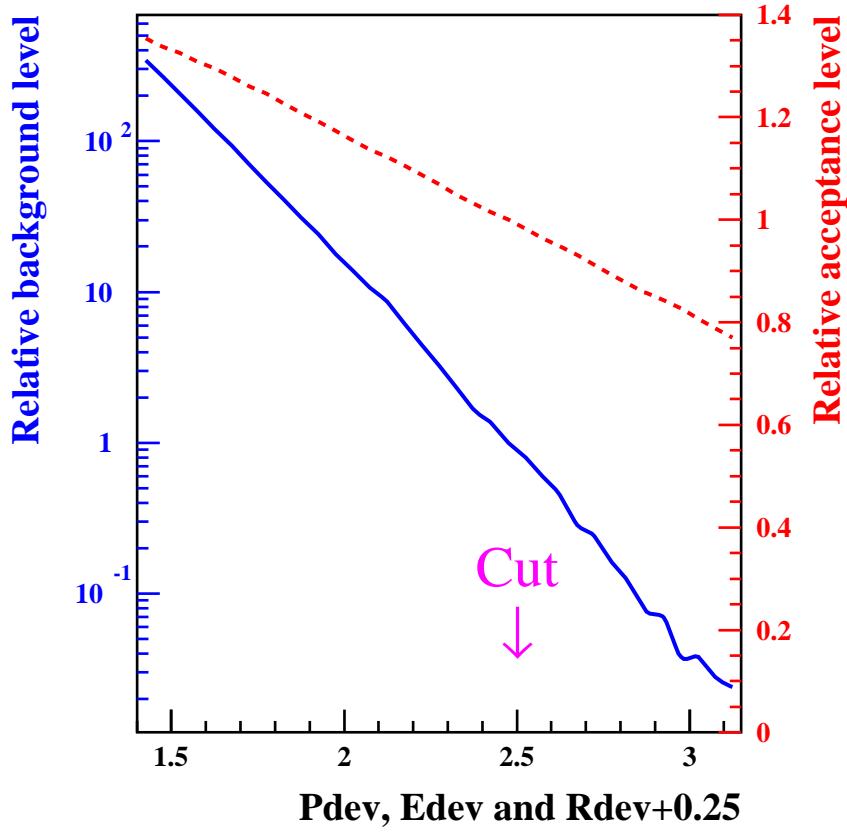


Figure 51: Background and acceptance functions related to the $K_{\pi 2}$ kinematics.

Figure 50 shows the values of the Muon Band functions at the different χ_{rm} cut positions. The background levels (solid line) and acceptances (dashed line) are normalized to those at the standard cut position (range deviation = 2.20). The background levels are measured with the Muon Band events in the $\pi\nu\bar{\nu}(1)$ trigger and the acceptances are measured with the Pion Scattering events in the $\pi\nu\bar{\nu}(1)$ trigger.

7.2.2 $K_{\pi 2}$ background function

Figure 51 shows the values of the $K_{\pi 2}$ kinematic functions at the different cut positions of momentum, energy and range deviations. The background levels (solid line) and acceptances (dashed line) are normalized to those at the standard cut position ($P_{dev} = 2.50$, $E_{dev} = 2.50$, $R_{dev} = 2.75$). The background levels are measured with the $K_{\pi 2}$ events in the $\pi\nu\bar{\nu}(1)$ trigger and the acceptances are measured with the Monte Carlo $K^+ \rightarrow \pi^+\nu\bar{\nu}$ events.

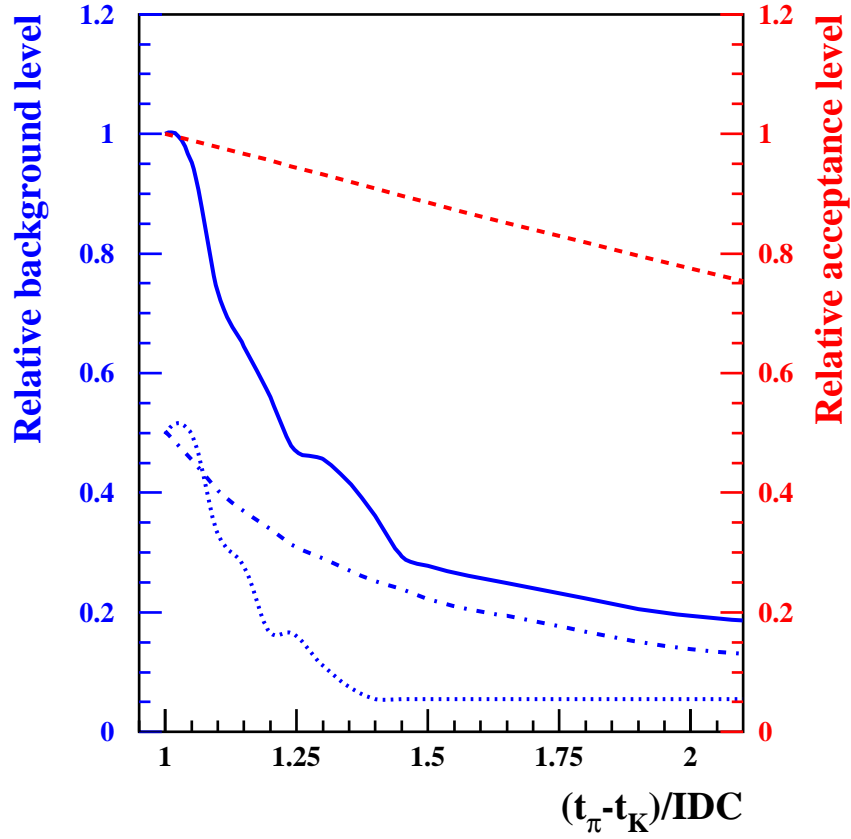


Figure 52: Background and acceptance functions related to the Single Beam background. The 1st column represents "normalized delayed coincidence", which is $t_\pi - t_K$ divided by the cut positions for the various Delayed Coincidence conditions (i.e., $idc = 2, 3, 4, 5, 6$ ns).

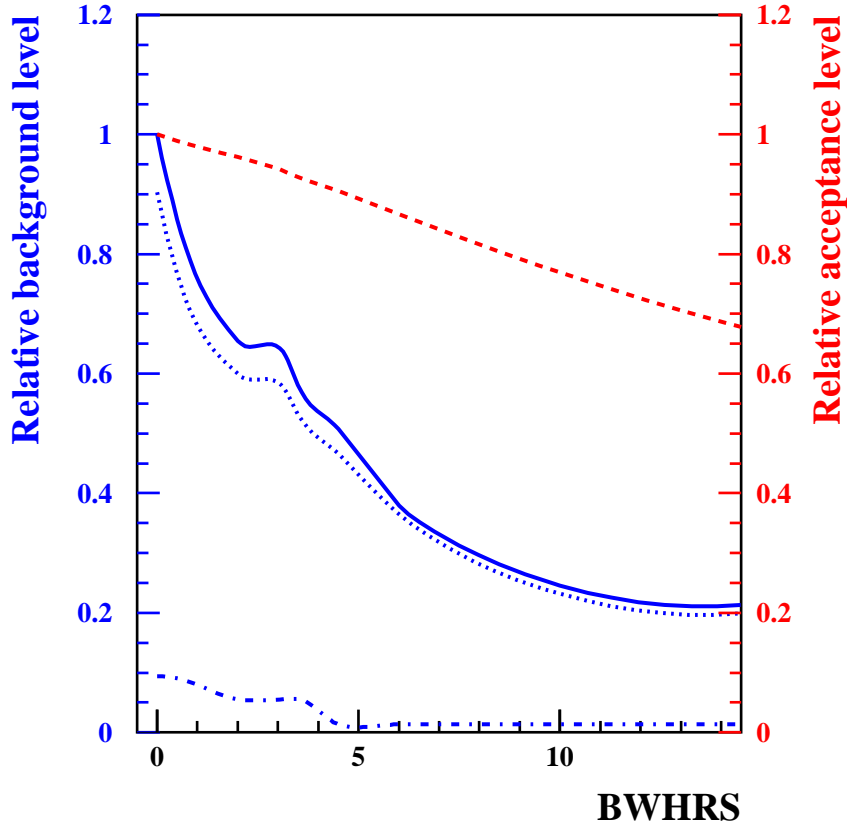


Figure 53: Background and acceptance functions related to the Double Beam background.

7.2.3 Single beam background function

Figure 52 shows the values of the 1-Beam functions at the different cut positions of Delayed Coincidence. The background levels (solid line) and acceptances (dashed line) are normalized to those at the standard cut position ($(t_\pi - t_K)/idc = 1.00$). The dotted-dashed line and dotted line represent the background levels for Single Beam background and CEX background, respectively. The background levels for Single Beam (CEX) background are measured with the Single Beam background sample in the $\pi\nu\bar{\nu}(1)$ trigger (Monte Carlo CEX events), and the acceptances are measured with the stopped kaon events in the $K_{\mu 2}$ monitor trigger.

7.2.4 Double beam background function

Figure 53 shows the values of the 2-Beam functions at the different cut positions of the timing in the BWPCs. The background levels (solid line) and acceptances (dashed line) are normalized to those at the standard cut position (BWPC timing = 0.00). The dotted and dotted-dashed lines represent the background levels for $K - K$ and $K - \pi$ Double Beam backgrounds, respectively. The background levels are measured with the Double

Beam events in the $\pi\nu\bar{\nu}(1)$ trigger and the acceptances are measured with the single kaon beam events in the $K_{\mu 2}$ monitor trigger.

8 Acceptance Measurement and Sensitivity

In this analysis, we make full use of the well known physics processes from a stopped kaon decay, measuring the acceptances whenever it is possible. Except for the acceptances of phase space and most of the trigger conditions, all the rest are measured using the $K_{\mu 2}$, $K_{\pi 2}$, $\pi - scat$ and $K - beam$.

8.1 Acceptance Measurements

The acceptances of both online and offline signal-selection cuts are estimated in order to measure the branching ratio of the $K^+ \rightarrow \pi^+ \nu \bar{\nu}$ decay. Most of the acceptance factors are measured by using monitor trigger data. The acceptance factors that are related to the $K^+ \rightarrow \pi^+ \nu \bar{\nu}$ kinematics are derived from Monte Carlo simulations. The monitor trigger data used for the acceptance measurements are tabulated in Table 16.

Data	Acceptance Factor
$K_{\mu 2}$	Reconstruction efficiency Beam and target analysis Accidental loss (Photon Veto, accidental muon veto) K^+ stop efficiency
$K_{\pi 2}$	Target reconstruction related to pion tracks
$\pi_{scatter}$	Kinematics related to pion tracks $\pi^+ \rightarrow \mu^+ \rightarrow e^+$ decay acceptance
$K^+ \rightarrow \pi^+ \nu \bar{\nu}$ (MC)	Trigger acceptance Phase space and Solid angle π^+ nuclear interactions and decay-in-flight

Table 16: Monitor triggers and the acceptance factors.

The signature of the $K_{\mu 2}$ decay (a single charged track and no other activities from the kaon decay) is the same as that of the $K^+ \rightarrow \pi^+ \nu \bar{\nu}$ signals. $K_{\mu 2}$ events are therefore suitable to measure the charged-track reconstruction efficiency, the beam and target analysis acceptances, and the accidental loss due to both online and offline Photon Veto Cuts.

$K_{\pi 2}$ decay is suitable for calculating the acceptances of the Target Reconstruction Cuts, which involve energy loss of pion tracks.

Pion Scattering events provide pion tracks whose stopping layer spreads throughout the Range Stack. They are useful to measure the acceptances of the kinematic constraints on pion tracks (RS dE/dx Cuts, track reconstruction in the UTC and RS, etc). They are also used to measure the $\pi^+ \rightarrow \mu^+ \rightarrow e^+$ decay acceptance.

The trigger acceptance, the phase-space and solid-angle acceptances, and the acceptance loss due to pion nuclear interactions and decay-in-flights are obtained by using Monte Carlo simulations of the $K^+ \rightarrow \pi^+ \nu \bar{\nu}$ decay, because they are related to the $K^+ \rightarrow \pi^+ \nu \bar{\nu}$ kinematics and can not be measured by using any monitor trigger data.

There are other acceptance factors: one is the T·2 efficiency, where T·2 is the trigger bit that requires a coincident hit in the first two layers of the RS counters. The definition is explained in Section 2.7, and the another is the K^+ stop efficiency. The T·2 efficiency accounts for the efficiency of the trigger counter in the Range Stack (i.e., T-Counter). The

acceptance loss due to the counter inefficiency and the geometrical inefficiency (which is due to azimuthal gaps between sectors) is estimated with both $K_{\pi 2}$ and $K_{\mu 2}$ events.

The K^+ stop efficiency is the fraction of kaons stopping in the target to those entering the target and satisfying the KB requirement. $K_{\mu 2}$ decay is used for this measurement because the signature of $K_{\mu 2}$ events is similar to that of $K^+ \rightarrow \pi^+ \nu \bar{\nu}$. This acceptance is calculated by taking the ratio of the number of stopped $K_{\mu 2}$ decays to the number of K^+ triggers times the $K_{\mu 2}$ branching ratio. Some selection cuts are required to select the stopped $K_{\mu 2}$ decays. The K^+ stop efficiency is therefore given as

$$K^+ \text{ Stop } Eff. = \frac{\text{Num. of Stopped } K_{\mu 2} \text{ Decays}}{K^+ \text{ Trigger}(K_{\mu 2}) \cdot A_{\text{selection cuts}} \cdot \mathcal{B}(K_{\mu 2})}, \quad (46)$$

where $A_{\text{selection cuts}} \equiv A_{\text{bad run}} \cdot A_{\text{trigger}} \cdot A_{\text{polar angle}} \cdot A_{\text{range}} \cdot A_{\text{recon}} \cdot$
 $A_{\text{beam\&target}} \cdot A_{\text{photon veto}} \cdot A_{T\bullet 2}.$

Here, $A_{T\bullet 2}$ is the T-2 efficiency for $K_{\mu 2}$. The $K_{\mu 2}$ branching ratio is taken from the Particle Data Group (PDG) value. Stopped $K_{\mu 2}$ events are selected by applying the cuts given in Table 17. The acceptances of the selection cuts are measured as shown in Table 18. The acceptances of the trigger (A_{trigger}), the polar angle cut ($A_{\text{polar angle}}$) and the range requirement (A_{range}) are obtained from the Monte Carlo $K_{\mu 2}$ events. The other acceptances are obtained from the $K_{\mu 2}$ monitor trigger data.

The K^+ stop efficiency is measured to be

$$K^+ \text{ Stop } Eff. = 0.7740 \pm 0.0011(stat.). \quad (47)$$

The acceptances of the $K^+ \rightarrow \pi^+ \nu \bar{\nu}$ signal selection cuts are summarized in Table 19. Each factor (written in bold) is composed of several components (in parentheses), whose acceptances are estimated using the monitor trigger data and Monte Carlo simulations. Measurements of the phase-space and solid-angle acceptance, the $\pi^+ \rightarrow \mu^+ \rightarrow e^+$ decay acceptance, and the accidental loss for the Signal Region are performed by loosening the corresponding cut without the other two cuts loosened. The total acceptance for the Signal Region is obtained by summing the total acceptance in the 1×1 Region and the acceptance gains from the three Extended Regions. The total acceptance in the Signal Region is therefore measured to be

$$A_{\text{total}} = 0.00222 \pm 0.00007(stat.) \pm 0.00018(sys.). \quad (48)$$

This value is greater by a factor of 1.31 than the total acceptance in the 1×1 Region.

8.2 $K_{\pi 2}$ Branching Ratio Measurement

The $K_{\pi 2}$ branching ratio is measured in order to confirm that the way to measure the acceptances of the $K^+ \rightarrow \pi^+ \nu \bar{\nu}$ selection cuts is correct. Stopped $K_{\pi 2}$ events are selected from the $K_{\pi 2}$ monitor trigger data by imposing the cuts given in Table 20. The Phase Space Cuts in this selection are defined to be in the $\pm 3\sigma$ region of the $K_{\pi 2}$ peaks in the

Cut	# of remaining events
Sample	1010924
Bad Run	1010318
Reconstruction Cuts	806196
Polar Angle	795506
Beam and Target Cuts	393245
Photon Veto Cuts	359031
Range Requirement	355119
Stopped $K_{\mu 2}$ Decays	355119

Table 17: Numbers of events passing the $K_{\mu 2}$ selection cuts and the number of stopped $K_{\mu 2}$ decays used in the K^+ stop efficiency measurement.

Stopped $K_{\mu 2}$ Decays	355119
K^+ Trigger ($K_{\mu 2}$)	4.1475×10^6
$A_{bad\ run}$	0.9994
$A_{trigger}$	0.4415
$A_{polar\ angle}$	0.9866
A_{range}	0.9877
A_{recon}	0.8388
$A_{beam\&\ target}$	0.5585
$A_{photon\ veto}$	0.9295
$A_{T \bullet 2}$	0.9303
$\mathcal{B}(K_{\mu 2})$	0.6351
K^+ Stop Efficiency	0.7740 ± 0.0011

Table 18: Summary of the K^+ stop efficiency measurement.

Factor	Acceptance		Data
	Signal Region	1×1 Region	
Trigger acceptance (A_{trig})	0.1796±0.0010±0.0090		MC
K^+ stop efficiency (A_{K^+stop})	0.7740±0.0011		$K_{\mu 2}$
Beam and target analysis (A_{beam} w/o RTDIF,PIGAP,TGB4)	0.5483±0.0007		$K_{\mu 2}$
Phase space and solid angle (Phase Space)	0.4020±0.0030	0.3662±0.0030	MC
(COS3D)	0.4458 ± 0.0032	0.4061 ± 0.0032	MC
(ZFRF)	0.9687 ± 0.0011		MC
(ZUTOUT)	0.9312 ± 0.0016		MC
	0.9998 ± 0.0001		MC
π^+ nucl. int. and decay-in-flight (A_{NIDIF})	0.4953±0.0077±0.0248		MC
Reconstruction efficiency (A_{recon})	0.9956±0.0001		$K_{\mu 2}$
Other kinematics constraints ($A_{K\pi 2}$)	0.5013±0.0071±0.0154		$K_{\pi 2}$
(RTDIF)	0.8785 ± 0.0029		$K_{\mu 2}$
(PIGAP)	0.9893 ± 0.0002		$K_{\mu 2}$
(TGB4)	0.9917 ± 0.0002		$K_{\mu 2}$
($A_{\pi scatter}$)	0.9440 ± 0.0004		$K_{\mu 2}$
	0.6161 ± 0.0085 ± 0.0189		$\pi_{scatter}$
$\pi^+ \rightarrow \mu^+ \rightarrow e^+$ decay acceptance (UFATE)	0.3914±0.0085±0.0074	0.3495±0.0076±0.0067	MC
(USTMED)	1.0000		MC
(USTOP_HEX)	0.9948 ± 0.0004		MC
($A_{\pi \rightarrow \mu \rightarrow e}$)	0.9971 ± 0.0003		$\pi_{scatter}$
	0.3946 ± 0.0086 ± 0.0075	0.3523 ± 0.0077 ± 0.0067	
Accidental loss (A_{PV})	0.8204±0.0019	0.7509±0.0022	$K_{\mu 2}$
($A_{LAYER14}$)	0.8389 ± 0.0019	0.7678 ± 0.0022	$K_{\mu 2}$
(A_{acc})	0.9820 ± 0.0002		$K_{\mu 2}$
	0.9959 ± 0.0006		$K_{\mu 2}$
T·2 efficiency ($A_{T\bullet 2}$)	0.9357±0.0011±0.0168		$K_{\mu 2}, K_{\pi 2}$
Total acceptance	(2.22±0.07±0.18) × 10⁻³	(1.69±0.05±0.16) × 10⁻³	

Table 19: Acceptances for the $K^+ \rightarrow \pi^+ \nu \bar{\nu}$ analysis. Each factor (written in bold) consists of several components (in parentheses). The first and second uncertainties represent the statistical and systematic uncertainties, respectively. The 3rd and 4th columns represent the data and the reference for each component.

Cut	# of remaining events
Sample	84844
Bad Run	84388
Reconstruction Cuts	65495
Polar Angle	64425
Beam and Target Cuts	26523
$\pi^+ \rightarrow \mu^+ \rightarrow e^+$ Decay Requirement	18688
Stopping Layer Cut	16469
Phase Space Cuts	16405
Stopped $K_{\pi 2}$ Decays	16405

Table 20: Numbers of events passing the $K_{\pi 2}$ selection cuts and the number of stopped $K_{\pi 2}$ decays used in the $K_{\pi 2}$ branching ratio measurement.

momentum, range and energy. The $K_{\pi 2}$ branching ratio is calculated as

$$\mathcal{B}(K_{\pi 2}) = \frac{\text{Num. of Stopped } K_{\pi 2} \text{ Decays}}{K^+ \text{ Trigger}(K_{\pi 2}) \cdot A_{\text{selection cuts}} \cdot A_{K^+ \text{ stop}}}, \quad (49)$$

where $A_{\text{selection cuts}} \equiv A_{\text{bad run}} \cdot A_{\text{trigger}} \cdot A_{\text{recon}} \cdot A_{\text{polar angle}} \cdot A_{\text{phase space}} \cdot A_{\pi \rightarrow \mu \rightarrow e} \cdot A_{\text{beam\&target}} \cdot A_{T \bullet 2}$.

Here, $A_{K^+ \text{ stop}}$ is the K^+ stop efficiency obtained from Equation (47), $A_{\pi \rightarrow \mu \rightarrow e}$ is the acceptance of the $\pi^+ \rightarrow \mu^+ \rightarrow e^+$ decay requirement, and $A_{T \bullet 2}$ is the T·2 efficiency for $K_{\pi 2}$. The acceptances of the selection cuts are measured as shown in Table 21. The acceptances of the trigger (A_{trigger}), the polar angle cut ($A_{\text{polar angle}}$) and the Phase Space Cuts ($A_{\text{phase space}}$) are obtained from the Monte Carlo $K_{\pi 2}$ events, while the other acceptances are obtained from the $K_{\pi 2}$ monitor trigger data. The acceptance of the $\pi^+ \rightarrow \mu^+ \rightarrow e^+$ decay requirement is obtained from the π_{scatter} monitor trigger data by applying the Phase Space Cuts for $K_{\pi 2}$ as the setup, instead of those for $K^+ \rightarrow \pi^+ \nu \bar{\nu}$. Figure 54 shows the variation of $K_{\pi 2}$ branching ratio as a function of run. A stable branching ratio is observed. The $K_{\pi 2}$ branching ratio is measured to be

$$\mathcal{B}(K_{\pi 2}) = 0.2190 \pm 0.0050(\text{stat.}). \quad (50)$$

This value agrees with the PDG value 0.212 ± 0.001 within 3.3%, which give us confidence that the acceptance measurements are correct.

8.3 Summary of Acceptance and Sensitivity

Once the acceptances of the $K^+ \rightarrow \pi^+ \nu \bar{\nu}$ selection cuts are measured, the sensitivity for the $K^+ \rightarrow \pi^+ \nu \bar{\nu}$ analysis in E949 is calculated. In the physics run of the E949 the number of the K^+ triggers for $K^+ \rightarrow \pi^+ \nu \bar{\nu}$ was 1.77×10^{12} . By using the measured total acceptance of $0.00222 \pm 0.00007(\text{stat.}) \pm 0.00015(\text{sys.})$, the sensitivity of the E949 2002 run is calculated to be

$$\text{Sensitivity } (K^+ \rightarrow \pi^+ \nu \bar{\nu}) = (2.55 \pm 0.08 \pm 0.18) \times 10^{-10}, \quad (51)$$

where the first and second uncertainties represent the statistical and systematic uncertainties, respectively. The total acceptance and the sensitivity for the $K^+ \rightarrow \pi^+ \nu \bar{\nu}$ analysis are summarized in Table 22.

Stopped $K_{\pi 2}$ Decays	16405
K^+ Trigger ($K_{\pi 2}$)	1.3233×10^6
$A_{bad\ run}$	0.9946
$A_{trigger}$	0.2782
A_{recon}	0.8439
$A_{polar\ angle}$	0.9839
$A_{phase\ space}$	0.9126
$A_{stopping\ layer}$	0.9633
$A_{\pi \rightarrow \mu \rightarrow e}$	0.8350
$A_{beam \& target}$	0.4622
$A_{T \bullet 2}$	0.9383
$A_{K^+ stop}$	0.7740
$\mathcal{B}(K_{\pi 2})$	0.2190 ± 0.0050

Table 21: Summary of the $K_{\pi 2}$ branching ratio measurement.

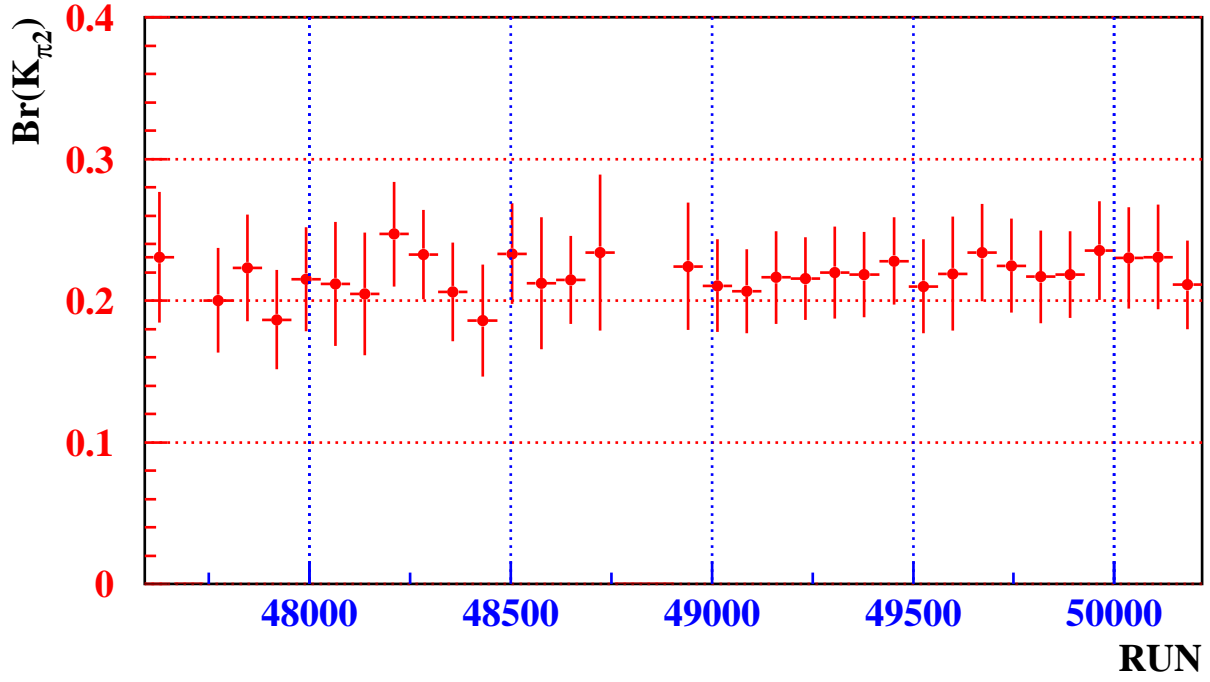


Figure 54: Measurement of the $K^+ \rightarrow \pi^+ \pi^0$ branching ratio as a function of run number in BNL-E949.

	Signal Region	1×1 Region
K^+ Trigger ($K^+ \rightarrow \pi^+ \nu \bar{\nu}$)	1.77×10^{12}	1.77×10^{12}
Total Acceptance	$(2.22 \pm 0.07 \pm 0.15) \times 10^{-3}$	$(1.69 \pm 0.05 \pm 0.14) \times 10^{-3}$
Sensitivity	$(2.55 \pm 0.08 \pm 0.18) \times 10^{-10}$	$(3.34 \pm 0.11 \pm 0.27) \times 10^{-10}$

Table 22: Acceptance and sensitivity for the $K^+ \rightarrow \pi^+ \nu \bar{\nu}$ analysis. The first and second uncertainties represent the statistical and systematic uncertainties, respectively.

Function	Bin	$N(BG)$
$K_{\pi 2}$ kinematics	$0.0 \leq N_{K\pi 2} < 0.2$	0.00
PV	$0.1 < N_{PV} < 0.2$	0.11
Muon Band	$0.0 < N_{Band} < 0.5$	0.29
$K_{\mu 2}$ Range Tail	$0.4 < N_{Tail} < 0.6$	0.51
$\pi^+ \rightarrow \mu^+ \rightarrow e^+$	$1.0 < N_{\pi \rightarrow \mu \rightarrow e} < 1.5$	1.23
1-Beam	$0.0 \leq N_{1beam} < 0.2$	0.00
2-Beam	$0.0 \leq N_{2beam} < 0.2$	0.00

Table 23: Bin in each background function (2nd column) and relative background level (3rd column) for the candidate event.

Source	Background Level (event)
$\bar{K}_{\pi 2}$	0.029×10^{-5}
Muon	5.632×10^{-5}
(Muon Band)	(0.715×10^{-5})
($K_{\mu 2}$ Range Tail)	(4.917×10^{-5})
1 Beam (including CEX)	0.058×10^{-5}
2 Beam	0.026×10^{-5}
Total Background b_i	5.745×10^{-5}
Relative Cell Acceptance A_i	1.210×10^{-4}

Table 24: Contribution of each background source to the background level in the cell for the candidate event. Each background level is represented as the number of events. The ratio of the acceptance in the cell to the total acceptance in the 1×1 Region is also tabulated in this table.

9 Statistical issues in determining the branching ratio

In this section, we will present how to extract the branching ratio of $K^+ \rightarrow \pi^+ \nu \bar{\nu}$ based on our knowledge for the background distribution in the single box. This can give a proper weight in determining the branching ratio.

9.1 Signal/noise cells definitions and Likelihood estimator

The $K^+ \rightarrow \pi^+ \nu \bar{\nu}$ branching ratio is measured via a likelihood analysis. All of the cells inside the Signal Region are pre-determined before an examination of the Signal Region. The cell for the candidate event is defined by the bins in the functions, as shown in Table 23. The background levels of all the background sources in this cell are summarized in Table 24. The largest contribution to the total background level in this cell (5.745×10^{-5} events) is the $K_{\mu 2}$ Range Tail background (4.917×10^{-5} events). The ratio of the acceptance in this cell to the total acceptance in the 1×1 Region ($A_{total}^{1 \times 1} = 0.001694$) is estimated to be 1.21×10^{-4} . The expected number of signal events in this cell is therefore

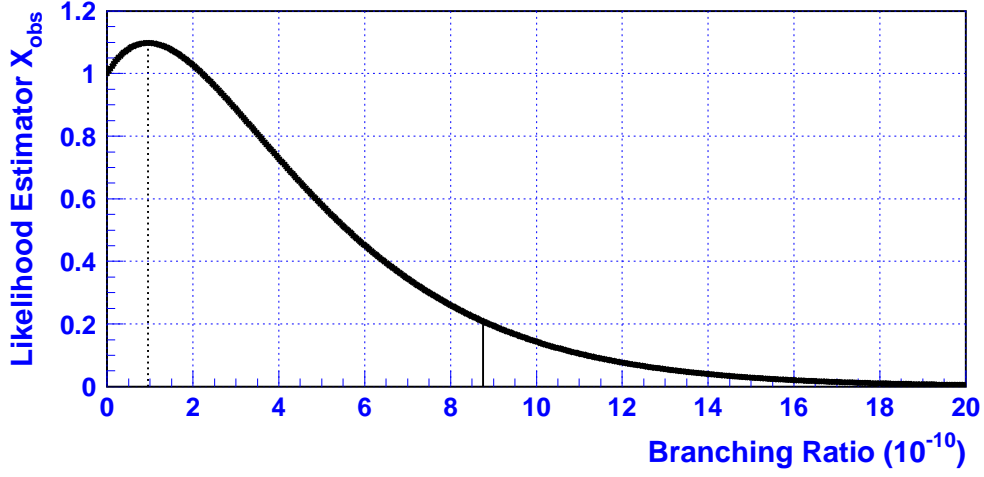


Figure 55: Likelihood estimator, X_{obs} , for the E949 2002 data set as a function of the $K^+ \rightarrow \pi^+ \nu \bar{\nu}$ branching ratio, \mathcal{B} .

calculated as

$$\begin{aligned}
 s_i &= N_K \cdot \mathcal{B} \cdot A_{total}^{1 \times 1} \cdot A_i \\
 &= 1.770 \times 10^{12} \cdot \mathcal{B} \cdot 0.001694 \cdot 1.21 \times 10^{-4} \\
 &= 3.628 \times 10^5 \cdot \mathcal{B},
 \end{aligned} \tag{52}$$

where \mathcal{B} represents the $K^+ \rightarrow \pi^+ \nu \bar{\nu}$ branching ratio and N_K is the number of K^+ triggers for $K^+ \rightarrow \pi^+ \nu \bar{\nu}$. With these expected number and background level in the candidate event cell, the likelihood estimator, X :

$$X \equiv \prod_{i=1}^n X_i, \quad \text{with} \quad X_i = \frac{e^{-(s_i+b_i)}(s_i+b_i)^{d_i}}{d_i!} / \frac{e^{-b_i}(b_i)^{d_i}}{d_i!} = e^{-s_i} \left(1 + \frac{s_i}{b_i}\right)^{d_i} \tag{53}$$

gives the central value of the $K^+ \rightarrow \pi^+ \nu \bar{\nu}$ branching ratio when the likelihood estimator with the given configuration of $\{s_i\}$, $\{b_i\}$ and $\{d_i\}$ (referred to as X_{obs}) gives the maximum value.

9.2 Branching ratio of $K^+ \rightarrow \pi^+ \nu \bar{\nu}$

Figure 55 shows the likelihood estimator, X_{obs} , as a function of the $K^+ \rightarrow \pi^+ \nu \bar{\nu}$ branching ratio, \mathcal{B} . This plot indicates that, even though X_{obs} has the maximum value at $\mathcal{B} = 0.96 \times 10^{-10}$, the case that $\mathcal{B} = 0$ is not necessarily ruled out because the candidate event observed in the E949 data has a small signal-to-background ratio. An upper limit for $\mathcal{B}(K^+ \rightarrow \pi^+ \nu \bar{\nu})$ is calculated with a Bayesian approach. Assuming that $X_{obs}(\mathcal{B})$ represents the probability density function for the branching ratio, one can have the probability to obtain a branching ratio, \mathcal{B} , with a given X_{obs} as follow

$$P(\mathcal{B}|X_{obs}) = \frac{X_{obs}(\mathcal{B})S(\mathcal{B})}{\int_{-\infty}^{+\infty} X_{obs}(\mathcal{B})S(\mathcal{B})d\mathcal{B}}, \tag{54}$$

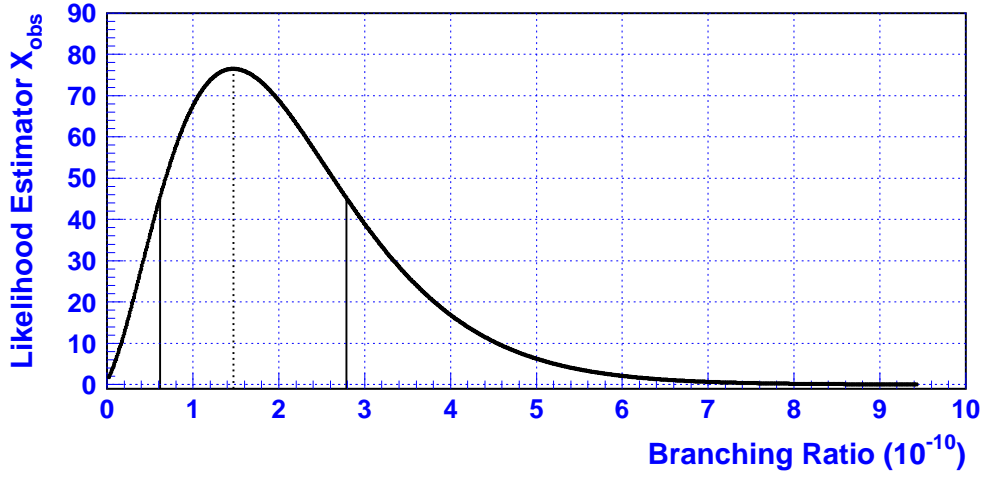


Figure 56: Likelihood estimator, X_{obs} , for the combined E787 and E949 results as a function of the $K^+ \rightarrow \pi^+ \nu \bar{\nu}$ branching ratio, \mathcal{B} .

where $S(\mathcal{B}) = 1$ when $\mathcal{B} \geq 0$ and $S(\mathcal{B}) = 0$ when $\mathcal{B} < 0$. The confidence level $(1 - \alpha)$ is calculated as

$$1 - \alpha = \int_{-\infty}^{\mathcal{B}_0} P(\mathcal{B}|X_{obs})d\mathcal{B} = \frac{\int_0^{\mathcal{B}_0} X_{obs}(\mathcal{B})d\mathcal{B}}{\int_0^{+\infty} X_{obs}(\mathcal{B})d\mathcal{B}}. \quad (55)$$

With Equations (54) and (55), an upper limit for $\mathcal{B}(K^+ \rightarrow \pi^+ \nu \bar{\nu})$ at the 90% confidence level (CL) is obtained as

$$\mathcal{B}(K^+ \rightarrow \pi^+ \nu \bar{\nu}) < 8.76 \times 10^{-10} \quad (90\% \text{ CL}) \quad (56)$$

based on the single candidate event. This limit is consistent with the previous results from E787.

The results from both E787 and E949 are combined to calculate the branching ratio for $K^+ \rightarrow \pi^+ \nu \bar{\nu}$. In the E787 $K^+ \rightarrow \pi^+ \nu \bar{\nu}$ analysis, two $K^+ \rightarrow \pi^+ \nu \bar{\nu}$ candidate events were observed in the signal region [23, 24]. Since all of the measurements (background and acceptance functions, background levels, sensitivity, etc.) of E787 and E949 were performed independently, what should be done for combining both results is to evaluate the likelihood estimator, X_{obs} , from all of the sets of $\{s_i\}$, $\{b_i\}$, and $\{d_i\}$ for both results. For the E949 data set, the Signal Region is divided into 3781 cells, while the E787 signal region has 488 cells. Figure 56 shows the likelihood estimator, X_{obs} , for the combined E787 and E949 results as a function of the $K^+ \rightarrow \pi^+ \nu \bar{\nu}$ branching ratio, \mathcal{B} . X_{obs} has the maximum value at $\mathcal{B} = 1.47 \times 10^{-10}$, and the case that $\mathcal{B} = 0$ is unlikely. By using Equation (54), a confidence level interval $(1 - \alpha)$ is calculated so that the probability that the true value of the branching ratio is included between \mathcal{B}_1 and \mathcal{B}_2 ($0 < \mathcal{B}_1 < \mathcal{B}_2$) is

$$1 - \alpha = \int_{\mathcal{B}_1}^{\mathcal{B}_2} P(\mathcal{B}|X_{obs})d\mathcal{B} = \frac{\int_{\mathcal{B}_1}^{\mathcal{B}_2} X_{obs}(\mathcal{B})d\mathcal{B}}{\int_0^{+\infty} X_{obs}(\mathcal{B})d\mathcal{B}}, \quad \text{where } X_{obs}(\mathcal{B}_1) = X_{obs}(\mathcal{B}_2). \quad (57)$$

The $K^+ \rightarrow \pi^+ \nu \bar{\nu}$ branching ratio at the 68% CL interval is obtained as

$$\mathcal{B}(K^+ \rightarrow \pi^+ \nu \bar{\nu}) = (1.47_{-0.86}^{+1.32}) \times 10^{-10} \quad (68\% \text{ CL interval}) \quad (58)$$

CL interval	Branching Ratio
68%	$[0.61, 2.79] \times 10^{-10}$
80%	$[0.45, 3.25] \times 10^{-10}$
90%	$[0.29, 3.90] \times 10^{-10}$
95%	$[0.17, 4.53] \times 10^{-10}$

Table 25: $K^+ \rightarrow \pi^+ \nu \bar{\nu}$ branching ratios at the 68%, 80%, 90%, 95% confidence level intervals.

	E787		E949
Candidate	1995A	1998C	2002A
s_i/b_i	50	7	0.9
$W_i \equiv s_i/(s_i + b_i)$	0.98	0.88	0.48
Background Prob.	0.006	0.02	0.07

Table 26: Signal to background ratio (s_i/b_i), signal weight ($W_i \equiv s_i/(s_i + b_i)$), and probability that the background alone gives rise to the candidate event ($1 - CL_b$) for each candidate event. The first and second candidate events in E787 and the E949 candidate event are called 1995A, 1998C and 2002A, respectively.

based on three candidate events. This measured branching ratio takes only the statistical uncertainty into account. This value is consistent with the SM prediction, although the central value is twice as large as the SM prediction. The $K^+ \rightarrow \pi^+ \nu \bar{\nu}$ branching ratios at several confidence level intervals are summarized in Table 25.

The signal-to-background ratio (s_i/b_i) and the signal weight ($W_i \equiv s_i/(s_i + b_i)$) for each candidate event are summarized in Table 26. The value of s_i for each candidate event is calculated based on the central value of the measured branching ratio, 1.47×10^{-10} . The signal-to-background ratio for the E949 candidate event is 0.9. The probability that the background alone gives rise to the E949 candidate event, or a more signal-like configuration, is 0.074; this value is not small, because the candidate event is observed in a region with a relatively small acceptance and a large background. On the other hand, the probability that the background alone gives rise to the three candidate events, or a more signal-like configuration, is 0.001.

9.3 Estimation of Systematic Uncertainty

Since the branching-ratio calculation depends on the magnitudes of the expected signal events and the background levels in the candidate event cells, the uncertainties concerning the sensitivity and background levels would affect the branching ratio. In Section 6.9, the correlation between the two Bifurcation cuts in each background source is considered, and the quantity that represents the consistency between the predicted and observed b backgrounds outside the Signal Region (the value c) is estimated. The magnitudes for the assumed systematic uncertainties are based on the uncertainties concerning the value c in Table 14; from the table, the uncertainty on each background source was estimated to be 20%. From the sensitivity calculation explained in Chapter 8, the uncertainty on

Source	68% CL interval (10^{-10})		
	$+1\sigma$	-1σ	relative error
No systematic	[0.615, 2.786]		
$K_{\pi 2}$	[0.614, 2.785]	[0.616, 2.787]	+0.043% -0.163%
$K_{\mu 2}$ Range Tail	[0.595, 2.749]	[0.639, 2.829]	+1.533% -3.270%
Muon Band	[0.611, 2.780]	[0.619, 2.792]	+0.226% -0.602%
1 Beam	[0.599, 2.768]	[0.631, 2.804]	+0.646% -2.587%
2 Beam	[0.614, 2.785]	[0.615, 2.786]	+0.007% -0.098%
Sensitivity	[0.676, 3.065]	[0.553, 2.507]	+10.00% -10.00%
Total			+10.14% -10.85%

Table 27: 68% CL intervals with $\pm 1\sigma$ variations of the background levels and the sensitivity. The 2nd and 3rd columns represent the 68% CL intervals with $+1\sigma$ and -1σ variations of each source, respectively. The top and bottom values in the 4th column represent the relative uncertainties with respect to the upper (2.786) and lower (0.615) bounds of the 68% CL interval, respectively.

the sensitivity was estimated to be 10%. These magnitudes concerning the uncertainties are regarded as being one standard-deviation (1σ) of their systematic uncertainties. The differences in the lower and upper boundaries of the 68% CL interval when the background levels and the sensitivity are varied by $\pm 1\sigma$ are treated as a systematic uncertainty. Table 27 summarizes the 68% CL intervals at $\pm 1\sigma$ variations of the background levels and the sensitivity; the main contribution to the systematic uncertainty on the 68% CL intervals is the uncertainty concerning the sensitivity. The systematic uncertainty on the branching ratio is obtained by summing the quadrature of the relative uncertainties, assuming that the uncertainties are not correlated. The systematic uncertainties on the upper and lower bounds (2.786 and 0.615) of the 68% CL interval are estimated to be +10.14% and -10.85%, respectively. The branching ratio at the 68% CL interval is therefore estimated to be

$$\mathcal{B}(K^+ \rightarrow \pi^+ \nu \bar{\nu}) = (1.47_{-0.86}^{+1.32}(\text{stat})_{-0.07}^{+0.28}(\text{sys})) \times 10^{-10} \quad (59)$$

$$= (1.47_{-0.93}^{+1.60}) \times 10^{-10}, \quad (60)$$

where the first and second uncertainties in (59) represent the statistical and systematic uncertainties, respectively, and the uncertainty in (60) represents the sum of the statistical and systematic uncertainties [48].

9.4 Implication for $BR(K^+ \rightarrow \pi^+ X^0)$

The experimental signature of $K^+ \rightarrow \pi^+ X^0$ is the same as $K^+ \rightarrow \pi^+ \nu \bar{\nu}$ except that the kinematic values of π^+ are monochromatic ($P = 227.1$ MeV, $E = 127.0$ MeV, $R = 38.6$ cm). The same analysis method as used in the $K^+ \rightarrow \pi^+ \nu \bar{\nu}$ analysis is used to search for $K^+ \rightarrow \pi^+ X^0$ except for the Phase Space Cuts (and the acceptance factors for it).

The signal region for $K^+ \rightarrow \pi^+ X^0$ is the same as $K^+ \rightarrow \pi^+ \nu \bar{\nu}$ except that the Phase Space Cuts are $\pm 2\sigma$ regions of momentum, energy, range peaks. The upper edges of the

Cut	NIDIF (ON)		NIDIF (OFF)	
	# Events	Acceptance	# Events	Acceptance
Setup	100000	-	60000	-
T•2	43768	0.4377	27354	0.4559
(6 _{ct} + 7 _{ct})	36379	0.8312	27353	1.0000
DC	36379	1.0000	27353	1.0000
19 _{ct}	35814	0.9845	27198	0.9943
BV + BVL + EC	35643	0.9952	27198	1.0000
HEX	35532	0.9969	27198	1.0000
Refined Range	24219	0.6816	23512	0.8645
<i>A_{trigger}</i>	0.2422±0.0014		0.3919±0.0020	
Setup	24066	-	23504	-
UFATE	21105	0.8770	23504	1.0000
USTMED	20911	0.9908	23261	0.9897
USTOP_HEX	20255	0.9686	23187	0.9968
COS3D	19413	0.9584	22168	0.9561
LAYER14	19290	0.9937	22133	0.9984
ZFRF	17538	0.9092	20087	0.9076
ZUTOUT	17533	0.9997	20076	0.9995
Loose Phase Space	10748	0.6130	14174	0.7060
Phase Space	10748	0.6130	14174	0.7060
<i>A_{MC}</i> (Signal Region)	0.4466±0.0032		0.6030±0.0032	
<i>A_{MC}</i> (1×1 Region)	0.4466±0.0032		0.6030±0.0032	

Table 28: Summary of the trigger, phase space, and solid angle acceptances for $K^+ \rightarrow \pi^+ X^0$ with the pion nuclear interaction and decay-in-flight (NIDIF) turned on or off. The errors are statistical.

Phase Space Cuts are tightened ($P \leq 229$ MeV/c, $E \leq 135$ MeV, and $R \leq 40$ cm as in $K^+ \rightarrow \pi^+ \nu \bar{\nu}$) so that the Muon background can be suppressed. The expected background level is small (0.05 events), because the region is far from the $K_{\pi 2}$ peaks.

The candidate event observed in the Signal Region for $K^+ \rightarrow \pi^+ \nu \bar{\nu}$ is also in the $K^+ \rightarrow \pi^+ X^0$ signal region; the candidate event is not exactly identified as $K^+ \rightarrow \pi^+ X^0$ signal, and only the upper limit is set with the assumption that the background is absent.

The trigger, phase space, and solid angle acceptances are measured with the Monte Carlo simulation which generates the $K^+ \rightarrow \pi^+ X^0$ decay (Table 28). All the acceptance factors for the $K^+ \rightarrow \pi^+ X^0$ analysis are summarized in Table 29. The acceptance factors for the enlarged signal region (Signal Region) are also measured. For the $K^+ \rightarrow \pi^+ X^0$ Signal Region, the Phase Space Cuts are not loosened; the acceptance gains from only the PV Extended and $\pi^+ \rightarrow \mu^+ \rightarrow e^+$ Extended Regions are taken into account, which results in 21% acceptance gain with respect to that for the 1×1 Region. The total acceptance and sensitivity for the $K^+ \rightarrow \pi^+ X^0$ analysis are measured to be

$$A_{total} = (6.89 \pm 0.20 \pm 0.52) \times 10^{-3} \quad \text{and} \quad S.E.S = (0.82 \pm 0.02 \pm 0.06) \times 10^{-10}, \quad (61)$$

where the first and second errors are the statistical and systematic uncertainties.

There was no candidate event in the $K^+ \rightarrow \pi^+ X^0$ signal region of E787. The combined E787 and E949 sensitivity of 0.196×10^{-10} and the Feldman and Cousins method [51] in the assumption of one signal event and no background give the upper limit for the

Factor	Acceptance	
	Signal Region	1×1 Region
Trigger acceptance	0.3919±0.0020±0.0196	
K^+ stop efficiency	0.7740±0.0011	
Beam and target analysis	0.5483±0.0007	
Phase space and solid angle	0.6123±0.0032	
π^+ nucl. int. and decay-in-flight	0.4577±0.0054±0.0229	
Reconstruction efficiency	0.9956±0.0001	
Other kinematics constraints	0.5013±0.0071±0.0154	
$\pi^+ \rightarrow \mu^+ \rightarrow e^+$ decay acceptance	0.3893±0.0085±0.0074	0.3476±0.0076±0.0066
Accidental loss	0.8204±0.0019	0.7509±0.0022
T•2 efficiency	0.9357±0.0011±0.0168	
Total acceptance	$(6.89 \pm 0.20 \pm 0.52) \times 10^{-3}$	$(5.68 \pm 0.17 \pm 0.44) \times 10^{-3}$
K^+ Trigger ($K^+ \rightarrow \pi^+ X^0$)	1.77×10^{12}	
Sensitivity	$(0.82 \pm 0.02 \pm 0.06) \times 10^{-10}$	$(0.99 \pm 0.03 \pm 0.08) \times 10^{-10}$

Table 29: Acceptances and sensitivity for the $K^+ \rightarrow \pi^+ X^0$ analysis. The first and second uncertainties represent the statistical and systematic uncertainties, respectively.

$K^+ \rightarrow \pi^+ X^0$ decay as:

$$\mathcal{B}(K^+ \rightarrow \pi^+ X^0) < 3.81 \times 0.196 \times 10^{-10} = 0.747 \times 10^{-10} \quad (62)$$

at 90% confidence level. This limit is larger than the previous limit 0.59×10^{-10} (90% CL) from the E787 result [23, 24] due to one candidate event in E949.

9.5 Impact of $K^+ \rightarrow \pi^+ \nu \bar{\nu}$ Branching Ratio on Unitarity Triangle

The $K^+ \rightarrow \pi^+ \nu \bar{\nu}$ branching ratio constrains the CKM matrix element, $|V_{td}|$. The quantity that is directly extracted from $\mathcal{B}(K^+ \rightarrow \pi^+ \nu \bar{\nu})$ is $|\lambda_t| \equiv |V_{ts}^* V_{td}|$. To extract $|V_{td}|$, $|\lambda_t|$ should be divided by $|V_{cb}| \simeq |V_{ts}|$. Since $|V_{cb}|$ should be measured from B decays, the quantity $|\lambda_t|$ is extracted in order to perform an independent measurement from B decays. $|V_{td}|$ is extracted by dividing $|\lambda_t|$ by $|V_{cb}|$.

Equation (9) can be written as

$$\mathcal{B}_{\pi^+ \nu \bar{\nu}} = \xi \left[(\text{Im} \lambda_t X_t)^2 + (\lambda_c \bar{X} + \text{Re} \lambda_t X_t)^2 \right], \quad (63)$$

where

$$\xi \equiv \frac{3\alpha^2 \mathcal{B}(K^+ \rightarrow \pi^0 e^+ \nu)}{|V_{us}|^2 2\pi^2 \sin^4 \Theta_W^4}, \quad \bar{X} \equiv \lambda^4 P_c(X) = \frac{1}{3}(2X_{\text{NL}}^e + X_{\text{NL}}^\tau), \quad \text{and} \quad X_t \equiv X(x_t). \quad (64)$$

From the upper limit of $\mathcal{B}(K^+ \rightarrow \pi^+ \nu \bar{\nu})$ the above equation has the relation

$$\mathcal{B}_{\pi^+ \nu \bar{\nu}}^{\text{MAX}} \geq \xi \left[(\text{Im} \lambda_t X_t)^2 + (\lambda_c \bar{X} + \text{Re} \lambda_t X_t)^2 \right]. \quad (65)$$

Assuming the extreme case that the second term equals zero (i.e., real parts of the charm and top contributions cancel each other exactly), one obtains the following relations:

$$\begin{aligned} \mathcal{B}_{\pi^+ \nu \bar{\nu}}^{\text{MAX}} &> \xi (\text{Im} \lambda_t X_t)^2, \\ |\text{Im} \lambda_t X_t| &< \sqrt{\mathcal{B}_{\pi^+ \nu \bar{\nu}}^{\text{MAX}} / \xi}. \end{aligned} \quad (66)$$

Using $\xi = 1.5226 \times 10^{-4}$ and the measured branching ratio at the 68% CL interval, $\mathcal{B}_{\pi^+\nu\bar{\nu}}^{MAX} = 3.07 \times 10^{-10}$. All of the values of the branching ratio used in this calculation include the systematic uncertainty. Taking $m_t = 168.1$ GeV to give $X_t = 1.529$, one can get $|\text{Im}\lambda_t| < 0.928 \times 10^{-3}$ from Equation (66).

The limits on the real part of λ_t can be set by assuming the extreme case that the imaginary part of λ_t is equal to zero.

$$\begin{aligned}\mathcal{B}_{\pi^+\nu\bar{\nu}}^{MAX} &> \xi (\lambda_c \bar{X} + \text{Re}\lambda_t X_t)^2 \\ |\lambda_c \bar{X} + \text{Re}\lambda_t X_t| &< \sqrt{\mathcal{B}_{\pi^+\nu\bar{\nu}}^{MAX}/\xi}.\end{aligned}\tag{67}$$

Since λ_c is negative,

$$\text{Re}\lambda_t X_t < \sqrt{\mathcal{B}_{\pi^+\nu\bar{\nu}}^{MAX}/\xi} + |\lambda_c \bar{X}|,\tag{68}$$

$$\text{Re}\lambda_t X_t > -\sqrt{\mathcal{B}_{\pi^+\nu\bar{\nu}}^{MAX}/\xi} + |\lambda_c \bar{X}|.\tag{69}$$

\bar{X} has a large uncertainty and depends on the charm quark mass, m_c , the scale factor, $\mu_c = \mathcal{O}(m_c)$, and the coupling constant, $\alpha_s(M_Z^2)$. Maximizing \bar{X} ($= 1.098 \times 10^{-3}$) in Equation (68) gives $\text{Re}\lambda_t < 1.085 \times 10^{-3}$. Minimizing \bar{X} ($= 0.761 \times 10^{-3}$) in Equation (69) gives $\text{Re}\lambda_t > -0.8197 \times 10^{-3}$. Note that the limit given in Equation (68) is also a limit on $|\lambda_t X_t|$, because, for a given $\mathcal{B}_{\pi^+\nu\bar{\nu}}$, $|\lambda_t|$ is maximum when it is real and directed opposite to $\lambda_c \bar{X}$.

From the lower limit of $\mathcal{B}(K^+ \rightarrow \pi^+ \nu \bar{\nu})$ we obtain

$$\begin{aligned}\mathcal{B}_{\pi^+\nu\bar{\nu}}^{MIN} &< \xi |\lambda_c \bar{X} + \lambda_t X_t|^2, \\ \sqrt{\mathcal{B}_{\pi^+\nu\bar{\nu}}^{MIN}/\xi} &< |\lambda_c \bar{X} + \lambda_t X_t| \\ &< |\lambda_c \bar{X}| + |\lambda_t X_t|, \\ \sqrt{\mathcal{B}_{\pi^+\nu\bar{\nu}}^{MIN}/\xi} - |\lambda_c \bar{X}| &< |\lambda_t X_t|.\end{aligned}\tag{70}$$

By maximizing \bar{X} , we obtain $|\lambda_t| > 2.355 \times 10^{-4}$.

In summary, from $\mathcal{B}(K^+ \rightarrow \pi^+ \nu \bar{\nu}) = (1.47_{-0.93}^{+1.60}) \times 10^{-10}$ (68% CL) the limits on λ_t are

$$\begin{aligned}0.236 \times 10^{-3} &< |\lambda_t| < 1.085 \times 10^{-3}, \\ -0.820 \times 10^{-3} &< \text{Re}\lambda_t < 1.085 \times 10^{-3}, \\ \text{Im}\lambda_t &< 0.928 \times 10^{-3}.\end{aligned}\tag{71}$$

From $\mathcal{B}(K^+ \rightarrow \pi^+ \nu \bar{\nu}) = (1.47_{-1.22}^{+2.83}) \times 10^{-10}$ (90% CL) the limits on λ_t are

$$\begin{aligned}0.107 \times 10^{-3} &< |\lambda_t| < 1.256 \times 10^{-3}, \\ -0.990 \times 10^{-3} &< \text{Re}\lambda_t < 1.256 \times 10^{-3}, \\ \text{Im}\lambda_t &< 1.099 \times 10^{-3}.\end{aligned}\tag{72}$$

The limits on $|V_{td}|$ are extracted from Equations (71) and (72) by using the measured limits $|V_{cb}| \simeq [0.039, 0.044]$ from PDG2004[6].

$$0.0054 < |V_{td}| < 0.0278 \quad (68\% \text{ CL}),\tag{73}$$

$$0.0024 < |V_{td}| < 0.0322 \quad (90\% \text{ CL}).\tag{74}$$

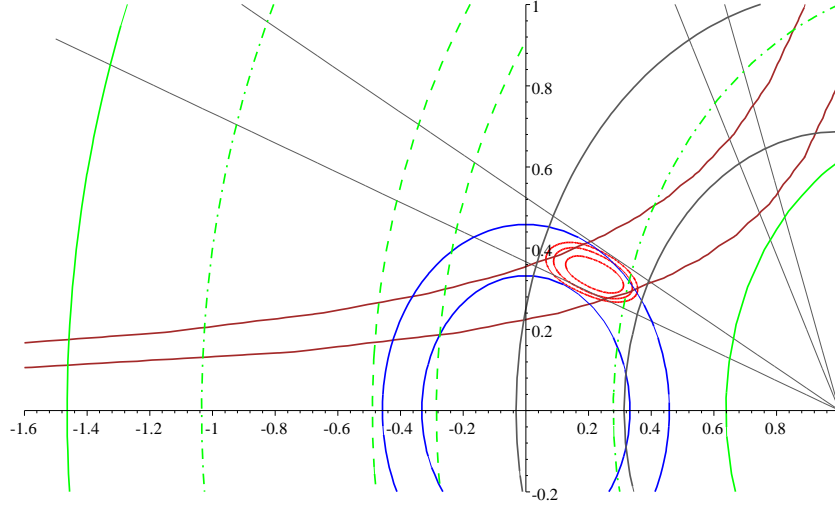


Figure 57: Impact of the $K^+ \rightarrow \pi^+ \nu \bar{\nu}$ branching ratio on the unitarity triangle [49]. The green lines indicate the constraints from the $K^+ \rightarrow \pi^+ \nu \bar{\nu}$ branching ratio (with theoretical uncertainty): central value (dashed), 68% CL interval (dot-dashed), 90% CL interval (solid). The red ovals show the 68%, 90%, 95% CL areas from other measurements ($|V_{ub}|$, ϵ_K , $\sin 2\beta$, Δm_d).

The latter is compared with the current experimental range of $|V_{td}|$, $0.0048 < |V_{td}| < 0.014$ in PDG2004[6]. The limits on $|V_{td}|$ obtained from our results are a bit wider than those from other measurements. Figure 57 shows the impact of the $K^+ \rightarrow \pi^+ \nu \bar{\nu}$ branching ratio on the unitarity triangle. The central value of the measured $K^+ \rightarrow \pi^+ \nu \bar{\nu}$ branching ratio does not intersect with the area of (ρ, η) constrained by $|V_{ub}|$, ϵ_K , $\sin 2\beta$, and Δm_d in other measurements, all of which support the SM prediction. This result is very interesting in that the discrepancy may indicate new physics. For example, once the constraints from the measurements of $\sin 2\beta$ and Δm_d , both of which are obtained from the $\Delta F = 2$ weak processes, are removed, the central value intersects with the area constrained by the other K and B decays in the region $\gamma > 90^\circ$ (Figure 58) [50]. The $K^+ \rightarrow \pi^+ \nu \bar{\nu}$ branching ratio should be measured precisely with more statistics and, with the measurement of the $K_L^0 \rightarrow \pi^0 \nu \bar{\nu}$ branching ratio, independent measurements of ρ and η from K and B decays are necessary to see whether there is a discrepancy or not.

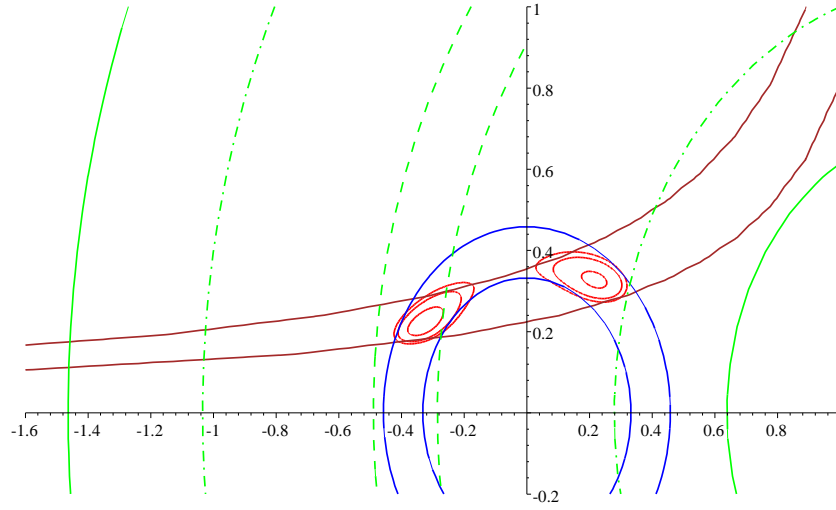


Figure 58: Impact of the $K^+ \rightarrow \pi^+ \nu \bar{\nu}$ branching ratio on the unitarity triangle excluding the constraints from the $\sin 2\beta$ and Δm_d measurements [49]. The green lines indicate the $K^+ \rightarrow \pi^+ \nu \bar{\nu}$ branching ratio (with theoretical uncertainty): central value (dashed), 68% CL interval (dot-dashed), 90% CL interval (solid). The red ovals show 68%, 90%, 95% CL areas from other measurements ($|V_{ub}|$ and ϵ_K).

10 Conclusion

The rare decay $K^+ \rightarrow \pi^+ \nu \bar{\nu}$ is a flavor-changing-neutral-current process and proceeds via 1-loop diagrams that mediate the top quark. This decay involves the coupling of top to down quarks. The branching ratio of $K^+ \rightarrow \pi^+ \nu \bar{\nu}$ is expressed by the magnitude of the CKM matrix element, $|V_{td}|$. Measuring $\mathcal{B}(K^+ \rightarrow \pi^+ \nu \bar{\nu})$ is one of the cleanest ways to extract $|V_{td}|$.

BNL-E949 is a successor to BNL-E787. The E949 detector was upgraded to achieve better measurements in the beam rate, twice that of E787. E949 examined stopped K^+ decays. A high-intensity K^+ beam was produced at the Alternating Gradient Synchrotron (AGS) by exposing 65 trillion protons per spill to a platinum target. Kaons with 710 MeV/c were transported to the E949 detector, and came to rest in a scintillating fiber target. 3.9×10^6 K^+ 's decayed at rest in the target per spill. The data were collected in 2002, which corresponded to 1.77×10^{12} K^+ decays.

The data were analyzed by a blind analysis. The Signal Region was masked out until the selection criteria were determined and the background levels were estimated. The development of the cuts and the estimation of the background levels were performed by using the Bifurcation Method. The Signal Region was enlarged compared to that in E787 with an increased confidence in the likelihood analysis. The enlargement of the Signal Region increased the acceptance by 30%. The total background level in the Signal Region was estimated to be 0.30 ± 0.02 events.

An examination of the Signal Region yielded one event near the upper kinematic limit of the $K^+ \rightarrow \pi^+ \nu \bar{\nu}$ decay. Based on the candidate event, an upper limit was set to be $\mathcal{B}(K^+ \rightarrow \pi^+ \nu \bar{\nu}) < 8.76 \times 10^{-10}$ at the 90% CL. E787 and E949 results were combined and the branching ratio was measured to be $(1.47_{-0.93}^{+1.60}) \times 10^{-10}$ at the 68% CL interval based on three events observed in the momentum region $211 \leq P \leq 229$ MeV/c. The measured branching ratio was twice as large as the SM prediction of $(0.78 \pm 0.12) \times 10^{-10}$, but was consistent within the error. At the measured central value of the branching ratio, the candidate event had a signal-to-background ratio of 0.9.

From the measured branching ratio, we set the limits on both $|\lambda_t|$ and $|V_{td}|$ to be

$$0.107 \times 10^{-3} < |\lambda_t| < 1.256 \times 10^{-3} \quad \text{and} \quad 0.0024 < |V_{td}| < 0.0322,$$

at the 90% CL interval, which was consistent with the current experimental range of $0.0048 < |V_{td}| < 0.014$ at the 90% CL interval.

References

- [1] W. Buchmiller, hep-ph/0306047
- [2] A.D. Sakharov, JETP Lett 5(1967) 24
- [3] V.A. Rubakov, M.E. Shaposhnikov, Usp. Fiz Nauk 166 (1996) 493; Phys. Usp. 39 (1996) 461; A Riotto and M. Trodden, Annu. Rev. Nucl. Part. Sci. 49(1999) 35.
- [4] M. Kobayashi and T. Maskawa, Prog. Theor. Phys. **49**, 652 (1973).
- [5] L. Wolfenstein, Phys. Rev. Lett. **51**, 1945 (1983).
- [6] Particle Data Group, S. Eidelman *et al.*, Phys. Lett. **B592**, 1 (2004)
- [7] C. Jarlskog, Phys. Rev. Lett. **55**, 1039 (1985); C. Jarlskog, Z. Phys. **C29**, 491 (1985); C. Jarlskog and R. Stora, Phys. Lett. **B208**, 268 (1988).
- [8] A.J. Buras, F. Schwab, and S. Uhlig, arXiv:hep-ph/0405132 (2004).
- [9] T. Inami and C.S. Lim, Prog. Theor. Phys. **65**, 297 (1981).
- [10] G. Buchalla and A.J. Buras, Nucl. Phys. **B548**, 309 (1999).
- [11] G. Buchalla and A.J. Buras, Nucl. Phys. **B398**, 285 (1993).
- [12] M. Musiak and J. Urban, Phys. Lett. **B451**, 161 (1999).
- [13] W.J. Marciano and Z. Parsa, Phys. Rev. **D53**, 1 (1996).
- [14] Particle Data Group, K. Hagiwara *et al.*, Phys. Rev. **D66**, 010001 (2002).
- [15] A.J. Buras, M.E. Lautenbacher, and G. Ostermaier, Phys. Rev. **D50**, 3433 (1994).
- [16] D. Rein and L.M. Sehgal, Phys. Rev. **D39**, 3325 (1989); J.S. Hagelin and L.S. Littenberg, Prog. Part. Nucl. Phys. **23**, 1 (1989); M. Lu and M.B. Wise, Phys. Lett. **B324**, 461 (1994); S. Fajfer, arXiv:hep-ph/9602322 (1996); C.Q. Geng, I.J. Hsu, and Y.C. Lin, Phys. Rev. **D54**, 877 (1996).
- [17] K. Anikeev *et al.*, Workshop Report "B Physics at the Tevatron: Run II and Beyond", arXiv:hep-ph/0201071 (2002).
- [18] A. Belyaev *et al.*, Kaon Physics working Group Report "Kaon Physics with a High-intensity Proton Driver", arXiv:hep-ph/0107046 (2001); G. Isidori, arXiv:hep-ph/0110255 (2001); G. Buchalla, arXiv:hep-ph/0110313 (2001).
- [19] A.J. Buras, arXiv:hep-ph/0402191 (2004); G. Isidori, arXiv:hep-ph/0301159 (2003).
- [20] A.J. Buras *et al.*, arXiv:hep-ph/0402112 (2004); A.J. Buras *et al.*, arXiv:hep-ph/0408142 (2004).

- [21] Y. Grossman and Y. Nir, Phys. Lett. **B398**, 163 (1997).
- [22] F. Wilczek, Phys. Rev. Lett. **49**, 1549 (1982); J.L. Feng *et al.*, Phys. Rev. **D57**, 5875 (1998).
- [23] S. Adler *et al.*, Phys. Rev. Lett. **79**, 2204 (1997).
- [24] S. Adler *et al.*, Phys. Rev. Lett. **88**, 041803 (2002); S. Adler *et al.*, Phys. Rev. Lett. **84**, 3768 (2000);
- [25] J.H. Klems *et al.*, Phys. Rev. **D4**, 66 (1971).
- [26] G.D. Cable *et al.*, Phys. Rev. **D8**, 3807 (1973).
- [27] Y. Asano *et al.*, Phys. Lett. **B107**, 159 (1981).
- [28] M.S. Atiya *et al.*, Nucl. Instr. Meth. **A321**, 129 (1992).
- [29] S. Adler *et al.*, Phys. Rev. Lett. **76**, 1421 (1996).
- [30] B. Bassalleck *et al.*, E949 proposal, BNL-67247, TRI-PP-00-06 (1999), <http://www.phy.bnl.gov/e949/> .
- [31] T. Yoshioka *et al.*, IEEE Trans. Nucl. Sci. **51**, 199 (2004).
- [32] J. Doornbos *et al.*, Nucl. Instr. Meth. **A444**, 546 (2000).
- [33] D.A. Bryman *et al.*, Nucl. Instr. Meth. **A396**, 394 (1997).
- [34] M. Atiya *et al.*, Nucl. Instr. Meth. **A279**, 180 (1989).
- [35] E.W. Blackmore *et al.*, Nucl. Instr. Meth. **A404**, 295 (1998).
- [36] R.A. McPherson, "Chasing the Rare Decay $K^+ \rightarrow \pi^+ \nu \bar{\nu}$ ", Princeton University, Ph.D. Thesis, November, 1995.
- [37] I.H. Chiang *et al.*, IEEE Trans. Nucl. Sci. **42**, 394 (1995).
- [38] T.K. Komatsubara *et al.*, Nucl. Instr. Meth. **A404**, 315 (1998).
- [39] C. Caso *et al.*, European Physical Journal **C3**, 1 (1998).
- [40] P. Meyers, "A modified Version of the UMC Multiple Scattering Routine MSCAT1", E787 Technical Note No.77 (1985). Unpublished.
- [41] A.J. Stevens, "Nuclear Interactions in CH revisited", E787 Technical Note No.140 (1987). Unpublished.
- [42] W.R. Nelson *et al.*, "The EGS4 Code Syatem", SLAC 265, SLAC (1985).
- [43] T. Sekiguchi, "Development of Silicon Strip Detector for Rare Kaon Decay Experiments", University of Tokyo, Master Thesis, January, 2002.

- [44] J.B. Birks, Proc. Phys. Soc. **A64**, 874 (1951).
- [45] The reference manual can be found in
<http://paw.web.cern.ch/paw/mlpfit/pawmlp.html>.
 The PDF version of the reference manual can also be available in
<http://schwind.home.cern.ch/schwind/MLPfit/doc/pawmlp.pdf>.
- [46] S. Adler *et al.*, Phys. Rev. Lett. **85**, 2256 (2000); M.R. Convery, "First Measurement of Structure Dependent $K^+ \rightarrow \mu^+ \nu_\mu \gamma$ ", Princeton University, Ph.D. Thesis, November, 1996.
- [47] T. Junk, Nucl. Instr. Meth. **A434**, 435 (1999).
- [48] The branching ratio published by the E949 collaboration (V.V. Anisimovsky *et al.*, Phys. Rev. Lett. **93**, 031801 (2004)), $(1.47_{-0.89}^{+1.30}) \times 10^{-10}$, was based on a statistical technique developed by T. Junk [47].
- [49] Figures 57 and 58 are made by G. Isidori.
- [50] G. Isidori, arXiv:hep-ph/0307014 (2003); G. Isidori, arXiv:hep-ph/0301159 (2003).
- [51] G.J. Feldman and R.D. Cousins, Phys. Rev. **D57**, 3873 (1998).